University of Stavanger

Faculty of Science and Technology

MASTER'S THESIS

Study program/Specialization: Petroleum Geosciences Engineering	Spring 2017 Open
Writer: Ivan Gutierrez	(Writer's signature)
Faculty supervisor: Nestor Cardozo	
Title of thesis: Application of trishear and elastic dislocation models to the Teapot Anticline, Wyoming	
Credits (ECTS): 30	
Keywords: Trishear Modelling Elastic Dislocation Modelling Teapot Anticline	Pages: 107 +enclosure: USB memory Stavanger, June 15th 2017

Application of trishear and elastic dislocation models to the Teapot Anticline, Wyoming

by

Ivan Gutierrez

Master Thesis

Presented to the Faculty of Science and Technology

University of Stavanger

The university of Stavanger

June 2017

Acknowledgements

I am extremely grateful with Nestor Cardozo for all the guidance and mentoring along these two years of master and for his dedication during the supervision of this study. Many thanks to Badley Geoscience, especially to Graham Yielding for all the technical support with Trap Tester software in this project, and also for his valuable advises and comments during the mechanical modelling. I also would like to thanks to Rocky Mountain Oil Field Testing Centre (RMOTC) for providing the data set. Special thanks to all the professor and Petroleum Geoscience staff for these two years of shared knowledge and experiences. To all my master classmates who contributed to a pleasant environment.

This thesis is dedicated to my family, especially to my wife Luz, and my two children, Esteban and Pablo. Thanks to their infinite support, patience and love, I have always felt motivated to deliver my best.

Abstract

Application of trishear and elastic dislocation models to the Teapot Anticline, Wyoming

Ivan Gutierrez

University of Stavanger, 2016

Supervisor: Nestor Cardozo

Teapot Dome is a Laramide fault-propagation fold developed over a west-vergent thrust that involves basement. In this thesis, I test the applicability of the kinematic trishear model and the mechanical elastic dislocation model to the Teapot Dome, Wyoming. The public domain dataset provided, consisting of 2D and 3D seismic, and a couple of wells with fracture data, is a typical example of a dataset with poor seismic imaging of the steeply dipping forelimb and lack of coverage in the footwall region. Additionally, the underlying thrust is not clearly imaged. Kinematic 2D trishear inverse modelling was applied to reconstruct the geometry of the thrust, forelimb and footwall on eight cross sections along the anticline. Then, a 3D structural model was constructed based on the trishear modelled cross-sections. This 3D structural model was the input for elastic dislocation modelling (ED). ED helped validating and modifying the reconstructed anticlinal and thrust geometry. ED fracture prediction was validated using fracture data from two selected wells, one close to the thrust and another in the backlimb. Fractures in these wells are tensile, and the ED predicted maximum compressive stress (S1) close to the wells, is subparallel to the wells fractures, which indicates that the ED model is a good proxy for the orientation of tensile fractures, and perhaps also shear fractures. Fracture intensity can be predicted using the ED maximum Coulomb shear stress (MCSS), which suggests more fracturing near the thrust and particularly in the footwall area. On cross section, trishear and ED proxies for fractures are similar, although the orientation of ED conjugate shear planes and trishear lines of no finite elongation (LNFE) is somewhat different, with the acute angle between LNFE being smaller than the one for the ED conjugate shear fractures. These results highlight the importance of using structural modelling techniques in discrete fracture networks (DFN) generation, and not just statistical or seismic-attributes based techniques.

Table of Contents

List of Tables

List of Figures

1 Introduction

Classical structural traps such as anticlines and folds in general, are the most relevant for the hydrocarbon industry. In sedimentary basins, faults are intimately related with folds. Naturally, thrust faults and anticlines co-exist in contractional regimes associated with large-scale orogenic process (Suppe, 1985). Fold and thrust belts and foreland basins are the typical signature of contractional and transpressional regimes. Fold and thrust belts reserves constitute about 14% of global reserves (Cooper, 2007) and amount to 15% of the undiscovered resources globally (USGS, 2000).

The structural evolution of thrust-anticlines needs to be well understood to constrain its geometry and strain. In general, the mechanical stratigraphy and direction of applied stresses control the fold growth (Groshong Jr, 2006). Thrust-anticlines form when the maximum horizontal stress is the largest principal stresses ($\sigma H > \sigma h > \sigma v$). Minor faults and fractures form in the reservoir rocks as consequence of applied stresses and the accumulation of strain. Fractures control the nature and distribution of porosity and permeability in the reservoirs, which is critical for well planning and development of these structures.

3D structural modelling integrates outcrop and subsurface (seismic and wells) data. Interpretation of these data provides observation points that control the interpolation and extrapolation required to construct a 3D model of the structures. The modelling of the complete geometry of the structures will require a lot of inferences since they are often undersampled (Groshong, 2008).

3D modelling methods are also challenged by the different scales of subsurface data, seismic and wells. Thrust-anticlines smaller than 10-20 m are poorly imaged or not imaged at all in conventional seismic surveys. An additional challenge is the presence of no-seismic-image, or wipeout zones that make impossible to distinguish faults from steeply dipping fold limbs (Kostenko *et al.*, 2008); Brandenburg et al., 2011). On the other hand, wells are localized and their information is difficult to interpolate. Unreliable results can be obtained if the wells are few and their distribution is not uniform.

A thrust system can be classified as thick- or thin-skinned if the detachment involves or does not involve basement, respectively. Since the last century, basement-cored anticlines across the Rocky Mountain region have been hydrocarbon-exploration targets (S. P. Cooper *et al.*, 2006). Traps in the Rocky Mountain belt amount to approximately 0.9 bn bbls of oil, 2 bn bbls of condensate, and 6 bn boe of gas (Cooper, 2007).

Teapot Dome, also known as the Naval Petroleum Reserve (NPR 3), is a Laramide basement-cored anticline near the southwestern edge of the Powder River basin in Natrona County, central-east Wyoming (Figure 1). Teapot Dome is a fault-propagation fold developed over a west-vergent thrust that involves basement. 1.5 million barrels of oil have been produced from the Tensleep formation, or 30% of the estimated 5 million STBO originally in place (Giangiacomo, 2000). In this study, I analyse the fold geometry across the sedimentary cover, from the Devonian Freemont Canyon Formation unconformably lying over the Precambrian granite, to the early upper Cretaceous Frontier Wall Creek Formation.

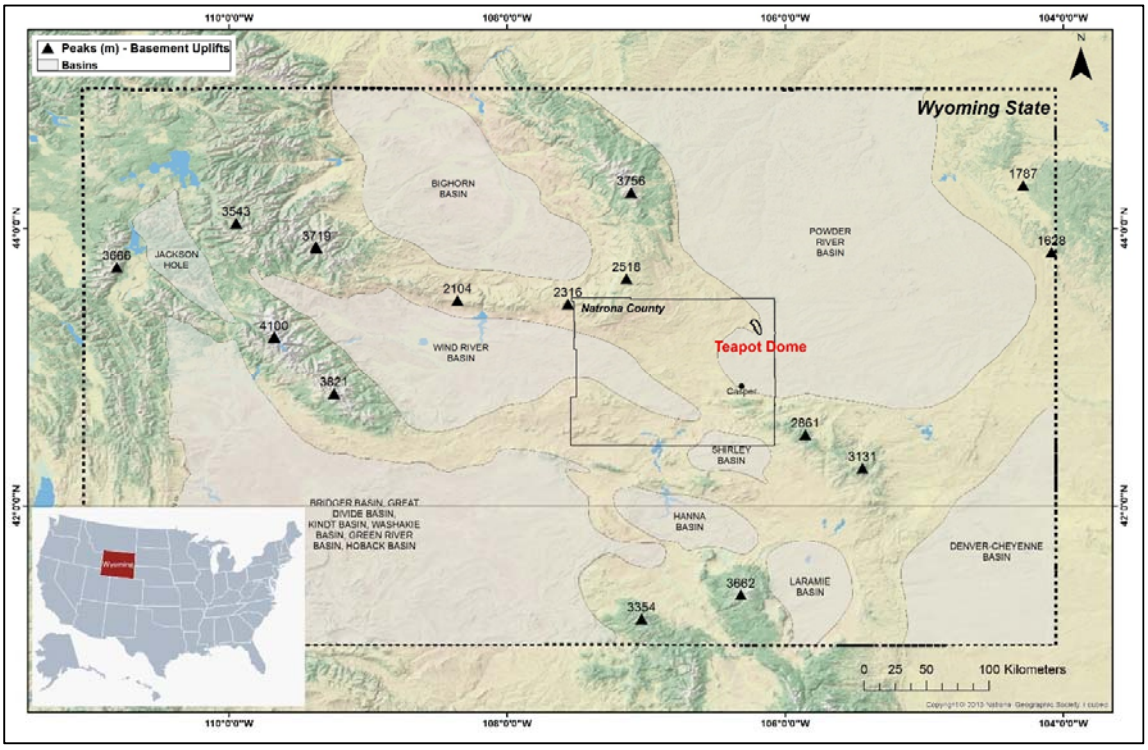

Figure 1. Geographical location of Teapot Dome, Wyoming, US. Light brown areas are basins. Base Map courtesy of The National Geographic Society (2013).

I present a modelling workflow to construct a plausible 3D structural model of Teapot Dome. The dataset used for this study are of public domain and is provided by The Rocky Mountain Oil Testing Centre (RMOTC, 2005a, 2005b). The dataset consists of a 3D seismic survey, 2D seismic lines, well logs and formation micro imager (FMI) logs. I deal with the limitations of the provided pre-stack migrated seismic dataset. The 3D seismic cube does not cover the entire structure. The west-vergent basement-sitting thrust, the steeper west dipping limb (forelimb), and the footwall are poorly imaged or not imaged at all (Figure 2).

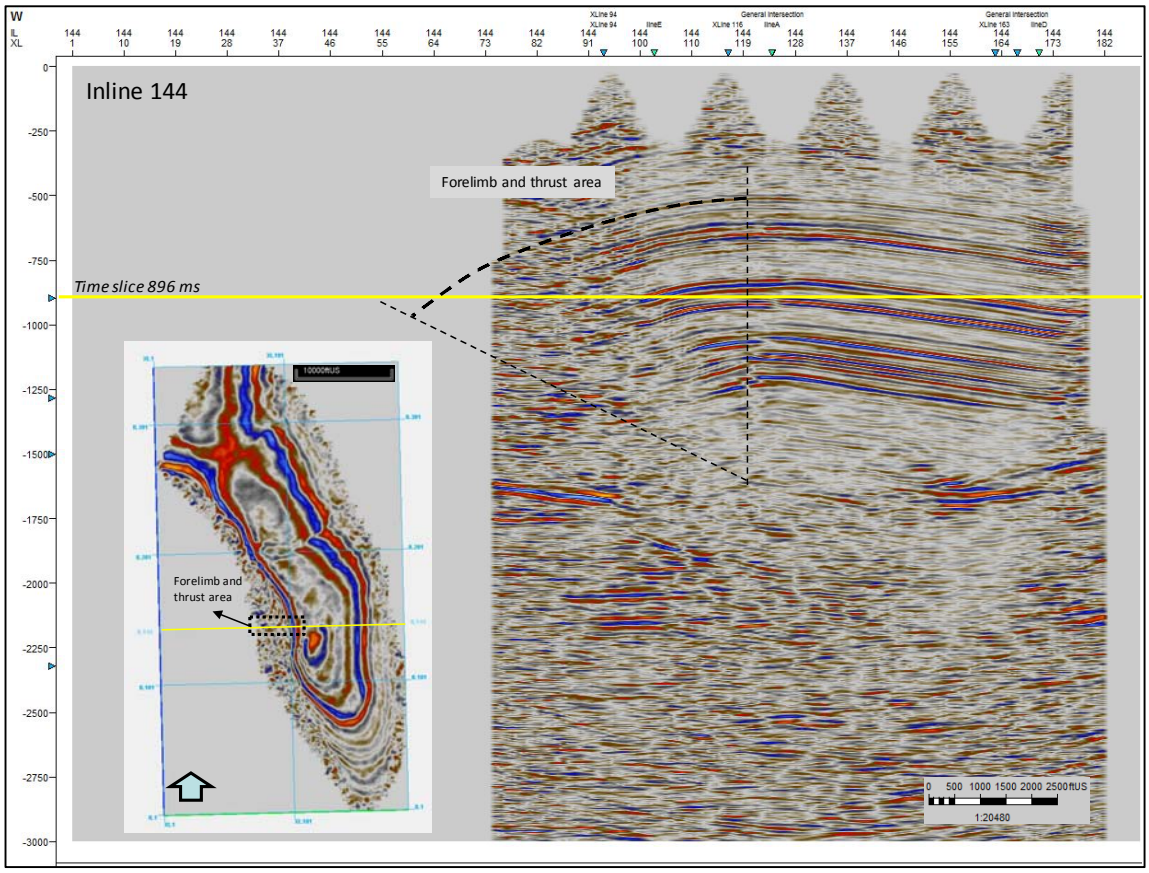

Figure 2 Poor seismic imaging of the west dipping forelimb, west-vergent basement-sitting thrust, and footwall of the Teapot Dome. Inline 144 of the 3D seismic cube in time domain. Vertical scale in Two-way time. The location of the line is shown in the inset figure by the yellow line. Inset figure is a time slice at 896 ms.

Only two 2D seismic lines cover the entire structure. However, these lines do not image well steeply dipping zones (Figure 3a-c). High-amplitude reflectors (1 - 5) can be easily followed and in general they depict a fault-propagation anticline (Figure 3a). However, a wipeout zone below the horizons makes difficult to interpret the thrust tip and the horizons cutoffs. Different interpretations can be proposed. The most simple is to maintain the thickness of the layers and

use an intermediate location for the thrust. The thrust tip would be located between horizons 1 and 2. Figures 3b and 3c illustrate two different, more complex scenarios that formulate several alternatives regarding the horizons and thrust geometry in the forelimb. Kostenko et al. (2008) and Brandenburg et al. (2011) describe the problems related to seismic imaging in the steep limbs of thrust-anticlines. Kostenko *et al.*, 2008 highlight the importance of knowing the geometry of the thrust termination, to correctly evaluate the risk of the structural trap.

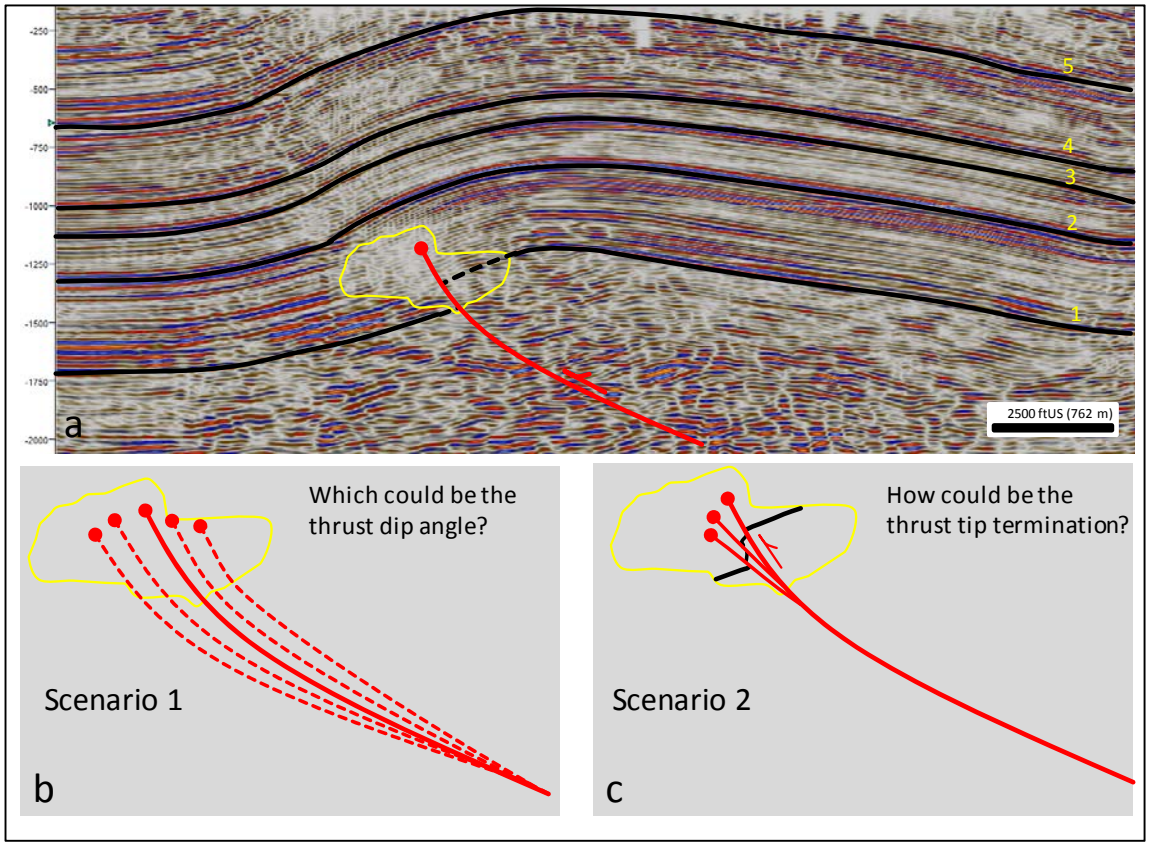

Figure 3 ***a*** *2D seismic line D in time domain (ms) across Teapot Dome. Notice the chaotic seismic response in the yellow polygon between horizons one and two;* ***b*** *and* ***c*** *Scenarios one and two showing different alternatives of thrust geometry. Scenario 1 is based on the thrust dip angle, and scenario 2 is based on the upward termination of the thrust. Vertical scale in Two-way time.*

Several studies of Teapot Dome have been published recently. Most of these studies have been focused on fractures and fracture network modelling of the anticline. Different authors (Kundacina, 2016; Schneider *et al.*, 2016; Schwartz, 2006; Wilson *et al.*, 2015) have applied diverse approaches to characterize the fracture patterns and to generate conceptual fracture models and discrete fracture networks (DFN) of the Teapot Dome. Approaches such as outcrop

characterization, extrapolation of well information using statistical tools, application of seismic attributes, or an integration of these last two, are the most common methods.

The main motivation of this thesis is to provide a new structural modelling approach that helps to better understand the geometry, kinematics and mechanics of the Teapot Dome, especially when the dataset does not provide a complete picture of the structure. The objective is to apply two structural modelling techniques: i. the kinematic trishear model (Hardy & Allmendinger, 2011), and ii. the mechanical elastic dislocation model (Dee *et al.*, 2007). The objective is to evaluate how these two models predict and reconstruct the geometry of the anticline, and the spatial distribution and orientation of subsurface strain. I also explore how the two models complement each other, and provide more constraints for fracture modelling.

Trishear uses kinematic approaches to model fault-propagation folding. The model generates a triangular shear zone from the tip line, where the deformation produced by the fault displacement is accommodated upwards (Hardy and Allmendinger, 2011). Elastic Dislocation (ED) modelling is a geomechanical approach to estimate the distribution of subsurface strain, which can be used to predict the intensity and nature of the fractures associated with large faults (Dee et al., 2007).

After careful interpretation of the seismic data, the interpreted and depth converted geological horizons were the input for the trishear model. 2D inverse trishear modelling (Cardozo & Brandenburg, 2014) helped reconstructing the fold forelimb, thrust tip, and footwall geometry. This also delivered parameters such as fault propagation, fault slip, and finite strain. Thrust and horizons surfaces reconstructed in trishear were imported to TrapTester (Badleys) to perform Elastic dislocation modelling (ED). This geomechanical technique helped validating the trishear predictions. The ED technique, also delivers strain tensors. Stress tensors were computed from the ED strain tensors using appropriate rock properties. The outputs provided for both models are used as proxies for the orientation and distribution of fractures in the anticline. The results are compared against the well fracture image-logs and previous studies at Teapot Dome.

I am aware there is some circular reasoning in this process, i.e. modelled trishear surfaces were fed into the ED model to compare these two methods. However, without complete coverage and imaging of the entire structure, this helps testing the complementarity of the methods, and

also highlights the limitations of one procedure or the other. This is also the first time the application of both trishear and elastic dislocation techniques is evaluated in detail for a relatively simple, although unfortunately incomplete, structure. These results contribute to a better understanding of the spatial distribution and orientation of fractures at Teapot Dome, and emphasize the importance of using structural modelling techniques in DFN generation, and not just statistical or seismic-attributes based techniques.

2 Geologic setting

The Laramide orogeny was produced by collision of the Farallon and North America plates from the Late Cretaceous to the Paleocene. The Laramide and Sevier orogenies partly overlapped in time in the central Rocky Mountains area, where the Cretaceous Sevier orogen is characterized by thin-skinned deformation, while the Laramide orogen is characterized by deep-seated, thick-skinned thrusts (Coney, 1972; Dickinson & Snyder, 1978; Snyder *et al.*, 1978; Spieker, 1946) (Figure 4). The Laramide orogen is expressed by basement-cored uplifts that mostly trend NW-SE, and separate several broken foreland basins. The axes of these basins trend sub-parallel to the uplifts (Figure 1). (Dickinson & Snyder, 1978; Gao *et al.*, 2011).

The central Rocky Mountains near the southwestern edge of the Powder River Basin display the greatest deformation in response to the Laramide uplift (Fox, 1991). Unlike the southern Rocky Mountains, the deformation in the central Rockies was distributed over a much broader area, since it was dominated by thrusting instead of strike-slip deformation (Cather *et al.*, 1990). The Teapot Dome is part of a large Laramide structural complex of basement-cored anticlines located in the central Rocky Mountains area.

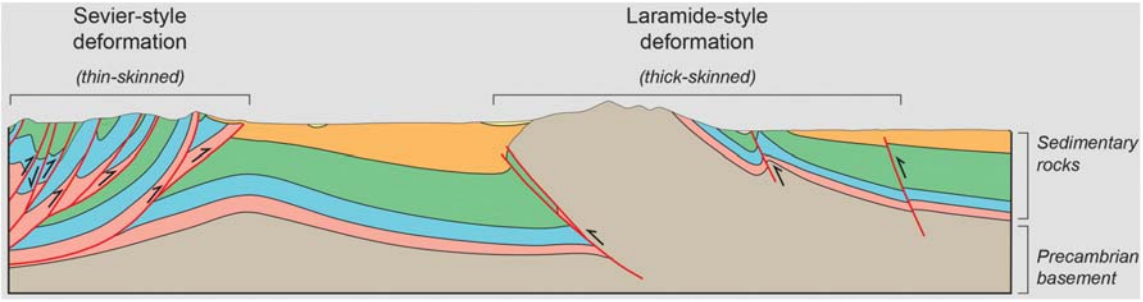

Figure 4 Difference between the structural styles of the Sevier (thin-skinned) and Laramide (thick-skinned) orogens. Modified from Wyoming State Geological Service.

2.1 Structural Geology

The Teapot Dome is a 12 km long, doubly plunging, basement-cored, Laramide anticline. The curvilinear anticline axis trends NW-SE, and the western flank (~30° W dip) depicts steeper dip angles than the eastern flank (~10° E dip) (Figure 5 and Figure 6a). The width of this thrust-related anticline is about 6 km and the hanging wall has an amplitude of ~800 m. Whereas near the basement, the west-southwest vergent fold is highly asymmetric and tight in response to the horizontal compression, it becomes more symmetric and less tight up-section (Lorenz & Cooper, 2013). A similar geometry is observed in the studied 3D seismic survey along the anticline's axis; the fold becomes less asymmetric and less tight towards the southern and northern fold terminations.

The Teapot anticline is the result of basement-cored uplift and reverse motion over a high-angle west-southwest vergent thrust (Wilson *et al.*, 2015) developed as a consequence of oblique horizontal compression (Lorenz & Cooper, 2013). The deep thrust with 35°-40° east-northeast dip (Chiaramonte *et al.*, 2011; McCutcheon, 2003), displaces the crystalline Precambrian granite, offsets the Paleozoic sediments and terminates in the Cretaceous sedimentary succession (Lorenz & Cooper, 2013) (Figure 6a). The anticline is segmented into compartments by normal-oblique and strike-slip faults rotted in the basement (Chiramonte *et al.*, 2011). At the surface, Cretaceous strata show evidence of vertical strain partioning resulted from extension and expressed by folding, extensional fracturing and normal faulting (Lorenz & Cooper, 2013).

Several authors (S. P. Cooper *et al.*, 2006; Doll *et al.*, 1995; Olsen *et al.*, 1993; Wilson *et al.*, 2015) have identified the presence of a major set of extensional fractures and normal faults in the eastern limb of the anticline striking perpendicular, oblique and parallel to the fold axis. These structures are characteristic of Rocky Mountain anticlines (Spieker, 1946; Thom, 1931). The structural control exerted by faulting and fracturing has played an important role in the permeability of the reservoir units at Teapot Dome. The Tensleep sandstone is considered an unconventional, natural fractured reservoir (NFR). Cooper *et al.* (2006) documented three fracture sets at Teapot Dome based on the fractures trends relative to the fold axis trend: The hinge-parallel fractures is the major set observed in surface exposure followed by hinge-perpendicular and hinge-oblique sets. The latter is considered as the regional fracture set occurred before Laramide orogeny. Based on observed fracture patterns in image-logs from

wells (included in the present study), Lorenz & Cooper (2013) suggested that the maximum horizontal compressive stress was oblique to the north-northwest striking thrust at deeper horizons. Using the same wells, Wilson *et al*., (2015) determined that west-northwest trending open fractures is the dominant set in the main reservoir unit (Tensleep Sandstone) at Teapot Dome, and corresponds to the hinge-oblique set reported by Cooper et al. (2006). Both Lorenz & Cooper (2013) and Wilson *et al*., (2015) found that the drilling induced open fractures set trends N76W in average, parallel to the present-day maximum horizontal compressive stress (Wilson *et al*., 2015).

2.2 Stratigraphy

The thickest section of the Powder River Basin is about 5.5 km thick. The uppermost 2.4 km of this section correspond to non-marine and clastic sediments deposited from Cretaceous to Tertiary (Fox *et al*., 1991). The Teapot anticline folds almost 3 km of non-marine sandstones, clastic and carbonates deposited from the Devonian to the Cretaceous (Figure 6). The Devonian sediments unconformable overlay the Precambrian Granite basement (Knittel *et al*., 2004). At the Naval Petroleum Reserve (NPR-3), nine oil-bearing and six water-bearing units are in the stratigraphic succession (Friedmann & Stamp, 2006). These units have been target of enhanced oil recovery operations using CO2 injection (Nummedal *et al*., 2003).

The shallowest oil reservoir at NPR-3 is the Upper Cretaceous Shannon Formation (Cooper, 2000). The Pennsylvanian Tensleep Sandstone Formation contains the most important reservoir. This Formation consists of 300 ft (~100 m) of eolian sandstones interbedded with dolomites (Li, 2014; Zhang, 2007), and is overlaid by cap rocks consisting of a mixture of sandstones, siltstones and shales of the Goose and Chugwater formations (Wilson *et al*., 2015). The average porosity of the Tensleep sandstones is 8%, and the permeability is about 80 md (Friedmann & Stamp, 2006).

The stratigraphic succession at Teapot Dome can be mapped on the surface, and in the subsurface using the 2D and 3D seismic data and wells utilized in this study. Cooper (2000) conducted a field study of the fractures in the Parkman Sandstone Member of the Mesaverde Formation (Figure 5 and Figure 6). The Mesaverde Formation is exposed within a resistant rim along the fold curvature, it dips about 30° in the western limb and between 7° and 14° in the eastern limb (Figure 5 and Figure 6a) (S. Cooper, 2000). In this study, I focus in five

stratigraphic intervals defined by five seismically observed Formation tops (Figure 6b): The top of the Devonian sandstones of the Freemont Canyon Formation, the Tensleep Formation top, the Crown Mountain Member top, and the Dakota Formation and Second Wall Creek Sandstone Member tops. The sedimentary intervals between these tops consist of predominantly more competent Paleozoic and Lower Cretaceous units, relative to the more shaly Upper Cretaceous units above.

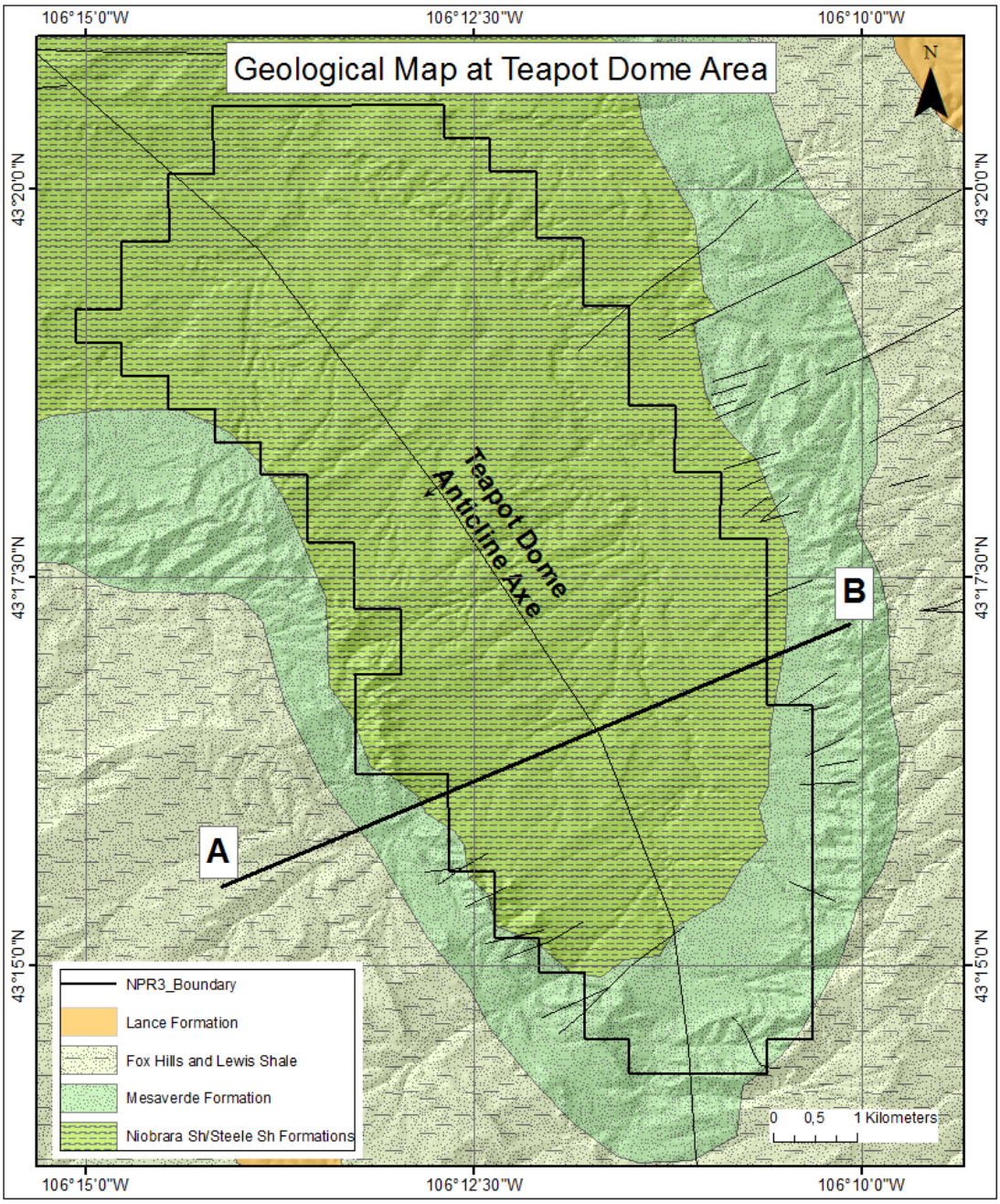

Figure 5 Geological map of Teapot Dome. See the legend for the name of the units. Thin black lines indicate the fold axis and faults. Notice the set of fractures and faults in the Mesaverde Formation on the eastern limb of the anticline. Hill shade and contours from ArcGis Online, owner: azolnai, source: RMOTC. Shape files of geological contacts and structures modified from The Wyoming State Geological Survey.

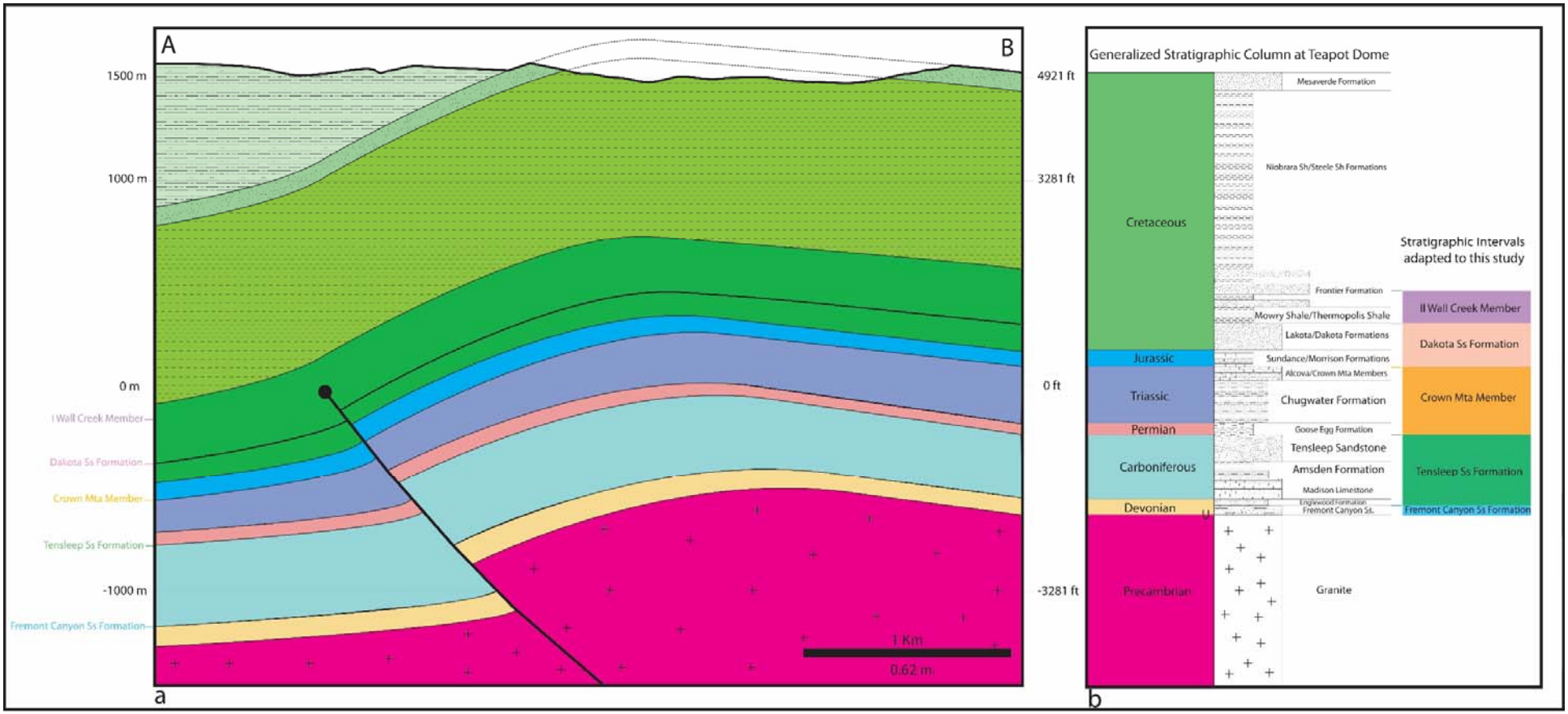

Figure 6 ***a****. Cross-section of the Teapot anticline and its stratigraphic units. Figure 5 shows the location of the section;* ***b****. Generalized stratigraphic column of Teapot Dome. Adapted from (RMOTC, 2005a, b) and (Wilson et al., 2015). The simplified column at right in b are the stratigraphic intervals used in this study.*

3 Dataset

This study is based on a public domain dataset of Teapot Dome provided by the Rocky Mountain Oilfield Testing Centre (RMOTC, 2005a, b). An ArcGis (Esri) Geodatabase (storing shape and raster files) contains all the information required to construct geologic and base maps of the area. The coordinate system is NAD 1927, Wyoming State Planes, East Central Zone, U.S. feet. The geographic information consists of wells and seismic lines positions, topography, and geological contacts among others. A quick display of the georeferenced elements provides a clear picture of the spatial distribution of the data, which facilitates the classification, selection and presentation of the information (Figure 7).

The post-stack seismic cube consists of 188 cross-lines and 345 in-lines with a seismic bin spacing of 110 ft. The polarity is normal and the survey covers an area of about 72 km² with maximum two way-travel time of 3000 ms. Strong reflectors clearly depict part of the anticline geometry, the east dipping backlimb and the fold axis. However, the west-vergent thrust, the steeper west dipping limb (forelimb), and the footwall are poorly imaged or not imaged at all (Figure 8a).

Four normalized, migrated, 2D seismic lines trend NE-SW, almost perpendicular to the anticline's axial trace (Figure 7, lines B-D). Another 2D seismic line runs almost parallel to the anticline's axial trace in a NW-SE direction (Figure 7, line A). These lines have different lengths. Line A is ~16 km long, lines B and C, 5 km long, line D is 7 km long, and line E is the shortest line with 4 km length. Line D is the seismic section that best covers and depicts the geometry of the anticline except for the wipeout zone in the steep forelimb of the structure (Figure 8b).

Time-depth relationship tables and a synthetic seismogram provided in the dataset were instrumental in the time-to-depth conversion of the seismic data. The drilling database contains about 1400 well headers (Figure 7). Most of them have their corresponding directional well survey, formation log tops and LAS files. Four wells drilled along the fold hinge provide formation microimaging (FMI) logs and FMI image interpretations (Figure 7). Wireline Log curves and fracturing data through the Tensleep sandstone reservoir are displayed in Figure 9.

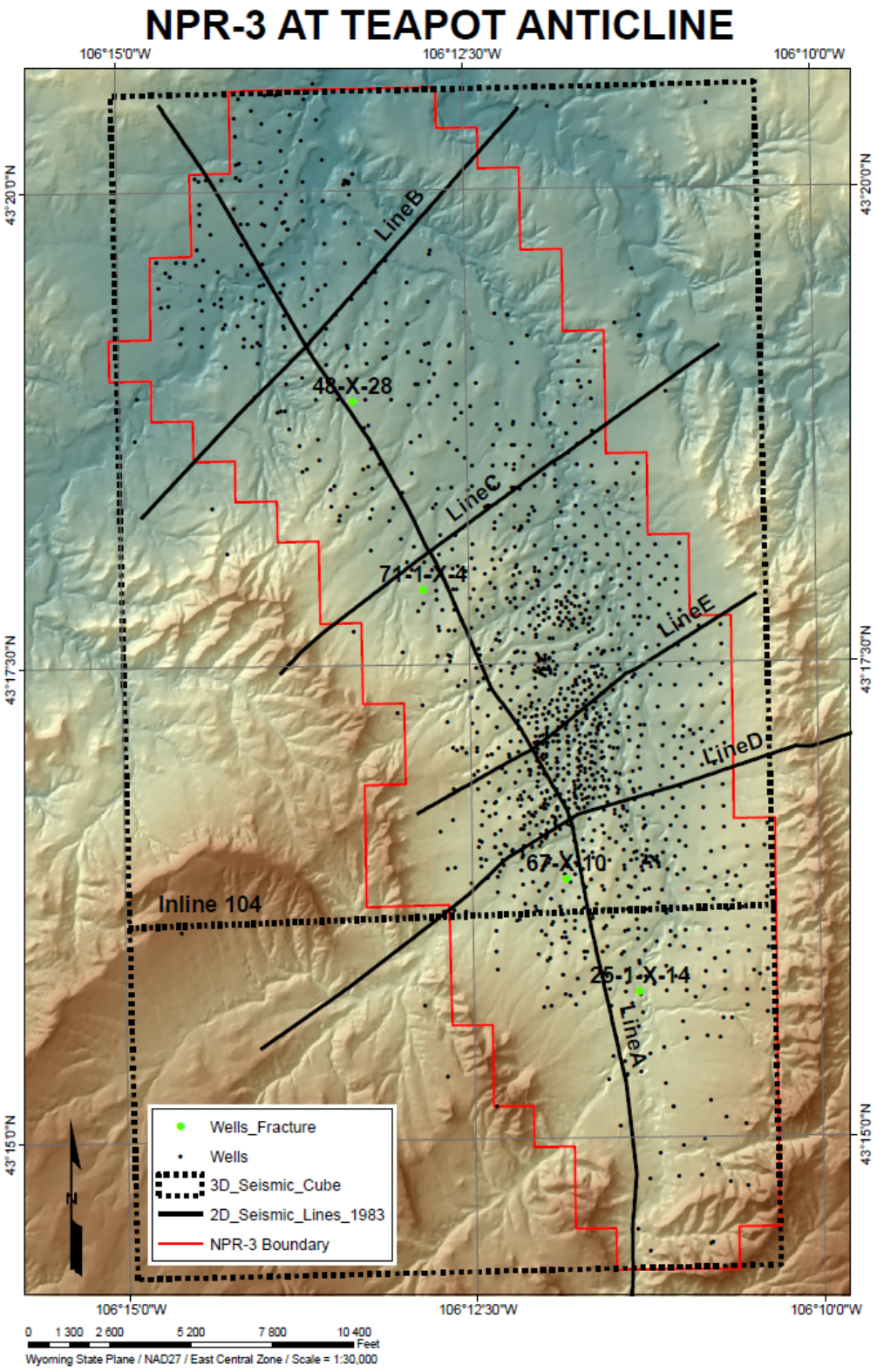

Figure 7. Base map of NPR-3 (Naval Petroleum Reserve) at Teapot anticline (modified from RMOTC). Location of the seismic cube survey (dotted black polygon) and 2D seismic lines (solid black lines), NPR-3 (solid red polygon), and wells (black dots). Green dots are four wells with fracture data.

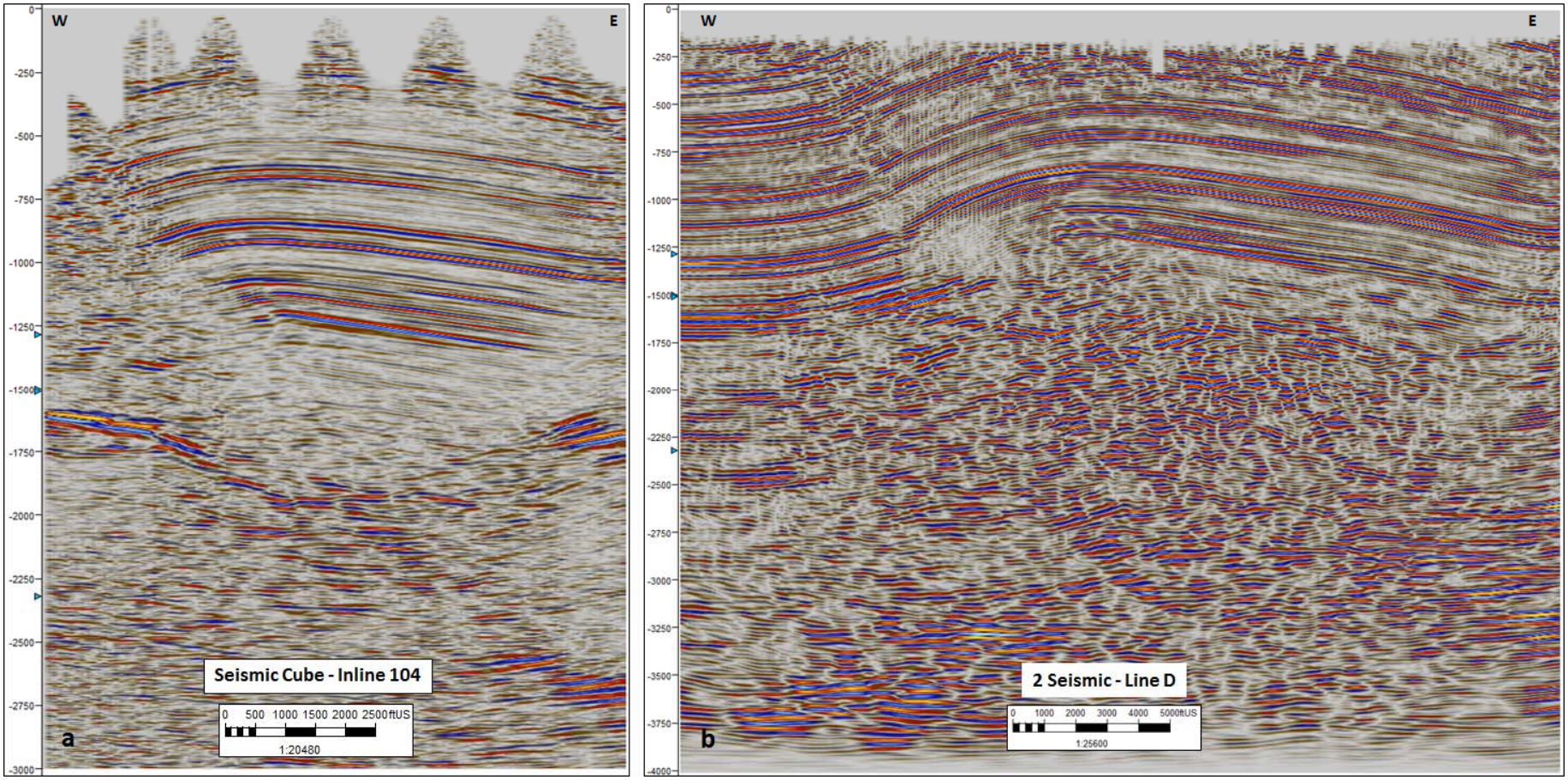

Figure 8 **.** *Seismic sections in time domain (ms) depicting the geometry of the Teapot anticline. The sections are almost perpendicular to the anticline's axis (see Figure 7 for location)* ***(a)*** *Inline 104 from the 3D seismic cube. Note the poor reflector imaging at the western side where the forelimb and footwall of the structure are located* ***(b)*** *2D seismic line D through the Teapot Dome. Note wipe-out area at the steep forelimb areas close to the thrust tip.*

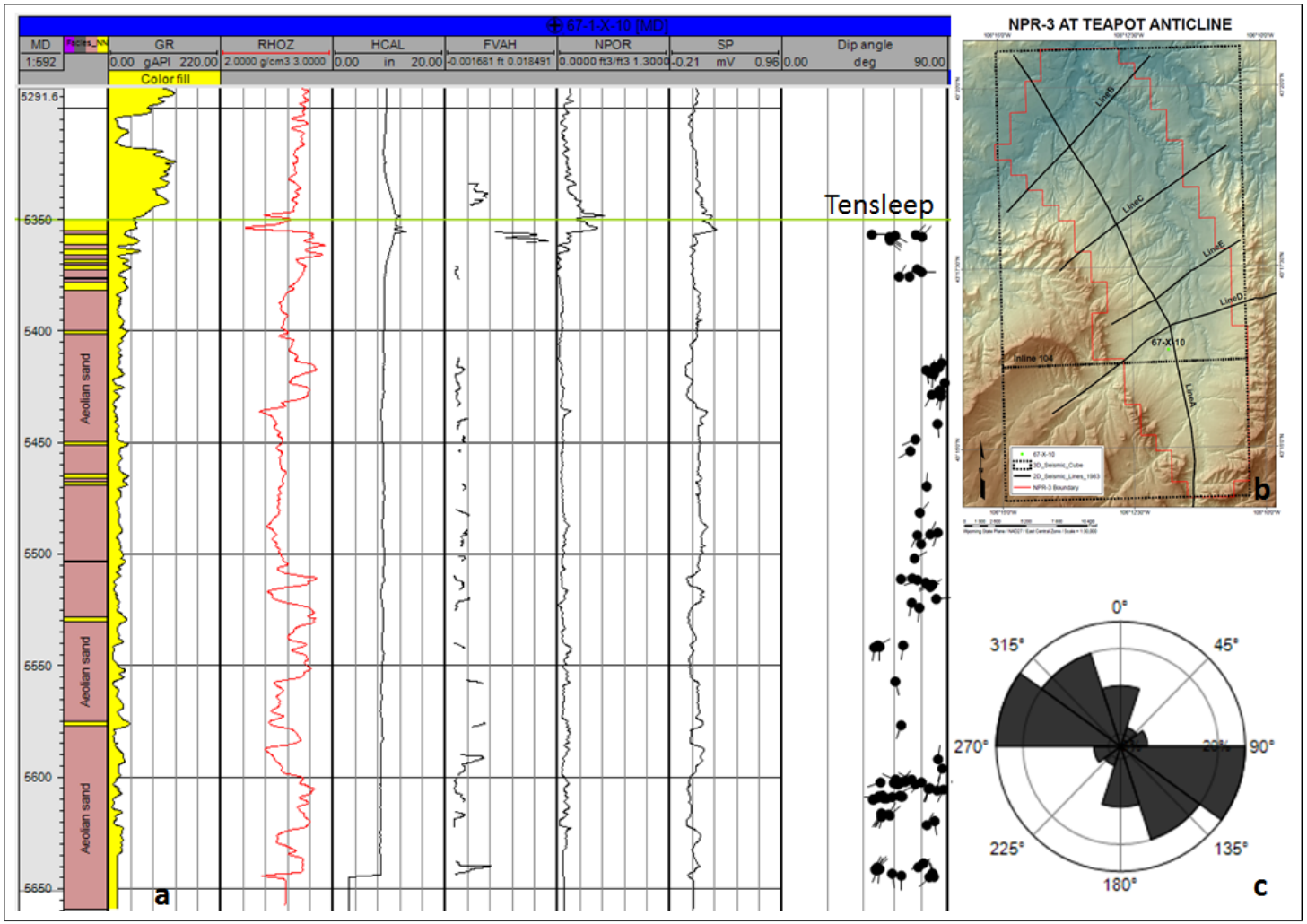

Figure 9 Example of well log information in the Tensleep sandstone. ***(a)*** *Wireline curves and Tap poles (dip and dip direction of fractures) in well 67-X-10.* ***(b)*** *Location of well 67-X-10.* ***(c)*** *Rose diagram displaying the strike of the fractures.*

4 Methodology

In order to achieve the objectives of this study, four main steps were followed: 1. Data set analysis and seismic interpretation; 2. 2D trishear inverse modelling; 3. 3D structural model generation; and 4. 3D elastic dislocation modelling. This study focuses on the structural modelling (kinematic and geomechanic) of seven horizons and the master thrust responsible for the Teapot anticline. (Figure 10) is a general illustration of the workflow.

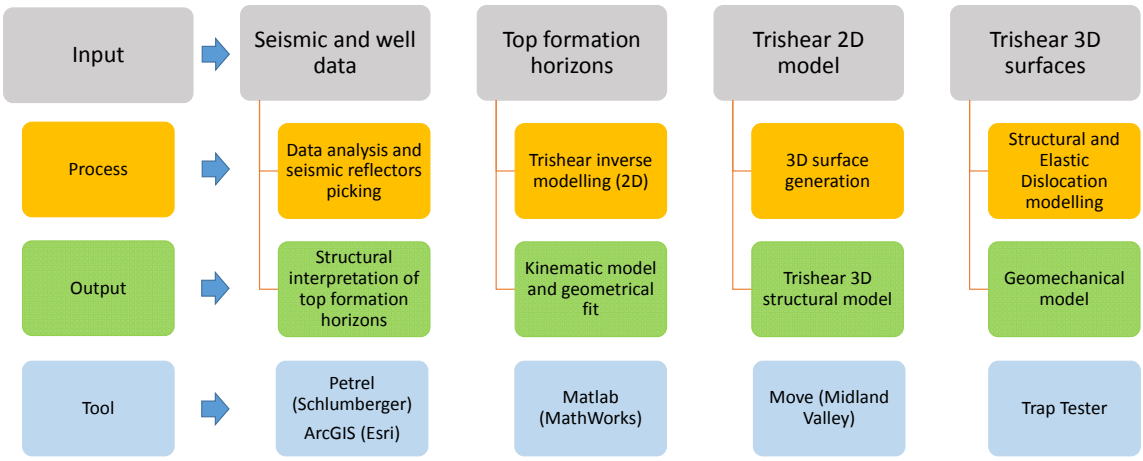

Figure 10 Workflow for kinematic and geomechanical modelling of the Teapot Dome.

4.1 Data Set Analysis and Seismic Interpretation

This step is sub-divided in four parts: 1. Quality control, data filtering and data selection; 2. Seismic to well tie; 3. Seismic reflector picking and surface generation; 4. Time to depth conversion.

1. The quality control consisted in a general check of the dataset. Excel and GIS databases containing wells with the associated drilling and geologic information such as directional well survey, formation well tops, e-logs, synthetic seismograms, and time-to-depth relationship were compared. The well information was filtered considering as much as possible the coverage of the whole stratigraphic sequence, the functionality of the e-logs in the generation of synthetic seismograms, and the implementation of a velocity model. The availability of fracture data was considered as well. The Excel well database consists of 1317 well headers and the GIS database of 1401 wells. 87 wells were selected for this study. The deepest well is 7180 ft (2188 m) deep,

the shallowest is 4000 ft (1219 m) deep, and the average depth reached by the selected wells is ca 5000 ft (1524 m, Figure 11). Only one well touched the basement at 6864 ft (2092 m) depth (Figure 12).

2. Synthetic seismograms of 11 wells were generated to tie the seismic survey to the wells and correlate well tops with seismic reflectors representing the tops of geologic formations (Figure 11). All selected wells include density and sonic logs. A provided composite synthetic seismogram (RMOTC, 2005a, b) and the interpretation by (Wilson *et al.*, 2013) were used as guidelines to identify the seismic reflectors. The reflectors correspond to the tops of the Freemont Canyon Sandstone Formation, Tensleep Sandstone Formation, Crown Mountain Formation, Dakota Formation, and Second Wall Creek Member of the Frontier Formation (Figure 12). Two additional continuous reflectors with strong-amplitude were included with the objective of having more control on the formations tops correlation. These reflectors are the negative-amplitude B1 reflector, which is positioned between the Crown Mountain Formation and the Dakota Formation top reflectors, and the positive-amplitude R3 reflector, which is above the Second Wall Creek Member top reflector (Figure 12)

3. First, it is important to note that the seismic interpretation only focused on the top formations horizons. The major thrust and other minor faults were not picked on the seismic since further steps in the workflow provide ways to predict the geometry of the major thrust plane.

Careful picking of the reflectors mentioned in the previous step took place over the migrated seismic data in time domain. Top horizons were picked along every fifth inline and crossline of the seismic cube and along four 2D seismic section lines (B, C, D and E) (Figure 13). Then, the geological 3D surfaces were generated for every picked horizon. These surfaces were fundamental in the generation of the velocity model used for time to depth conversion. A structural isochrone map of the top of the Tensleep Formation is presented in (Figure14).

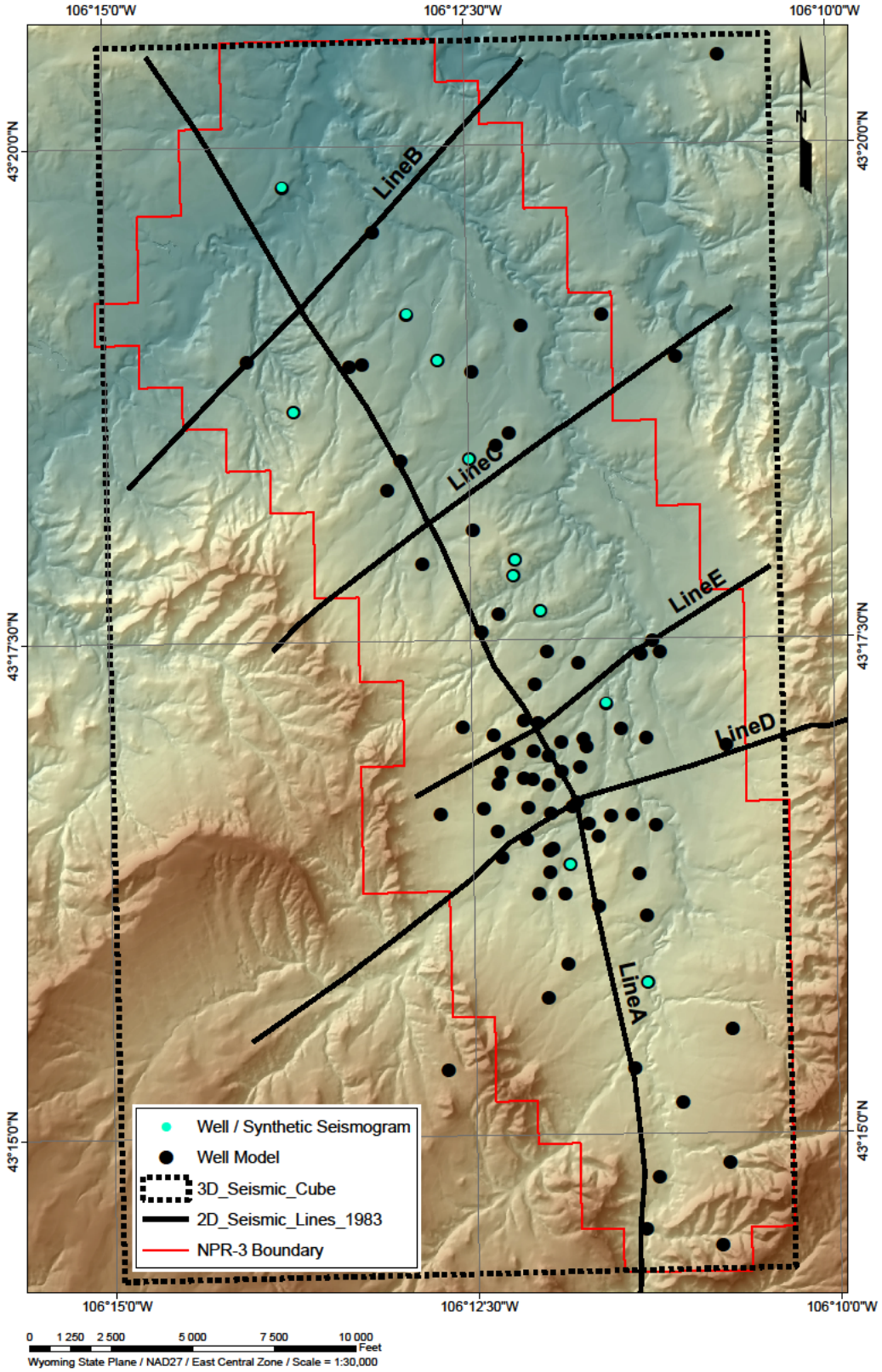

Figure 11. Geographic distribution of wells used in this study. Note the distribution and positions of the wells with synthetic seismograms (green dots).

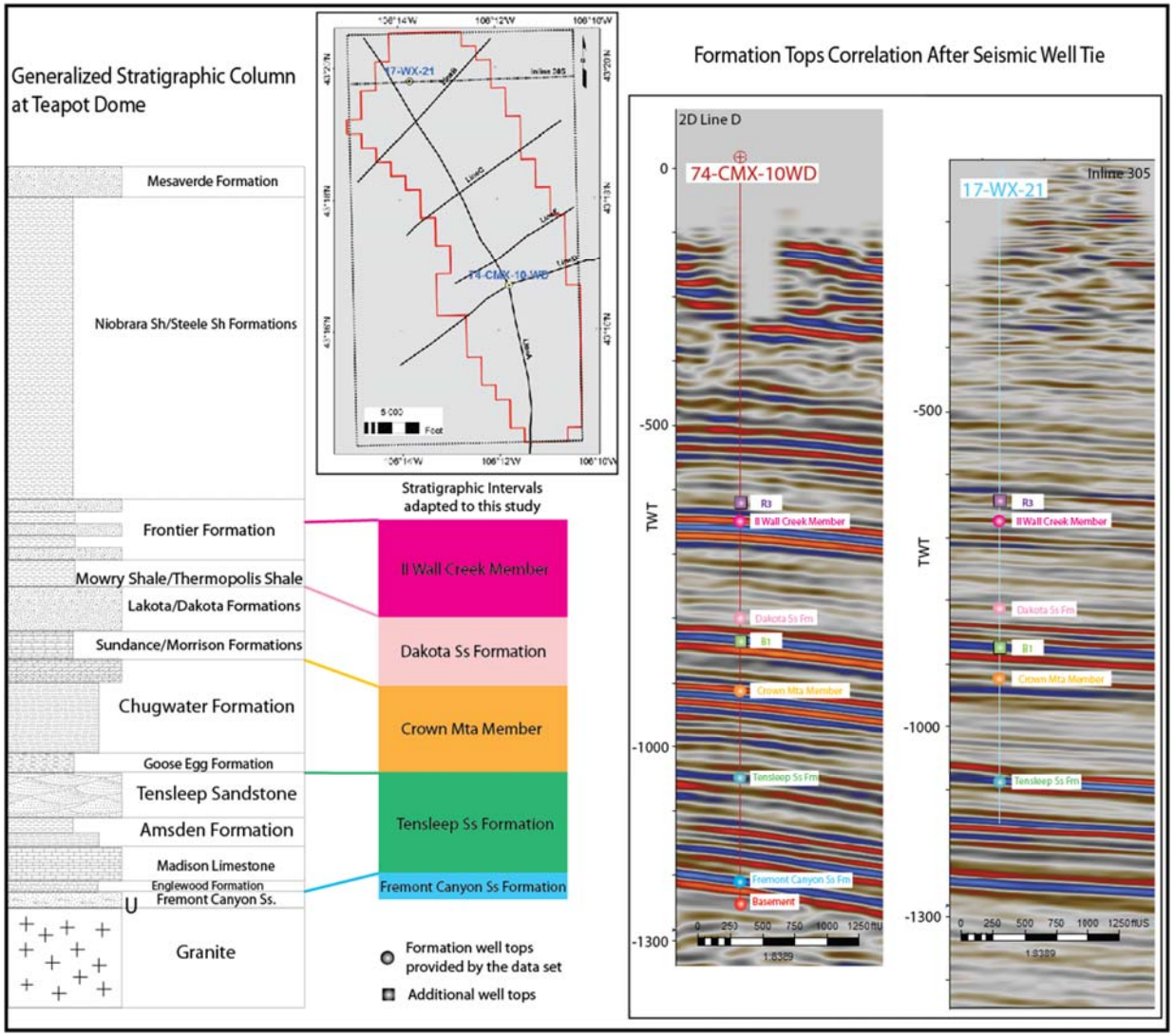

Figure 12 Seismic to well tie. On the left, generalized stratigraphic column. In the centre, stratigraphic intervals for this study. On the right, results of the seismic well tie. Well 17-WX-21 is tied to inline 305 through a synthetic seismogram, while well 74-CMX-10 WD is tied to 2D line D. Inset map shows the location of the wells.

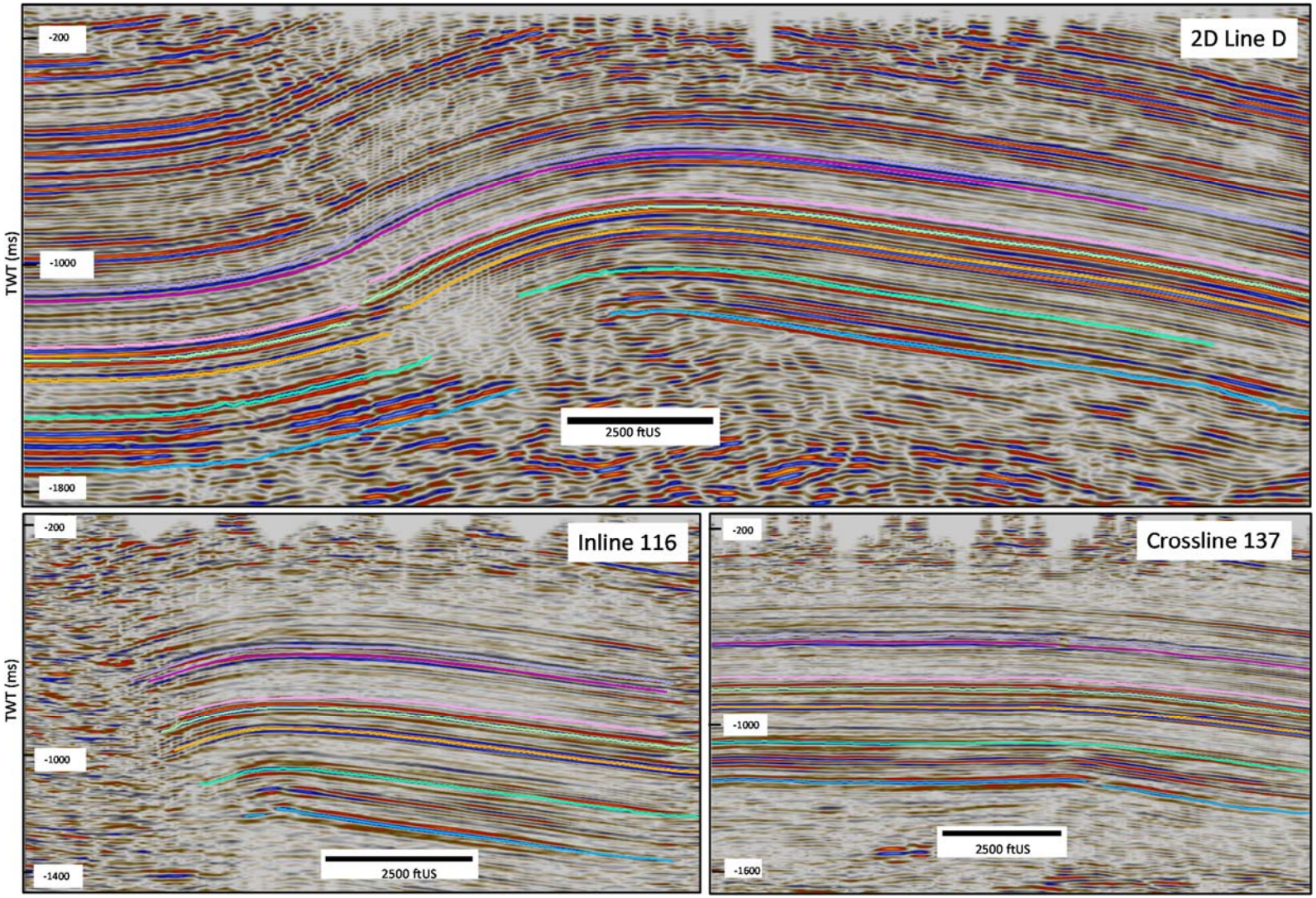

Figure 13 Seismic interpretation of the selected tops on the migrated stack seismic data. From bottom to top: Freemont Canyon Formation (blue), Tensleep Formation (green-blue), Crown Mountain Member (orange), B1 reflector (green), Dakota Formation (pink), Second Wall Creek Sandstone Formation (magenta) and R3 reflector (violet).

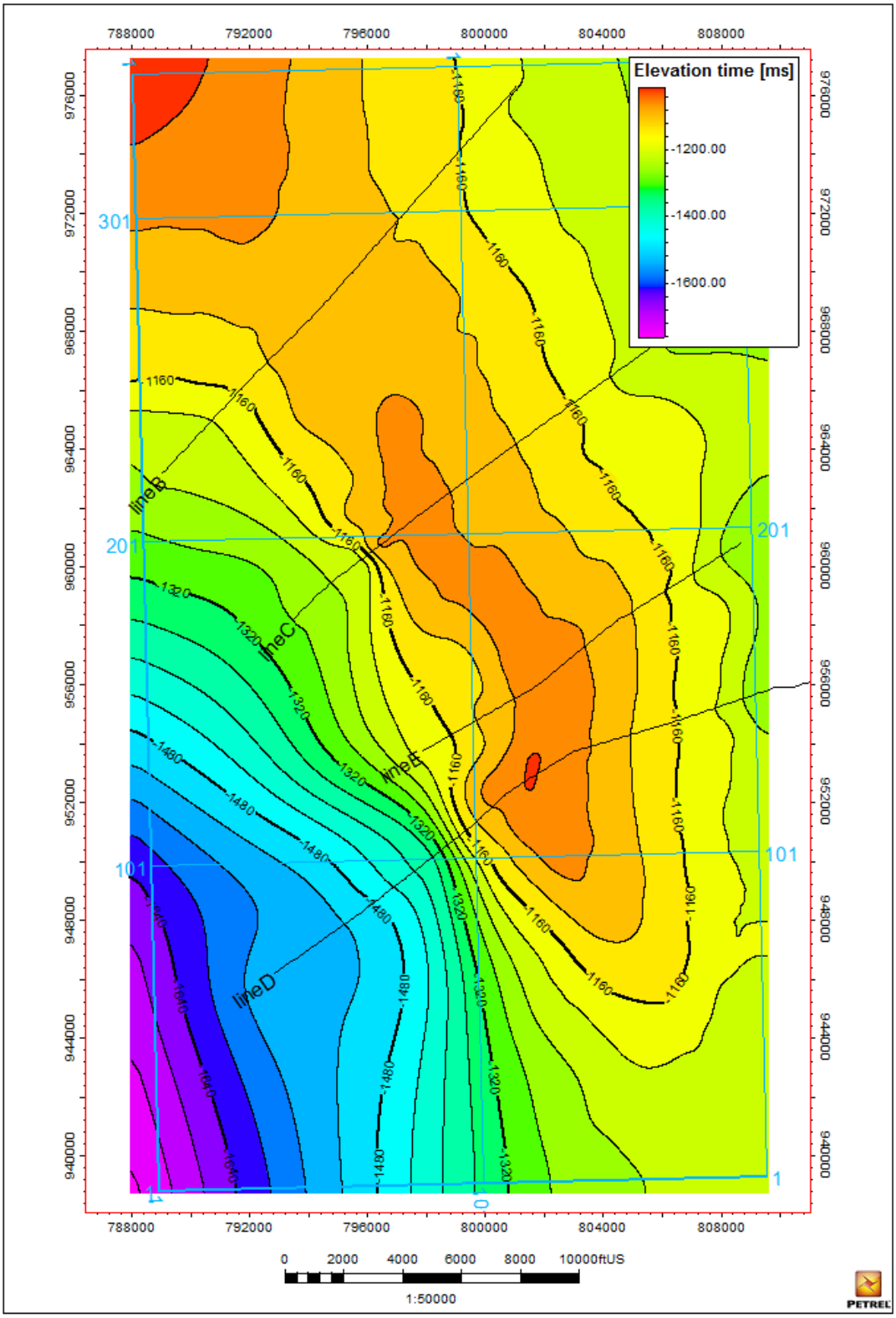

Figure 14 Structural isochrone map in two-way travel time (ms) of the top of the Tensleep Formation, the main reservoir at Teapot Dome.

4. Time to depth conversion was a fundamental step for structural modelling. A detailed construction of the 3D time-domain geological surfaces, the calculation of the time-depth relationship curves, and reasonable stratigraphic correlation of the formation well tops, support the velocity model generated in this study

To acknowledge the uncertainty and lateral variation of the velocity, two velocity models with good well control were generated. The second model was derived from the first one, which was produced using the same wells (11) used in the synthetic seismograms generation. The shallowest well is 4000 ft (1219 m) deep, the deepest is 6000 ft (1828 m), and the wells average depth is ca 4800 ft (1463 m). Additionally, five time horizons were loaded as base surfaces in the calculation, four correspond to geologic horizons (Tensleep, Crown Mountain, Dakota and R3), and one is a computed surface coinciding with the seismic acquisition datum. Well tops correction was applied to the four geologic horizons. An important result of the first velocity model is the generation of time-to-depth curves under each well loaded in the project, that is the 87 wells included in the project contain time-to-depth tables from the first velocity model. The second velocity model was generated using all these 87wells, including those with synthetic seismograms. The same five horizons in time domain, and the well tops velocity corrections used in the first model, were used in the second model as well.

The geological surfaces in time domain, the high density and fairly uniform distribution of the wells with their respective well tops, helped accounting for the lateral velocity variations and their uncertainty. The spatial distribution of the wells plays an important role in the velocity model. The 11 wells with synthetic seismograms are located close to the crest of the anticline, mostly in the backlimb and trending sub-parallel to the fold axis. The rest of the wells are fairly disseminated but cluster in the crest between the seismic lines E and D (Figure 11). Based on this, the near crestal area with higher well population is the one where the velocity model has the highest confidence. Conversely, areas with limited well control such as the southern and northern fold terminations have the lowest confidence in the velocity model (Figure 11).

4.2 Trishear Inverse Modelling (2D)

The objective of this step is the geometric reconstruction of the forelimb, the major thrust fault, and the footwall, considering the poor seismic imaging of these structural elements (Figure 2). Trishear is a suitable kinematic model for fault-propagation folding, including basement-cored

anticlines (*e.g.* Teapot Dome). The input data for trishear modelling is a set of 2D profiles across the anticline (Figure 15a-b), striking orthogonal to the fold axis. Each cross section contains the interpretation of the top horizons. Inverse trishear modelling consists of unfolding these geological horizons by running the trishear model backwards. The best-fit model is the one that best restores the folded horizons to straight lines (Figure 15c). Forward modelling using the best-fit model parameters provides the fold geometry, the thrust geometry, and finite strain ellipses (Figure 15d).

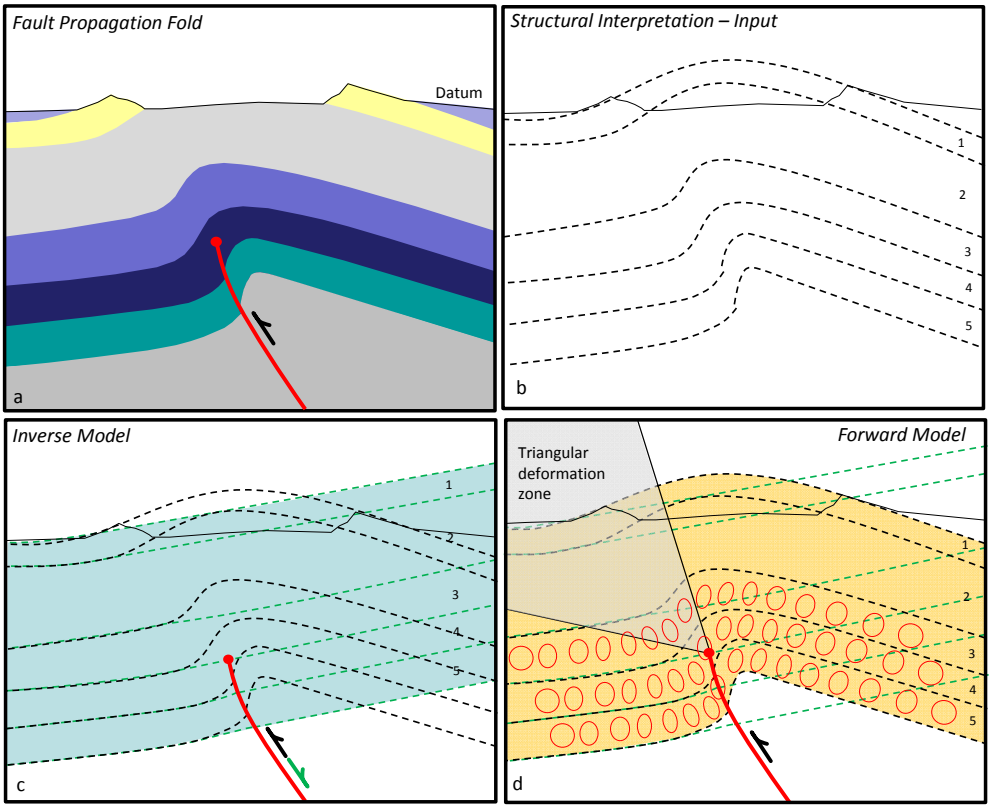

Figure 15. Cartoon showing the trishear inverse modelling technique. a. Fault propagation fold. b. structural interpretation. c-d Inversion and forward modelling to predict the structure geometry and finite strain

The best-fit horizons depict the reconstructed structure in each cross-section. They also serve as geological controls for the further 3D geologic surface generation. Hence, the accuracy of the generated 3D surfaces depends on the number of cross sections used in 2D trishear modelling and the spacing between these sections. In this study, eight cross-sections were modelled with trishear and their results were used to generate the 3D model of the anticline. Four of these sections correspond to the same position of the 2D seismic sections B, C, D and E initially provided in the dataset (Figure 11). The other four sections S1, D2, C1 and B1 (Figure

16) were derived as 2D composite seismic lines from the depth converted 3D cube. These four sections were interpreted in depth by picking the key seismic reflectors as in the previous step.

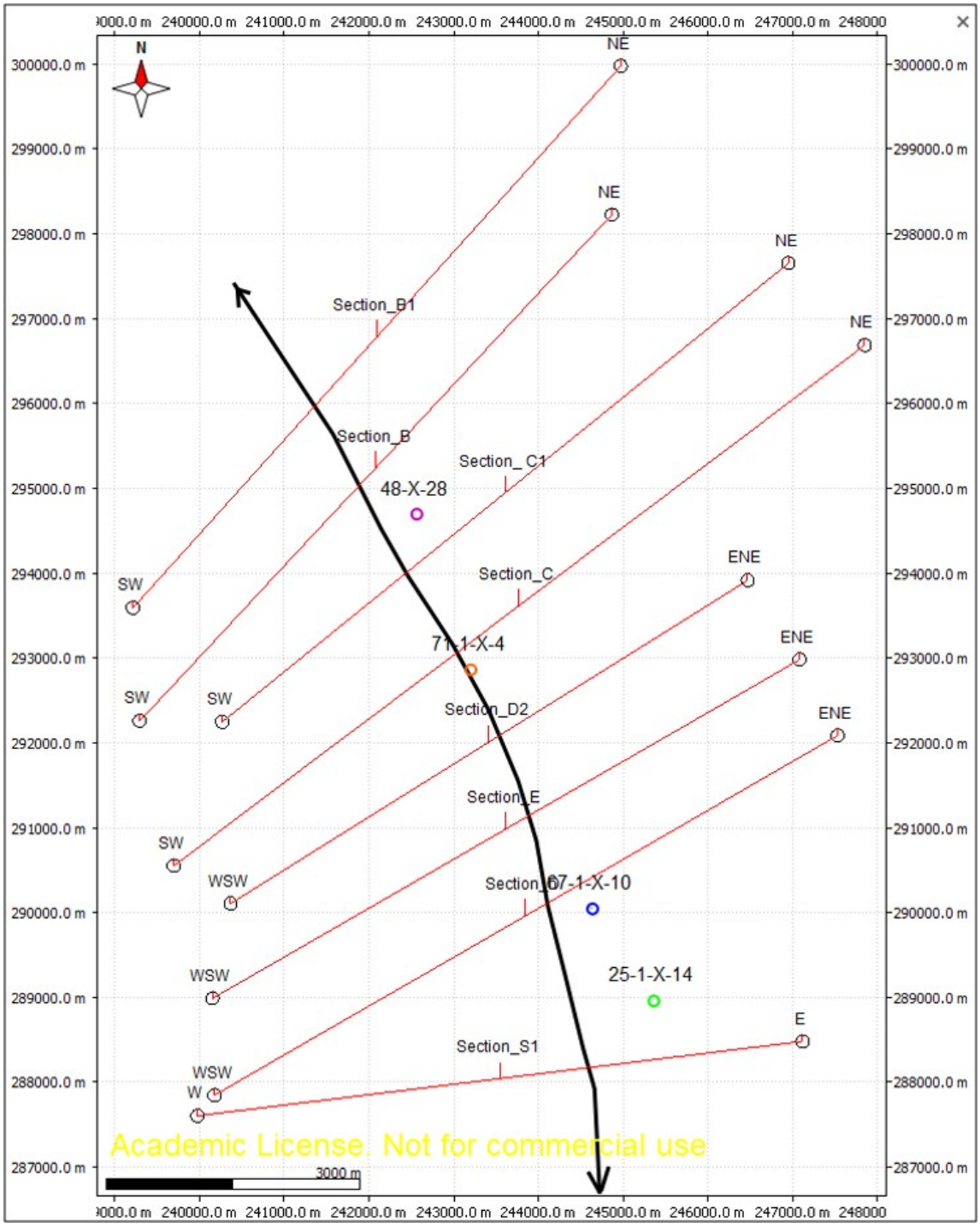

Figure 16. Eight cross sections used in 2D trishear modelling. Section are oriented almost perpendicular to the fold hinge.

Depth converted horizons interpreted along the selected sections were exported from Petrel to Move. Then, the horizons were loaded into Move's cross sections where it was possible to plot the horizons in both the model coordinate system and a local coordinates system for each section . The horizons were exported from Move as ASCII plain text documents with local cross-section coordinates X representing the length of the section line with origin at zero, and Z representing the elevation in meters. Seven ASCII files (one per horizon) were the input data to the 2D inverse trishear algorithm, in each section.

The backlimb of the Teapot dome gently dips to the east. A planar thrust would not be able to produce this backlimb geometry in trishear. Therefore, the inverse trishear algorithm applied in this study uses a listric thrust fault. The algorithm uses inclined shear in the backlimb as in Cardozo & Brandenburg (2014) (Figure 17). However, since the detachment is not clearly imaged, this study only focuses in the shallower and steeper thrust locations rather than the deeper locations where the thrust might be sub-horizontal.

The codes for trishear inversion were implemented by Nestor Cardozo in Matlab. These consist of a combination of functions and scripts that use the text files of the horizons' geometry as input data to produce best-fit models stored in Matlab files. The algorithm predicts the geometry of the listric thrust by drawing a circular arc segment from a user-selected current fault tip area, and proportional to the best-fit fault slip. The radius of the circular arc is also input by the user based on the approximate (or interpreted) location of the current fault tip and the thrust geometry close to its tip. A text file containing the estimated (or guess) coordinates (x and y) of the fault tip and the radius of curvature was generated for each cross-section. This file also contains the uncertainty of these parameters. The cross sections were loaded into the program Intaglio, where the possible fault tip location and the radius of curvature were measured. (Figure 17) shows how the algorithm calculates the circular arc that represents the trajectory of the listric fault in the cross section.

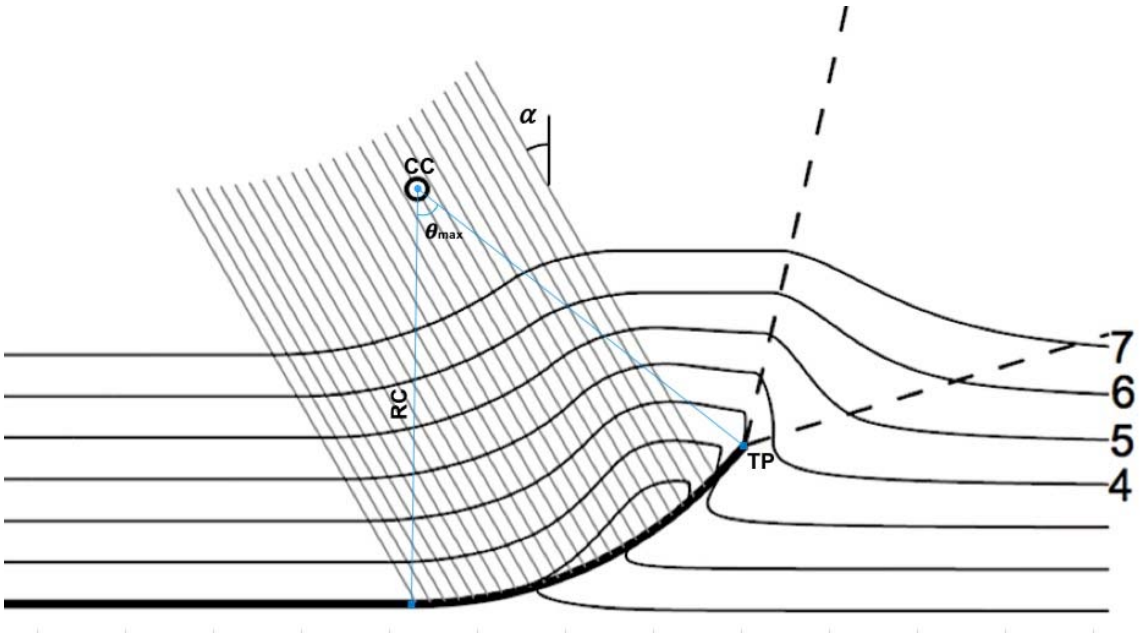

Figure 17 Illustration of how the algorithm works to construct the thrust geometry. Input data: radius of curvature (RC) and location of fault tip point (TP). Centre of curvature (CC) is computed by the algorithm. Note the incline shear angle α in the backlimb, and the maximum central angle θ. After Cardozo & Brandenburg (2014)

2D trishear deformation is calculated from the combination of six model parameters related to the fault geometry and its propagation (Allmendinger, 1988; Cardozo *et al*., 2011). These, together with the angle of shear in the backlimb, result in a total of seven parameters for the inversion. The user searches for the most suitable combinations of these parameters that honor the interpreted horizons (Cardozo & Brandenburg, 2014; Cardozo *et al.*, 2011). These best-fit models restore the beds to straight lines. The fit of any tested model is evaluated using an objective function that measures the departure of the restored beds from straight lines (Allmendinger, 1998). The trishear inversion algorithm uses global optimization, and specifically simulated annealing to determine the range of models that best fits the structure (the models with low objective function; Cardozo *et al*., 2011). Table 1 lists the model parameters and their ranges.

Table 1 Model parameters and their ranges in the trishear inversion. All parameters have the same ranges or uncertainties in the other sections. Centre of curvature coordinates and radius of curvature is for section D. The initial guess of the parameters is halfway between their minimum and maximum limits.

2D Trishear Paremeters Ranges			
Parameter		Range	Description
1	slmin	0.0	Minimum slip as proportion of slip in entire fault arc
	slmax	1.0	Maximum slip as proportion of slip in entire fault arc
2	tamin	40.0	Minimum trishear angle
	tamax	100.0	Maximum trishear angle
3	ccx	3150	Fault tip location in x (meters)
	ccy	0	Fault tip location in y (meters)
	tpuncer	100	Uncertainty in x and y of fault tip
4	maxarc	6000	Maximum radius of curvature (meters)
	maxarcuncer	500	Uncertainty in the radius of curvature length (meters)
5	psmin	1.0	Minimum fault propagation to fault slip ratio
	psmax	4.0	Maximum fault propagation to fault slip ratio
6	fdipmin	40.0	Minimum fault dip angle at tip point
	fdipmax	60.0	Maximum fault dip angle at tip point
7	ashearmin	0.0	Minimum angle of shear in the backlimb
	ashearmax	30.0	Maximum angle of shear in the backlimb

The algorithm works with thrusts dipping to the left (x coordinate increasing to the right). Therefore, the input horizons were horizontally flipped to fit this strategy (Figure 18c). I used the uppermost four beds (B1 to R3 reflectors, Figure 18b) in the inversion. 5,000 iterations were run to find the 100 models that best restore these horizons to straight lines (the 100 models with the lowest objective function). (Figure 19a) shows the best 100 models of the thrust and the four uppermost horizons compared to the interpreted horizons. The histogram charts (Figure 19b) show the frequency distribution of the shear angle in the backlimb, P/S, fault slip, and trishear angle for the 100 best-fit models. Further inversions based on these distributions might help to reduce the ranges of the parameters and get better fits.

The model with the lowest objective function is the one that best represents the geometry of the structure. (Figure 19c) shows the comparison between the predicted geometry using trishear and the horizons interpreted in the seismic lines. The predicted geometry of the thrust is also displayed. The table in (Figure 19d) shows the parameter values of the best-fit model.

After estimating the best-fit model for each cross-section, additional functions where ran to export the modelled horizons to Move. This operation was applied to both the restored and

deformed horizons. Since the forward model can calculate finite strain, one function was used to plot the strain ellipses and the initial circular makers. Lines of no finite elongation (LNFE) were drawn from the intersection points of the ellipses and circles. The LNFE can be used as proxies for the orientation of fractures (Allmendinger, 1998; Hardy and Allmendinger, 2011).

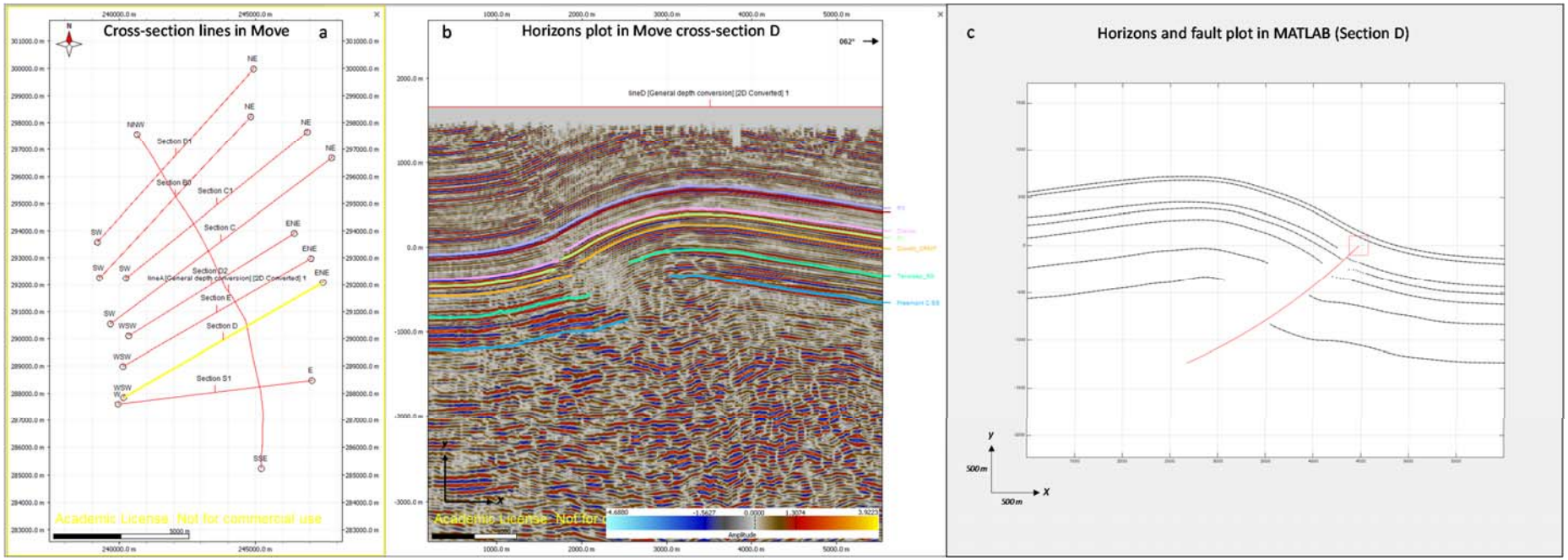

Figure 18 a. Map showing the location of section D. b. Cross-section showing the interpreted horizons along seismic line D in depth domain. c. Plot showing the same horizons of Figure 13b but flipped in the horizontal. This is necessary because the algorithm works with thrusts dipping to the left (x increases to the right). The trajectory of the thrust is also plotted. The red square represents all the potential positions of the fault tip. The size of this square is defined by the uncertainty in fault tip location (Table 1).

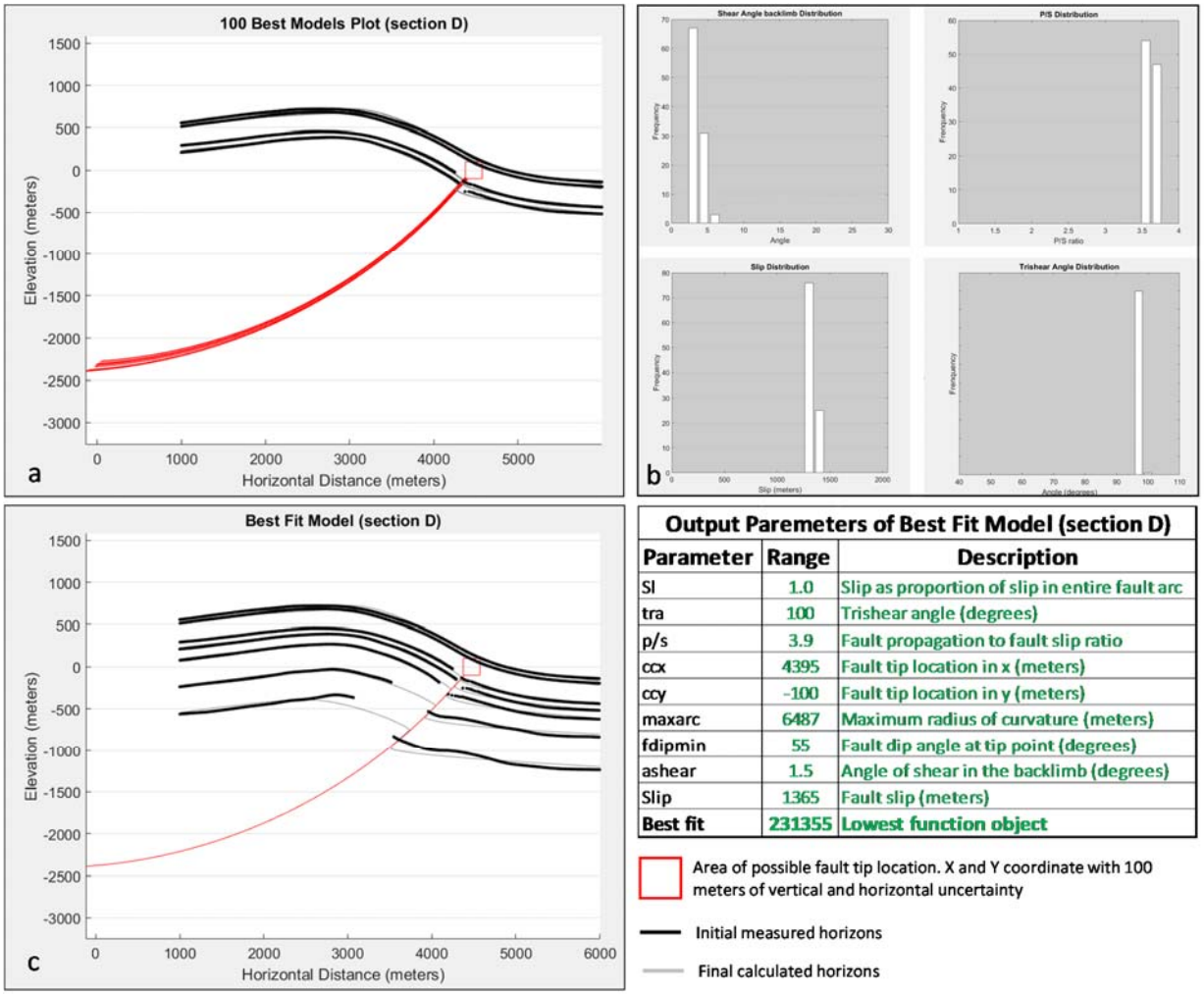

Figure 19 ***a****. Plot of the best 100 models for the four uppermost horizons and reconstructed thrust.* ***b.*** *Frequency distribution charts of the trishear parameters for the best 100 models.* ***c.*** *Plot of the best-fit model. Parameter values of the best-fit model in inset table. This example is for section D.*

4.3 3D Structural Modelling

Horizons and thrusts traces from trishear inverse modelling in 2D were imported into Move, where ordinary Kriging was applied to generate 3D surfaces for each geological horizon and the thrust (Figure 20). The initial thrust surface was ca 9 km long along strike, but it was extended 2 km and 1 km towards the north and south respectively along strike. The thrust was also extended down-dip until 4000 m depth (Figure 20). The next section explains the reasons for extending the thrust surface.

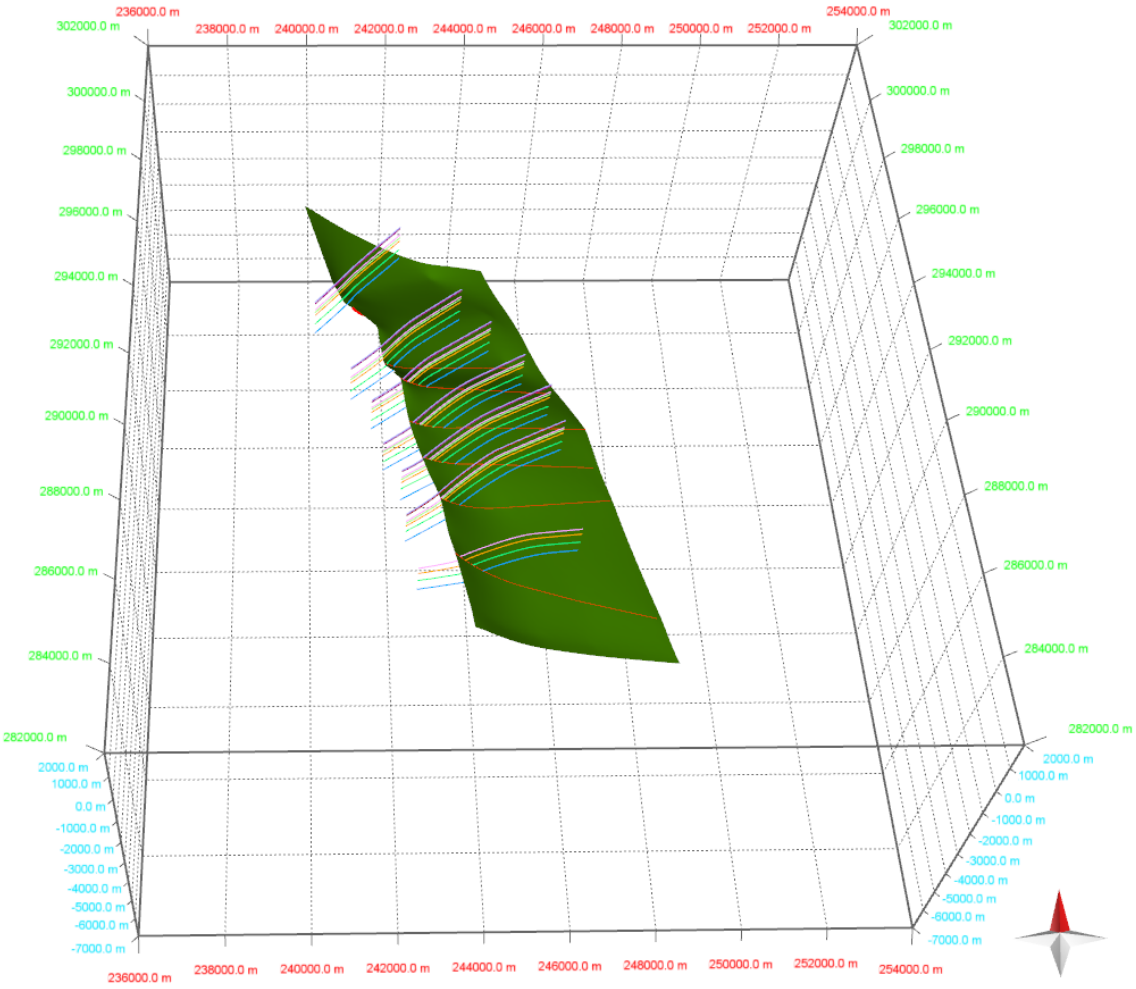

Figure 20. 3D perspective view in Move showing the horizons and fault traces after trishear inverse modelling. The green surface corresponds to the thrust plane generated from the interpolation of the fault segments (solid red lines) for each cross section.

4.4 Elastic Dislocation Modelling

Elastic dislocation (ED) is a geomechanical modelling technique used to calculate the distribution of subsurface strain due to dislocations (e.g. faults) in an isotropic elastic medium (Crouch *et al.*, 1983; Dee *et al.*, 2007; Thomas, 1993). In this study, I followed the methodology implemented by Dee et al. (2007). This methodology is the fundamental background of the FaultED (Fracture Prediction) module of TrapTester (Badleys, 2004). FaultED allows running the model forward and backwards to generate surfaces honouring the horizons interpreted in the seismic data. The module applies the ED formulation of Okada (Okada, 1985, 1992) to compute the displacement vector and strain tensor at points where the fault related strain is superimposed to the regional strain. To achieve this, the formulation uses the elastic constant of the medium and the fault geometry and fault displacements measured on the seismic data. The fault surface is discretized in smaller rectangular panels that contain fault parameters such as strike, dip, coordinates (x, y, and z) and slip (Figure 21). Arbitrary grids are generated to observe the displacement vectors and strain tensors in the elastic medium (Dee et al., 2007).

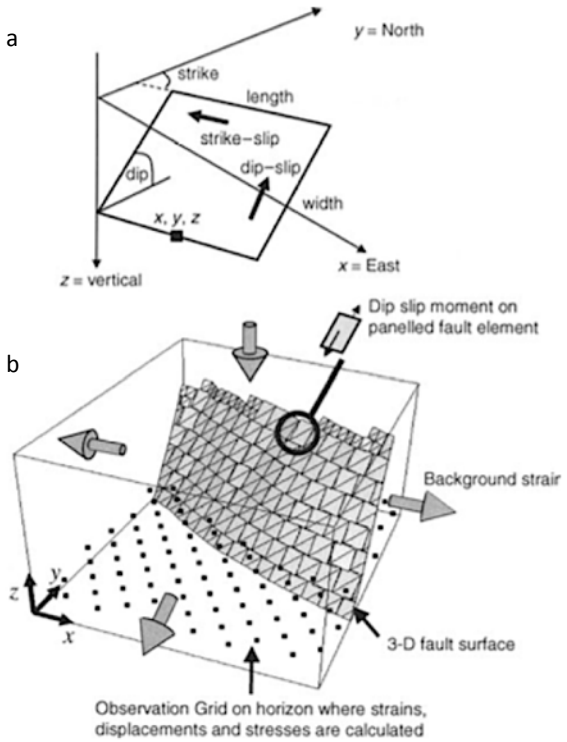

Figure 21 ***a.*** *Geometry of a single rectangular fault panel.* ***b*** *Discretization of the fault surface. After Dee et al. (2007).*

Since the well fracture data is restricted to the main reservoir, the ED modelling only was performed for the three lower horizons: the deepest top horizon of the Freemont Sandstone Formation underlying the main reservoir, the Tensleep Formation (main reservoir), and the overlying Crown Mountain Formation.

The 3D surfaces in depth from the previous step were imported into TrapTester software.
Then, the following workflow was used:

- Generation of structural model in TrapTester
- Generation of scenarios
- Observation grids

Framework modelling in TrapTester consists of a structural model with no stratigraphic infill (Badleys, 2004). In this study, this process started a step forward than the traditional procedure, since the 3D surfaces were already generated from the seismic interpretation, trishear modelling, and 3D surface generation. The next step consisted in the computation of the horizon-fault intersections or fault polygons, which represent the fault cutoff lines (Figure 22). Pairs of same-coloured solid lines correspond to the fault-horizons intersections for both hanging wall (upper dashed line) and footwall (lower solid line). The fault polygons' widths give an idea about the throw (vertical component of dip-slip displacement), which decreases towards the north. The orange uppermost fault polygon corresponds to the Crown Mountain Formation, the green- and blue fault polygons to the Tensleep and Freemont Sandstone Formations respectively. Note also an additional, lowermost purple polygon with the highest displacement. This polygon was drawn in response to inconsistencies observed in the initial modelling. The early model did not fit the amplitude of the anticline, due to the absence of a deeper fault polygon(s) with sufficient fault slip. After fault-polygons construction, fault attributes such as throw can be computed. (Figure 23) shows the thrust surface coloured by throw.

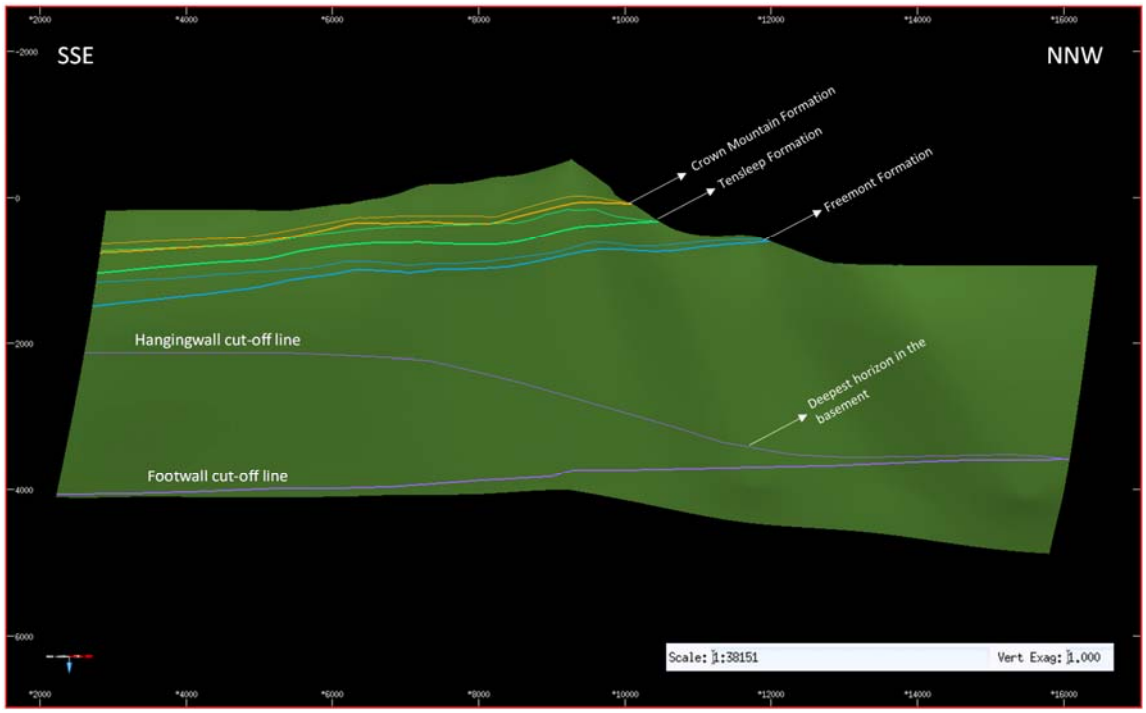

Figure 22 Strike view of the thrust showing the fault polygons representing the cutoff lines for both haging wall (dashed) and footwall (solid). Note how the throw decreases to the north.

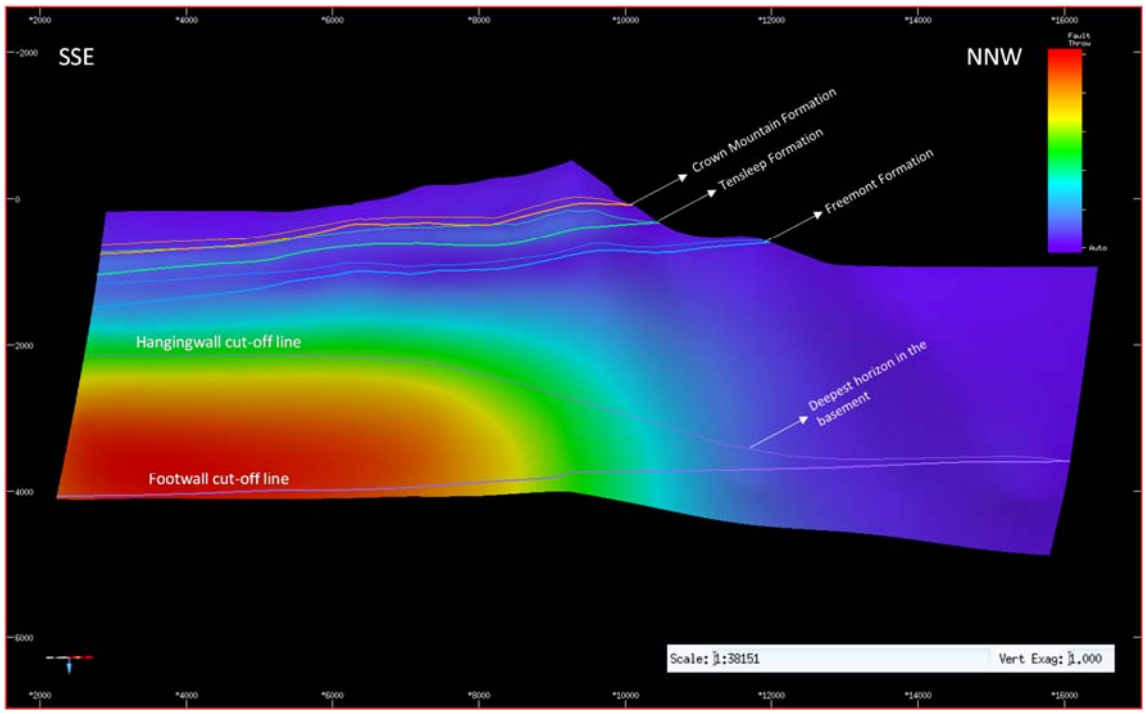

Figure 23 Strike view of the thrust colored proportional to the throw. Warmer colors represent higher throws. Note how the throw decreases upwards and towards the north.

Generation of scenarios is one fundamental step in the FaultED tool, since a single scenario encompasses the collection of parameters, which control the modelling of the dislocation (Badleys, 2004). In this step, fault panelling, background strain, and model parameters in general were set. Basic parameters and rock properties values were introduced in the general settings. Rock properties were taken from the Badleys, 2004 (Table 2), based on the lithology exhibited in the lowermost Palaeozoic units of Teapot, consisting mainly sandstones and carbonates. The values used for these units were a Poisson's ratio of 0.25, Young's Modulus of 15 GPa, total rock density of 2000 kg m^{-3}, cohesive strength of 20 MPa, and coefficient of internal friction of 0.5.

The model was constructed in an elastic half-space. The top of the elastic half-space is the free ground surface (zero datum), meaning that any object shallower than the datum is assumed to be in the air, therefore, it has not elastic response (Figure 24a). Teapot is an inactive structure that has undergone post-folding erosion since the cessation of faulting, therefore its current elevation of about 5500 ft (1700 m) above sea level is lower than its elevation at the time of faulting. I assumed that the highest elevation of the free ground surface at Teapot during the time of faulting and folding was about 6500 ft (2000 m) above sea level (Figure 24b). Therefore, a depth correction of -2000 m was entered in the model parameters.

Table 2Rock physic properties per lithology Badleys, 2004

Rock type	Young's Modulus E (GPa)	Poisson's ratio	Cohesive strength C (MPa)	coefficient of internal friction	Tensile strength T (MPa)
Westerly granite	56	0.11	37	1.4	21
Lac du Bonnet Granite	69	0.26	27	1.7	9.3
Solenhofen Limestone	53		63	0.6	
Berea Sandstone	19	0.38	28	0.5	1.2
Springwell Sandstone	12	0.36	13	0.6	
Tournemire Mudstone	23	0.32	16	0.6	
Granite	50-70	0.1-0.26	40-100	1.4	7-25
Basalt			30-85	0.6	10-30
Quartzite			50-100	0.9	10-30
Sandstone	10-20	0.21-0.38	5-40	0.5	4-25
Shale	5-70	0.2-0.4	1-25	0.6	2-10
Limestone	35-55	0.18-0.25	8-65	0.6	5-25
Marble	50-70	0.06-0.22	1000-2000	0.7	~7

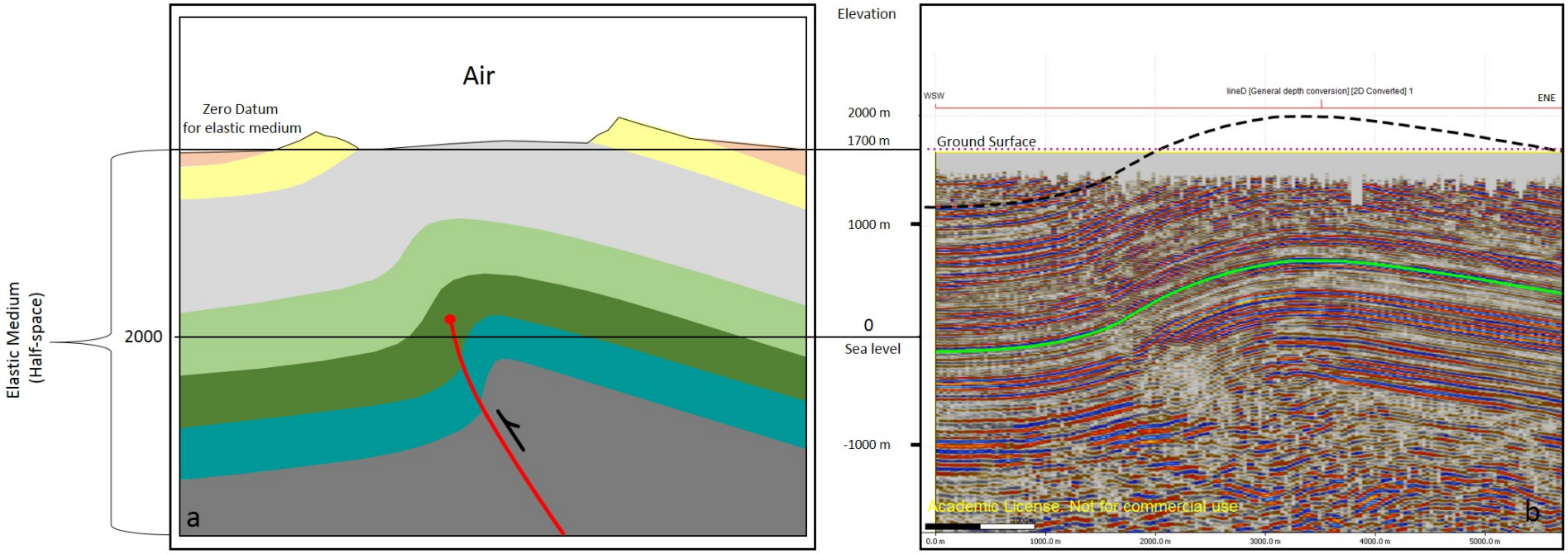

Figure 24. ***a.*** *Cartoon (not scaled) showing the half-space used in the FaultED module. Half-space corresponds to the elastic medium and its top (or zero datum) is the earth's surface.* ***b.*** *Reconstruction in Move of the pre-erosion geometry of Teapot using seismic line D. The dash line shows the elevation of the anticline at the time of faulting and folding. This reconstruction suggests that before the cessation of faulting, Teapot anticline reached an elevation of 2000 m above sea level.*

The fault panelling procedure was applied with the aim of discretizing the fault surface in an array of smaller rectangular dislocations following the fault geometry and its slip variation. The minimum and maximum panel sizes were set to 50 m and 100 m respectively for both the horizontal and vertical dimensions (Dee et al., 2007) (Figure 25). Two sub-horizontal and three vertical observation grids were generated to observe the deformed horizons after the calculations (Figure 26).

A background strain of 10% shortening was estimated by the ratio of the maximum heave observed in the horizon of the deepest stratigraphic unit (Freemont Formation, ca 400 m) and the width of the study area measured perpendicular to the fault strike (ca 4000 m). The orientation of the maximum horizontal strain is assumed to be perpendicular to the thrust

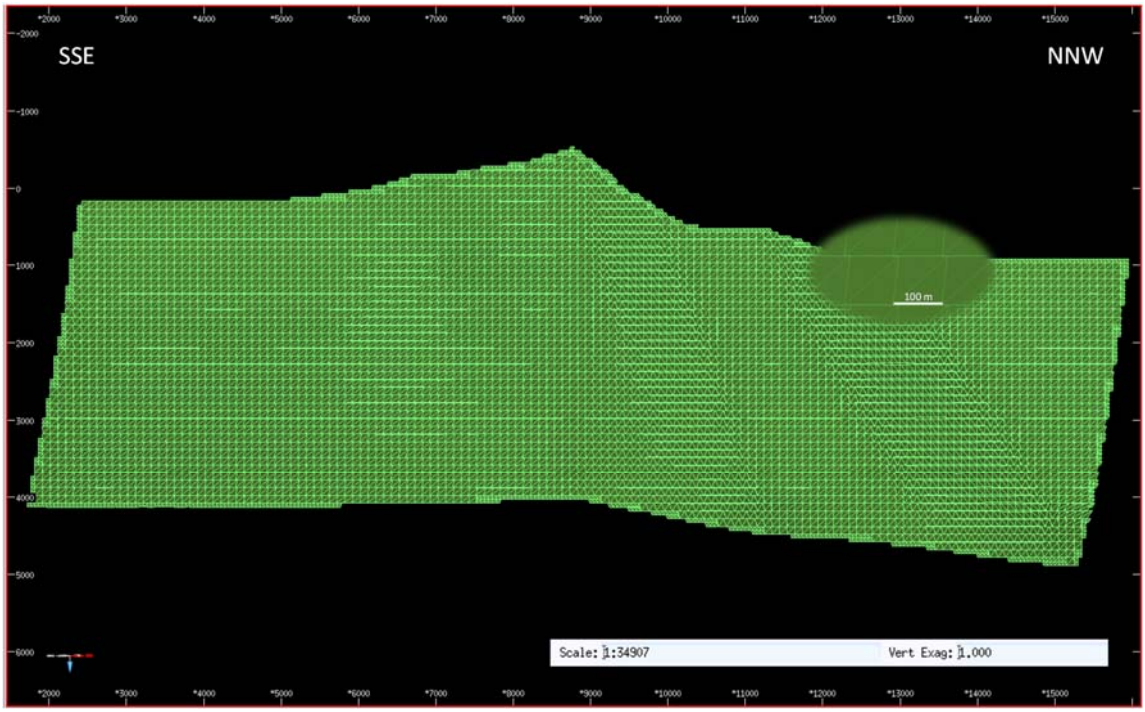

Figure 25 Thrust surface after applying the fault panelling procedure. Inset close-up shows the geometry and dimension of the panels

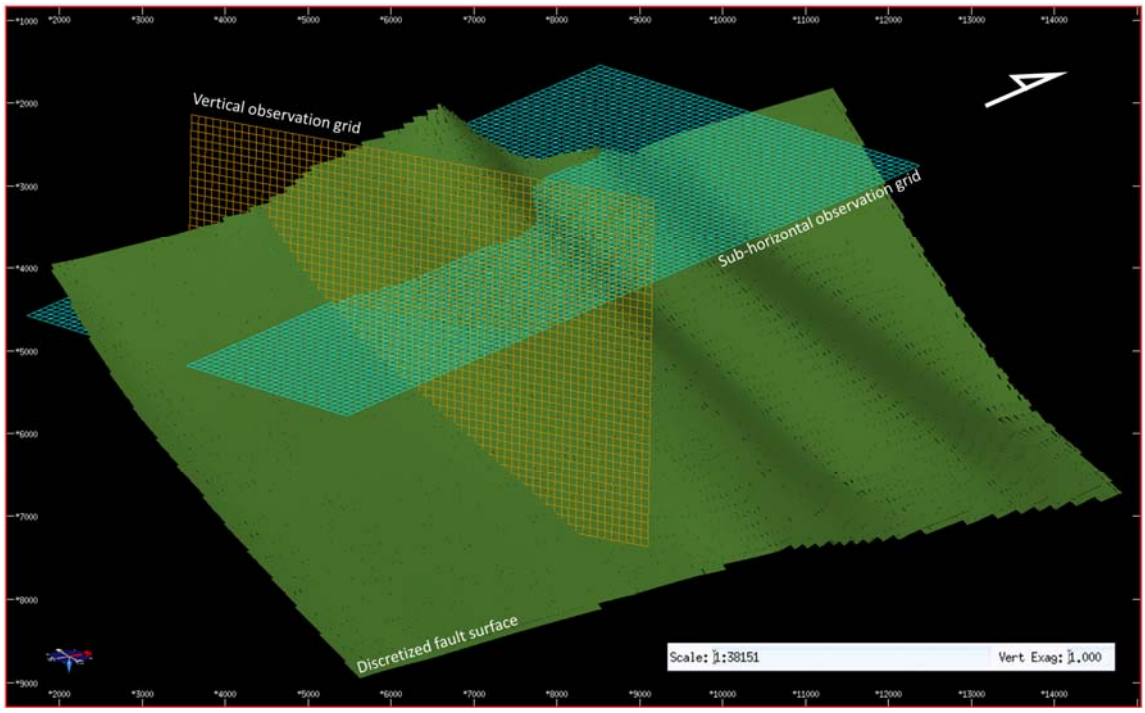

*Figure 26**Figure 25.** Vertical and horizontal observation grids generated to observe the deformed horizons. Note the discretization in small panels of the thrust surface.*

5 Results

The results of this thesis consist of three parts: 2D trishear modelling, construction of 3D geological model, and 3D elastic dislocation modelling. In addition, I discussed the implications of the trishear and elastic dislocation model for the prediction of fractures.

5.1 Trishear Model

2D trishear modelling was applied to eight cross-sections perpendicular to the fold axial trace to produce a kinematic reconstruction of the anticline and the underlying thrust on the sections (Figure 27e). Trishear models were compared against the exploration data (seismic and wells) in order to validate their predictions. Strain ellipses and lines of no finite elongation (LNFE) where also drawn in the models to be used as proxies for the orientation of fractures on the selected sections. The trishear best-fit models of the eight sections were the input for the construction of the 3D structural model of the anticline and the major thrust.

5.1.1 2D Modelling Reconstruction and Geometry Fits

As mentioned in the methodology chapter, an inversion modelling technique combining a listric thrust, trishear on the forelimb, and inclined shear on the backlimb (Cardozo & Branderburg, 2014) was applied. The technique uses a global optimization algorithm to determine the models that best fit the input horizons.

To better explain the results, I have divided the cross sections in three groups in accordance to the coverage of the seismic data. The first group of sections comprises sections S1, E, D2 and C1, where the seismic data only cover the backlimb (Figure 27). For practical purposes, the horizons are represented by numbers: 1. Freemont Formation, 2. Tensleep Formation, 3. Crown Montain Formation, 4. B1 reflector, 5. Dakota Formation, 6. II Wallcreek Member, and 7. R3 reflector. The second group of sections includes sections C and D, where the complete structure is in general well constrained by the seismic data, except in the steeply dipping forelimb areas where there is poor seismic imaging (Figure 28). The third group of sections includes sections B and B1 (Figure 29), where the entire fold geometry is well constrained by the seismic data.

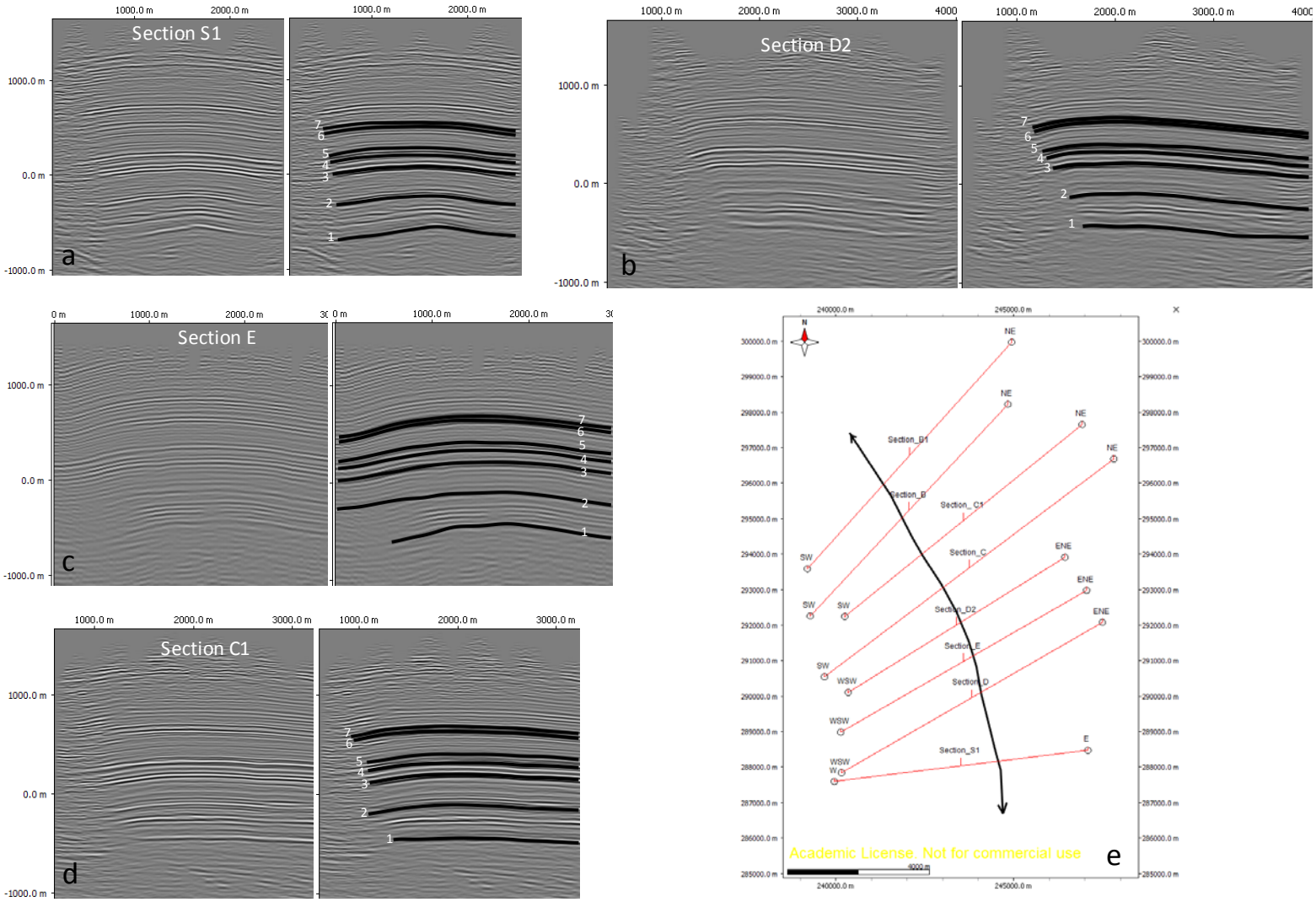

Figure 27 Cross sections of group 1. Seismic coverage is good in the backlimb. ***a****. Section S1,* ***b****. Section D2,* ***c.*** *Section E,* ***d.*** *Section C1, and* ***e.*** *Location of the section lines. On each section the seismic profile (left) and the interpreted horizons (right) are shown.*

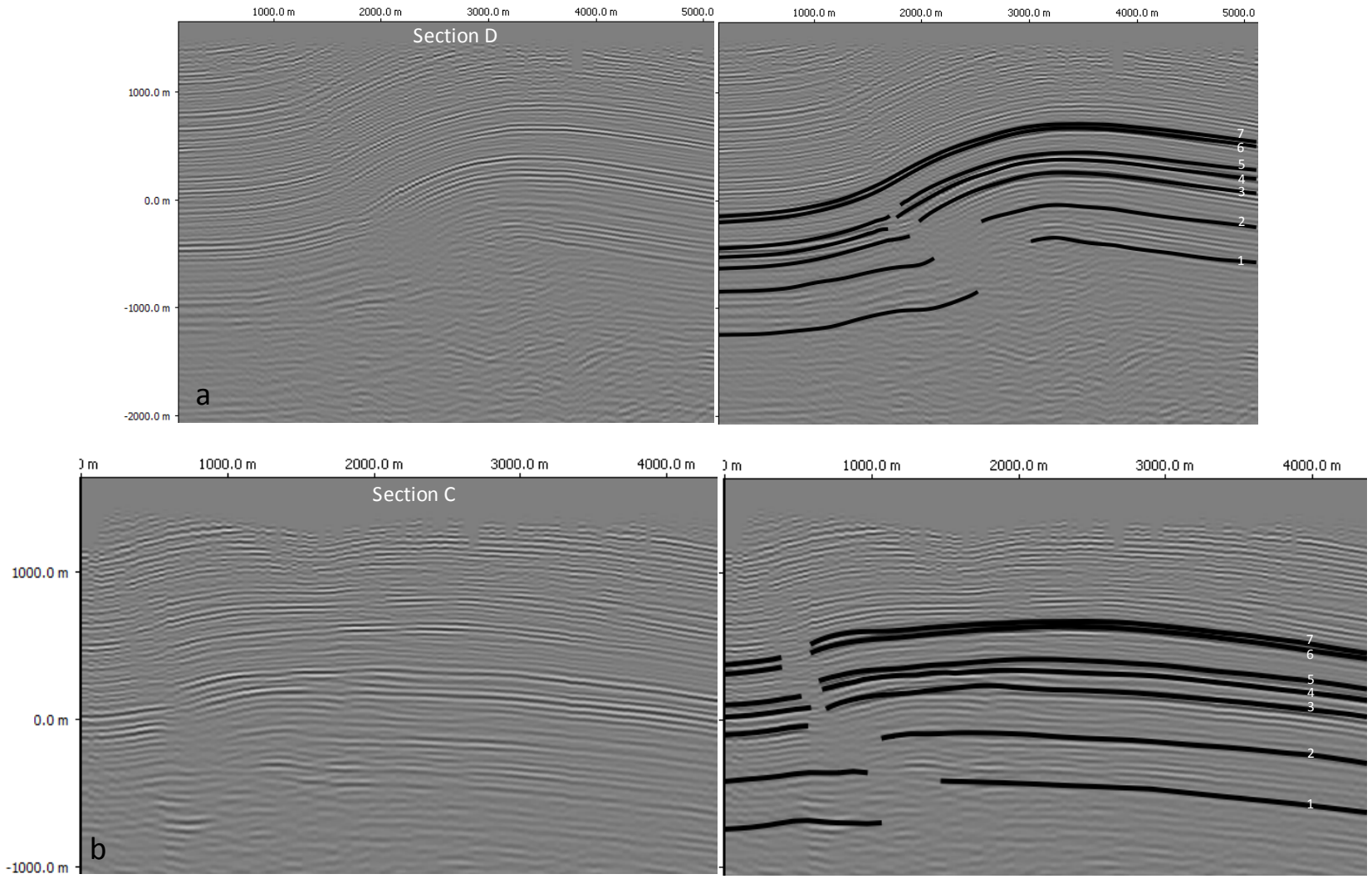

Figure 28 Cross sections of group 2. In general, the geometry of the structure is well imaged, except in the forelimb where beds are steeper ***a****. Section D and* ***b****. Section* ***C****. Each section includes the seismic profile (left) and the interpreted horizons (right). For location of the section lines please refer to Figure 26e.*

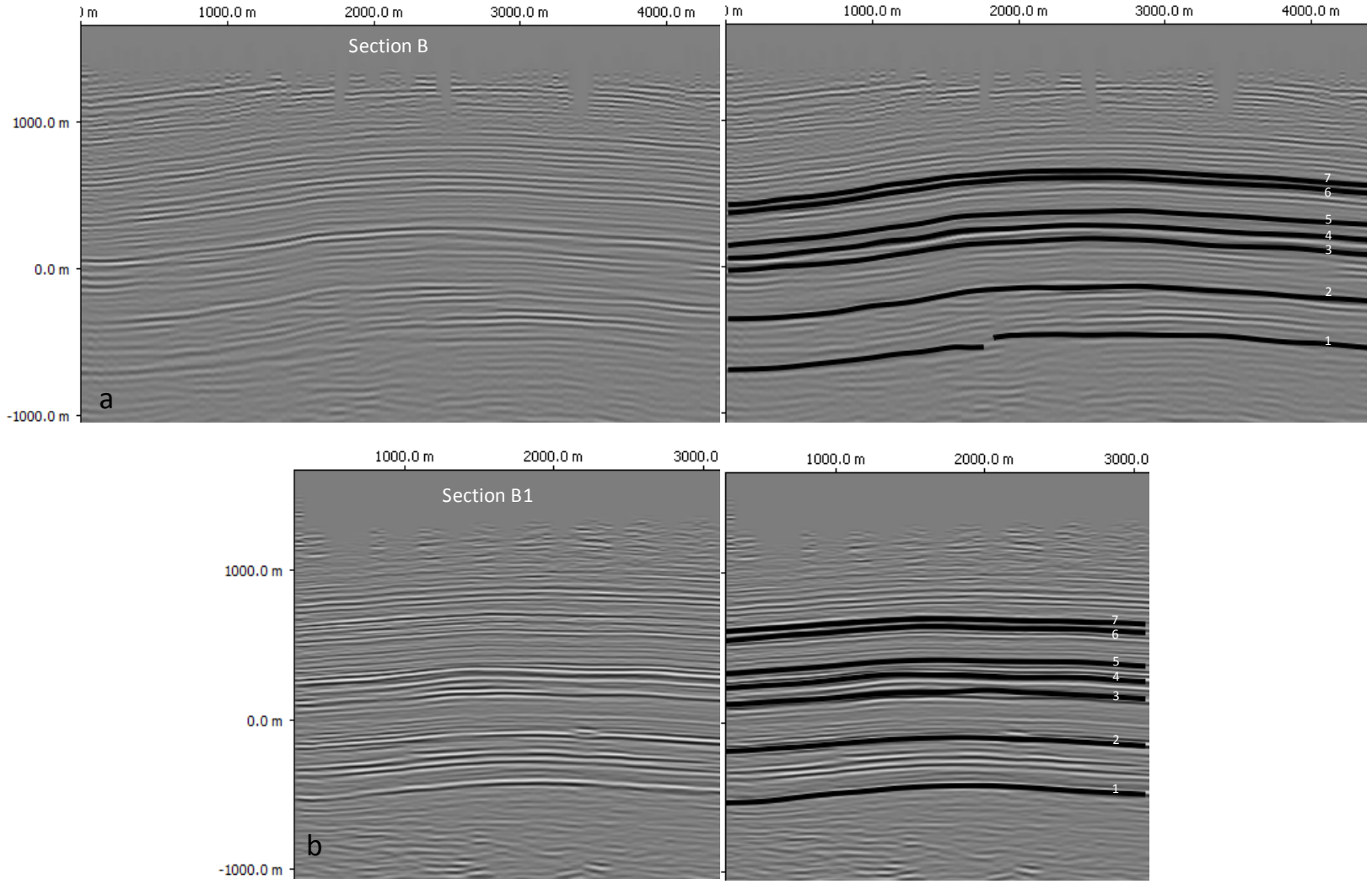

Figure 29 Cross sections of group 3. In general, the geometry of the structure is well constrained by seismic imaging. ***a****. Section B and* ***b.*** *Section B1. Each section includes the seismic profile (left) and the interpreted horizons (right). Section lines are shown in Figure 26e.*

Figures 30 to 37 show the kinematic modelling of these sections. The figures show the 100 models that best fit the anticline computed from the inversion of the four uppermost deformed beds 4-7, including the predicted fold geometry (black and grey lines are observed and predicted beds, respectively), and thrust geometry (red lines; Figs. 30-37 part a). The model with the lowest objective function (best-fit model), which was used to predict the geometry of the underlying beds 1-3 (Figs. 30-37, part b). The restored beds using the best-fit models (Figs. 29-36, part c), and histograms that show the distribution of the 100 best models for parameters such as P/S, trishear angle, slip distribution and shear angle in the backlimb (Figs. 30-37, part d). The grey dashed lines in the histograms indicate the parameter values of the best-fit model.

Group 1 (sections S1, E, D2 and C1)

This group involves the highest uncertainty in trishear modelling since the algorithm has to reconstruct the structure in areas with no data: forelimb, thrust trajectory and footwall. On the other hand, there is low uncertainty in the backlimb where the data coverage is good. One of the highest uncertainties is the thrust trajectory, which in the algorithm depends on the radius of curvature and the position of the thrust tip. Since the location of the thrust tip is unknown in these sections, its position had to be inferred from the interpretation of the other sections with better seismic coverage, for instance those in group 2.

The 100 best models for section S1 fit well the geometry of the backlimb (Figure 30a). The thrust tip was assumed to be at a similar location than in section D (Figure 34a), below horizon 6. However, some models show that beds 6 and 7 are offset by the thrust (Figure 30a). Ranges of P/S, trishear angle and shear angle show large spread, while the fault slip is the parameter that shows the lowest spread (Figure 30d). Although the best-fit model suggests good agreement between the observed and modelled geometry of the beds in the backlimb (1-7), there is high uncertainty in the forelimb, the thrust trajectory and the footwall (Figure 30b). No pre-kinematic folding and thinning is suggested by the planar geometry of the restored beds slightly dipping W (Figure 30 c).

The 100 best models for section E show good fit of the beds 4-7 in the backlimb and the crest, and a reasonable good fit on a small portion of the forelimb (Figure 31a). Despite these models having the highest f_{obj} in this group, they look fairly similar. This is confirmed by the less spread in P/S, trishear angle and slip parameters (Figure 31 d). The shear angle has more spread (Figure 31d) despite most of the data is in the backlimb. This could partially be explained by the gentle

termination of the observed beds 4-7 in the small-imaged-portion of the forelimb. The best-fit model fairly reproduces the deformed geometry of the lower beds 1-3 mainly in the backlimb and the anticline crest, while there is some misfit in the forelimb, particularly in bed 2 (Figure 31b). The geometry of the restored beds suggests sub-horizontal layers with subtle thinning (layer between horizons 2 and 3) towards the W, and no pre-kinematic folding (Figure 31c).

A more asymmetric anticlinal geometry is observed in the models of section D2 (Figure 32). Although the best 100 models resemble well the interpreted geometry of the backlimb, high uncertainty is present in the forelimb, footwall, and thrust trajectory (Figure 32a). The models not only show more spread shear angles (10°-19°) (Figure 32d), but also show that the shear angles are smaller than those observed in the less asymmetric geometry with more gentle backlimb, *e.g.* sections S1 (shear angle 29°-30°) and E (shear angle 24°-29°). The best-fit model reproduces well the geometry of beds 1-3 (Figure 32b), and the restored beds show planar and parallel geometry tilted towards the W (Figure 32 c).

The trishear models for section C1 show the best fit of the group. The models fit very well the observed backlimb geometry with low E dipping angle beds (Figure 33). This observation is confirmed by the relatively narrow range of shear angle values (27°-32°, Figure 33d). The spread of trishear angle and P/S is maybe associated to the high uncertainty in the thrust dip angle at the tip point (Figure 33a and d). Figure 33c shows sub-horizontal restored beds with no evidence of pre-kinematic folding, but some thinning of the uppermost layers towards the hanging wall. Notice that in section C1, the kinematic algorithm uses less than 45% of the circular arc defining the thrust (Figure 33a), while in sections S1, E and D2, the algorithm uses between 88 and 98% of this arc. Also, the radius of curvature of the thrust is larger in section C1 than in sections S1, E and D2. Essentially steep backlimb dips to the east require the thrust to horizontalize at a relatively shallow depth (Figs. 30-32, a), while shallow backlimb dips result in a steeper thrust that continues down section (Figure 33a). This results from the kinematics of the algorithm. Trishear deforms mainly the forelimb, while the backlimb geometry results from inclined shear on a listric thrust surface. This might not be true in reality, and we will see from the elastic dislocation modelling in a latter section, that the thrust must continue deep in the section in order to reproduce the anticline´s geometry. This is consistent with the observed geometry of thrusts below basement uplifts in the Laramide province (Allmendinger et al., 1983).

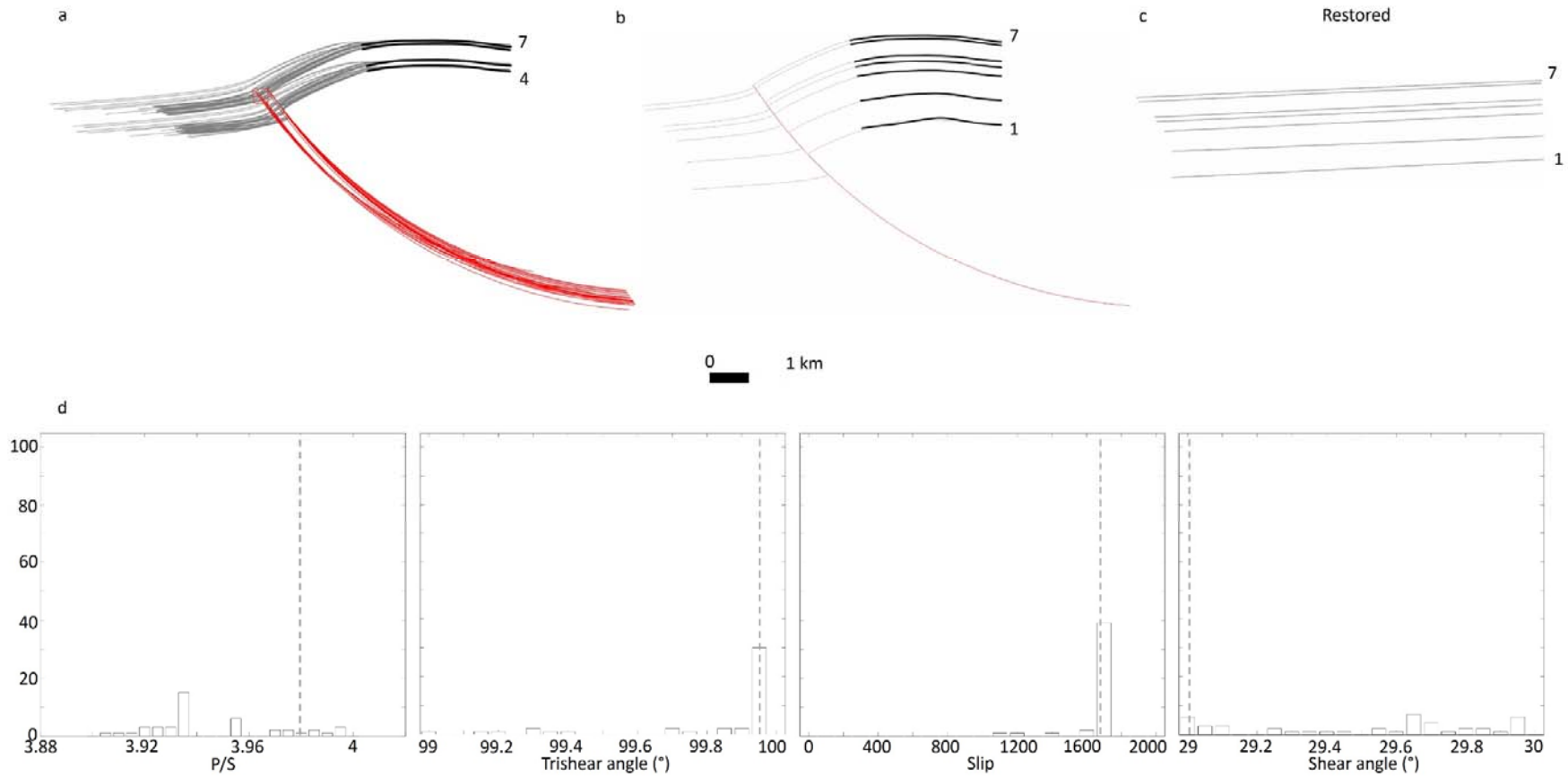

Figure 30 Trishear models for section S1, Group 1. ***a.*** *100 best trishear models for beds 4 to 7,* ***b.*** *Best-fit model applied to the complete sequence of beds 1-7. Modelled beds (gray lines) compared to the interpreted beds (black lines) and thrust (red line).* ***c.*** *The restored geometry of the beds using the best-fit model* ***d.*** *Histograms showing the distribution of the models in P/S, trishear angle, fault slip and shear angle. Vertical axis corresponds to the number of models. Gray dashed lines in histograms indicate the parameter values of the best-fit model.*

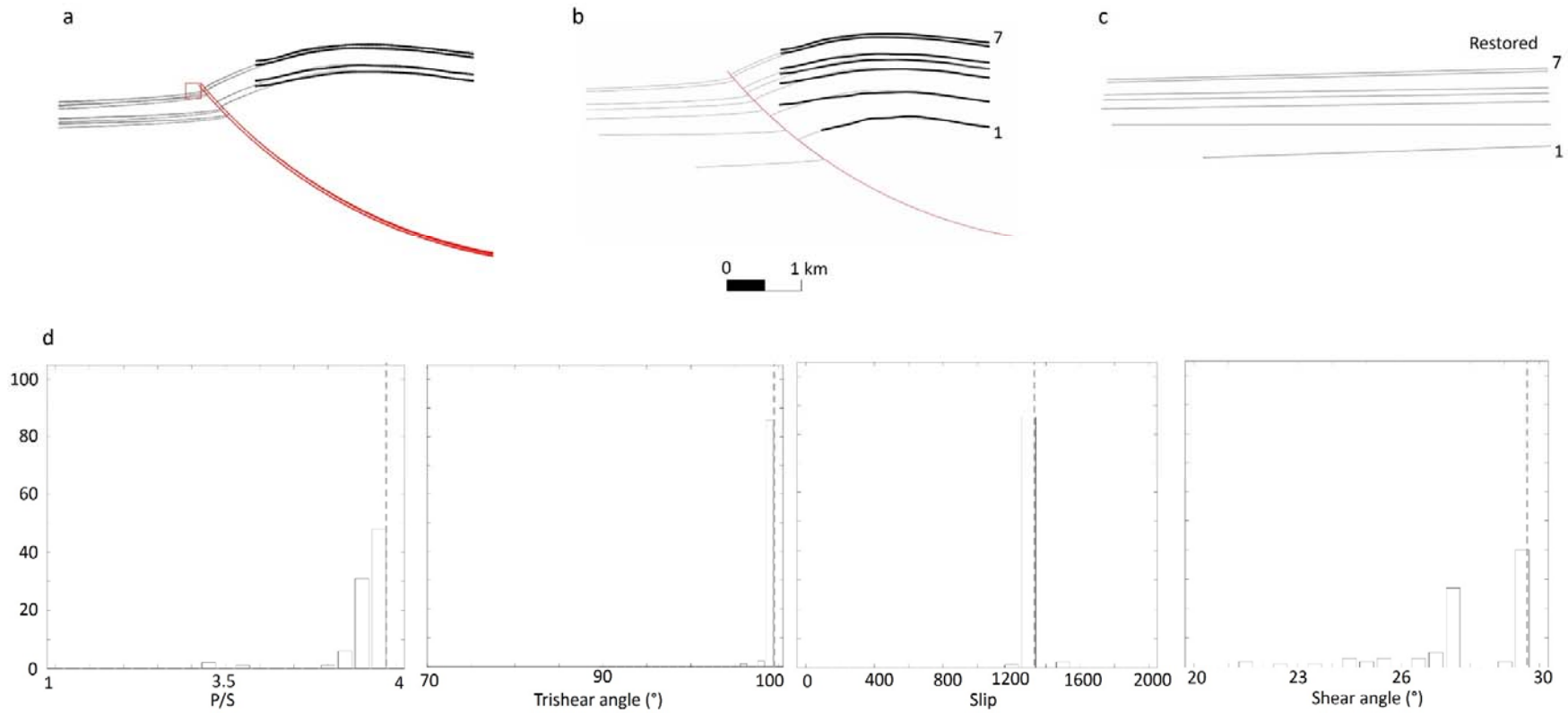

Figure 31 Trishear models for section E, Group 1. ***a.*** *100 best models for beds 4 to 7,* ***b.*** *Best-fit model applied to the complete sequence of beds 1-7. Modelled beds (gray lines) compared to the interpreted beds (black lines) and thrust (red line).* ***c****. The restored geometry of the beds using the best-fit model.* ***d.*** *Histograms showing the distribution of the models in P/S, trishear angle, fault slip and shear angle. Vertical axis scale corresponds to the number of models. Gray dashed lines in histograms indicate the parameter values of the best-fit model.*

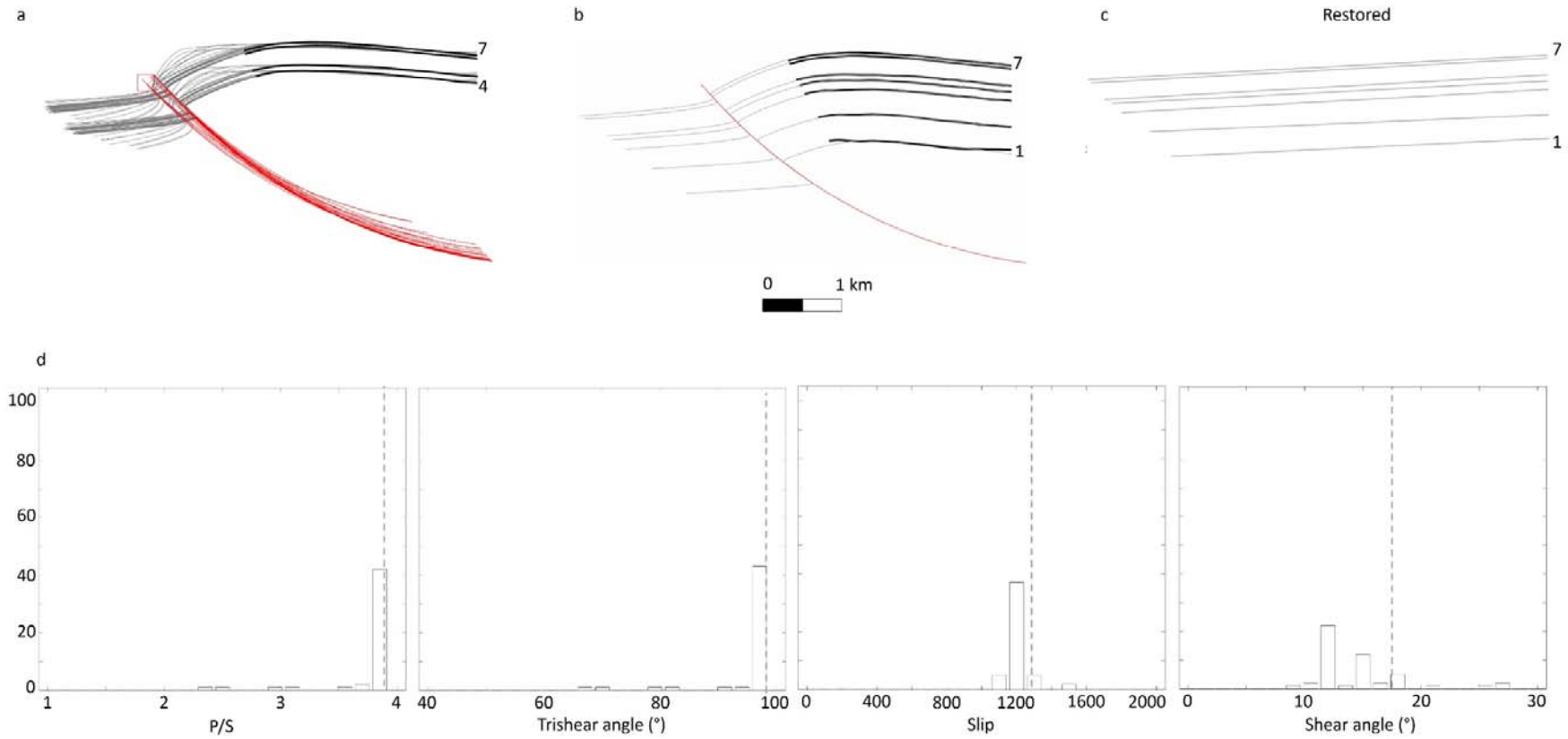

Figure 32 Trishear models for section D2, Group 1. ***a.*** *100 best models for beds 4 to 7,* ***b.*** *Best-fit model applied to the complete sequence of beds 1-7. Modelled beds (gray lines) compared to the interpreted beds (black lines) and thrust (red line).* ***c.*** *The restored geometry of the beds using the best-fit model.* ***d.*** *Histograms showing the distribution of the models in P/S, trishear angle, fault slip and shear angle. Vertical axis scale corresponds to the number of models. Gray dashed lines in histograms indicate the parameter values of the best-fit model.*

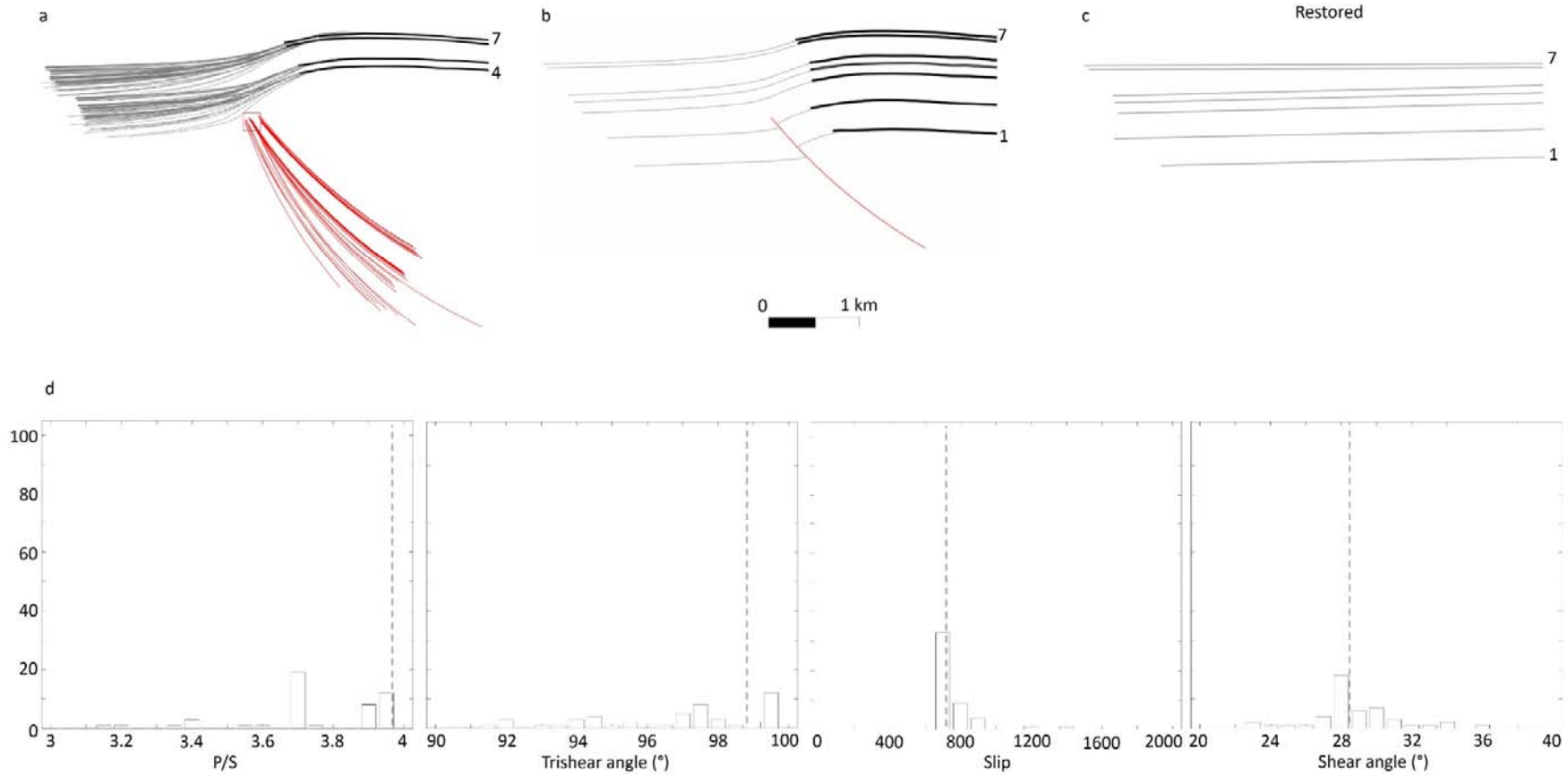

Figure 33 Trishear models for section C1, Group 1. ***a****. 100 best trishear models for beds 4 to 7,* ***b****. Best-fit model applied to the complete sequence of beds 1-7. Modelled beds (gray lines) compared to the interpreted beds (black lines) and thrust (red line).* ***c.*** *The restored geometry of the beds using the best-fit model.* ***d****. Histograms showing the distribution of the models in P/S, trishear angle, fault slip and shear angle. Vertical axis scale corresponds to the number of models. Gray dashed lines in histograms indicate the parameter values of the best-fit model.*

Group 2 (sections D and C)

Sections D and C are considered the sections that better capture the geometry of the Teapot anticline. The thrust position can be inferred in the wipeout area in the forelimb, although with large uncertainty because the horizons cutoffs in this area are not imaged (Figure 28). The beds imaged in these two seismic profiles suggest two different thrust geometries for the Teapot anticline. Section D (Figure 28a) is the key section of this study; it shows the geometry of a fault-propagation fold typical of this region. Based on the image, the thrust tip must be below bed 6. Since the thrust detachment is not clearly imaged, it will be reconstructed by the algorithm as that listric thrust geometry for which the backlimb beds are best fit. On the other hand, section C (Figure 28b) shows a more symmetric, less amplitude, and low curvature anticline with gentler beds in the forelimb and backlimb. This implies a more planar thrust.

The 100 best models for section D resemble very well the beds 4-7 (Figure 34a). The thrust does not offset bed 6 but the underlying beds 1-5. Figure 34d shows low spread in P/S, trishear angle and slip, but the shear angle shows larger spread (0-8°, almost vertical shear), partially explained by the low radius of curvature of the thrust. In the hanging wall, the best-fit model (Figure 34b) fits well the deformed geometry of the beds 2-7. Some misfit is observed in bed 1 in the hanging wall, and beds 1 and 2 in the synclinal footwall. The algorithm reproduces the thrust by propagating the slip along the entire circular arc. Thus, it suggests that the thrust horizontalizes at a relatively shallow depth (I tried larger radius of curvature, but the only way to reproduce the anticline's geometry in the backlimb was with a shallow detachment). The restored beds using the best-fit model show layers tilted and thinning (beds 2-3) towards the footwall with no pre-kinematic folding (Figure 34 c).

The 100 best models for section C have the highest misfit (highest fobj) of all sections, despite the good data constrain (Figure 28b). The interpretation suggests that all the beds are offset and their geometry is related to a planar-thrust structure. The 100 best models fairly fit the observed low curvature beds 4-7 (Figure 35a). The misfits in the backlimb are mainly localized where the interpreted beds have irregular geometries. The synclinal folding observed in the footwall is not well reproduced by the models. The algorithm only uses 37% of the circular arc to propagate about 750 m of slip along the thrust. The greatest spread is in the shear angle (27°-40°) (Figure 35d). The thrust of the best-fit model offsets all the beds1-7, but goes through bed

3 in the hanging wall (Figure 35b). No pre-kinematic thinning and folding is observed in the sub-horizontal restored beds (Figure 35c).

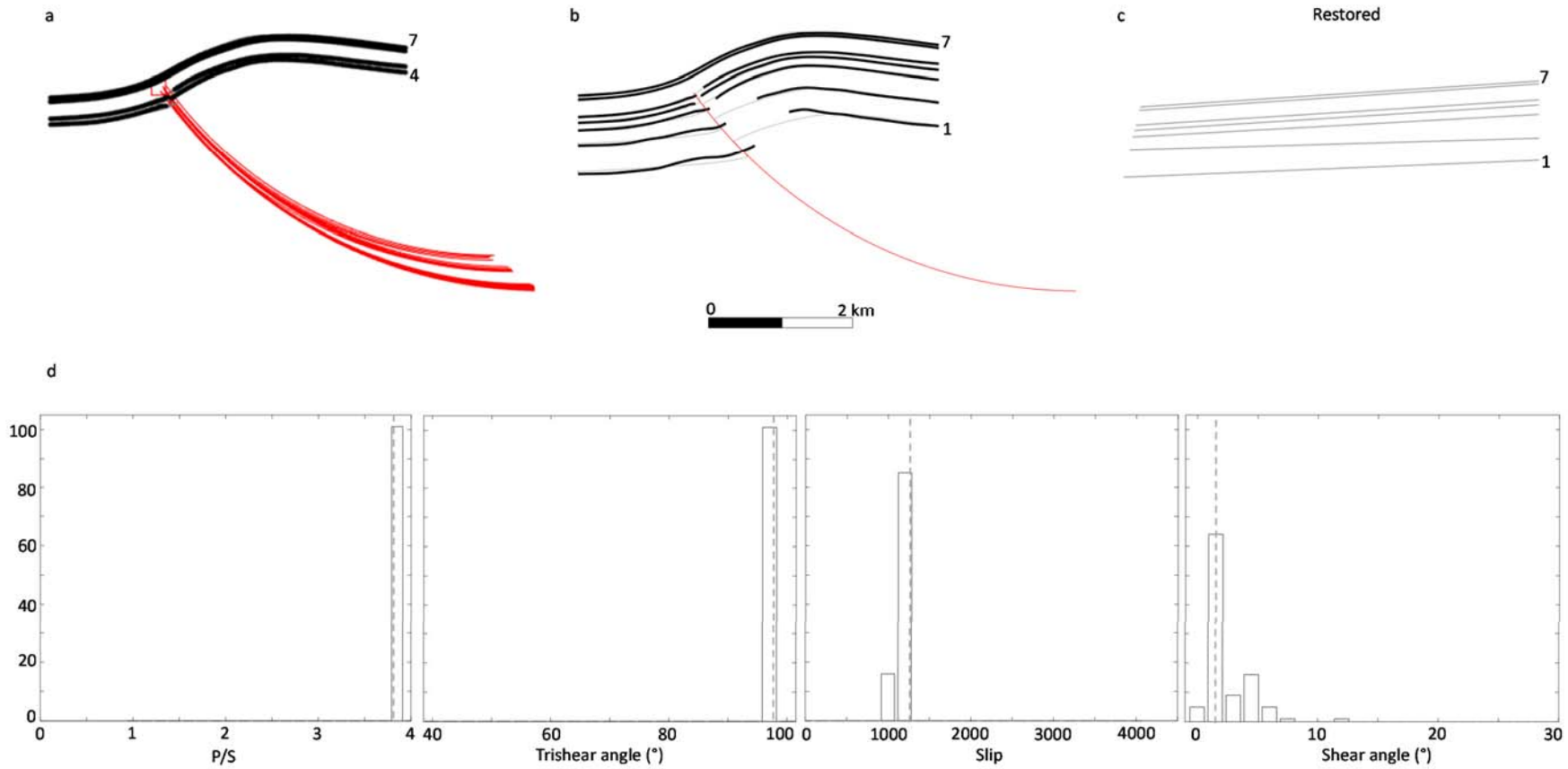

Figure 34 Trishear models for section D, Group 2. ***a****. 100 best trishear models for beds 4 to 7,* ***b****. Best-fit model applied to the complete sequence of beds 1-7. Modelled beds (gray lines) compared to the interpreted beds (black lines) and thrust (red line).* ***c.*** *The restored geometry of the beds using the best-fit model.* ***d****. Histograms showing the distribution of the models in P/S, trishear angle, fault slip and shear angle. Vertical axis scale corresponds to the number of models. Gray dashed lines in histograms indicate the parameter values of the best-fit model.*

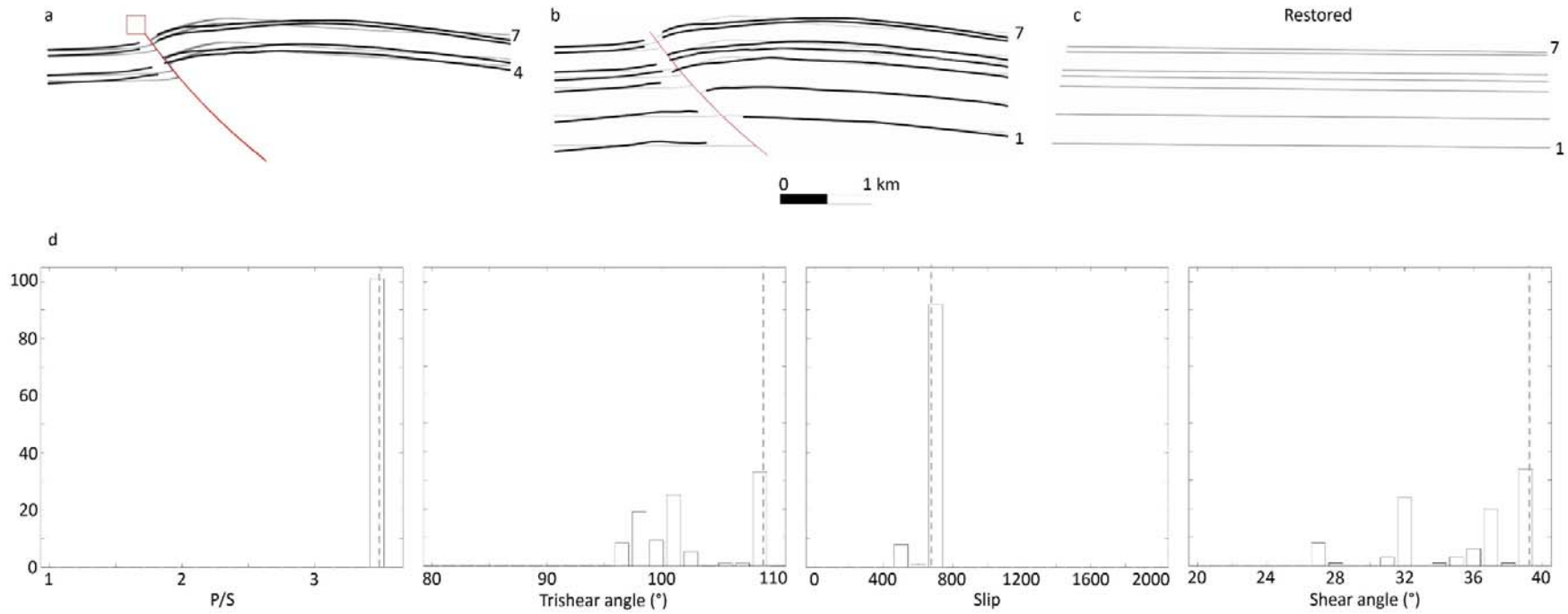

Figure 35 Trishear models for section C, Group 2. ***a****. 100 best trishear models for beds 4 to 7,* ***b.*** *Best-fit model applied to the complete sequence of beds 1-7. Modelled beds (gray lines) compared to the interpreted beds (black lines) and thrust (red line).* ***c.*** *The restored geometry of the beds using the best-fit model.* ***d****. Histograms showing the distribution of the models in P/S, trishear angle, fault slip and shear angle. Vertical axis scale corresponds to the number of models. Gray dashed lines in histograms indicate the parameter values of the best-fit model.*

Group 3 (B and B1)

Seismic profiles B and B1 provide the best coverage of the structure in the north. However, since the profiles are located at the northern fold termination, where the thrust dies out, the interpreted geometry does not provide much information about the thrust trajectory (Figure 29). The fold shows the lowest amplitude and curvature in section B1 (Figure 29b).

The 100 best models for sections B and B1 are quite similar since these sections are quite similar. The 100 best models fit well the deformed geometry of the beds in both cases (Figure 36a and 37a) despite showing some differences in the parameters values (Figs. 36d and 37d). The P/S is higher and has less spread in B (4) (Figure 36d). Both cases show large spread for trishear angle. However, B1 shows higher trishear angle values (70°-80°) than B (40°-50°). The opposite occurs with the shear angle, values are greater for B (23°-28°) than B1(14°-20°). These discrepancies could be explained by the propagation of the deformation upwards across the beds in relation to the proximity of thrust. The narrower wavelength observed in the fold crest at B, explains the smaller values of trishear angle relative to B1. This geometry maybe associated to the shallower thrust position. Restored horizontal beds suggest absence of folding and layer thinning at pre-kinematic stage (Figs. 36c and Figure 37c).

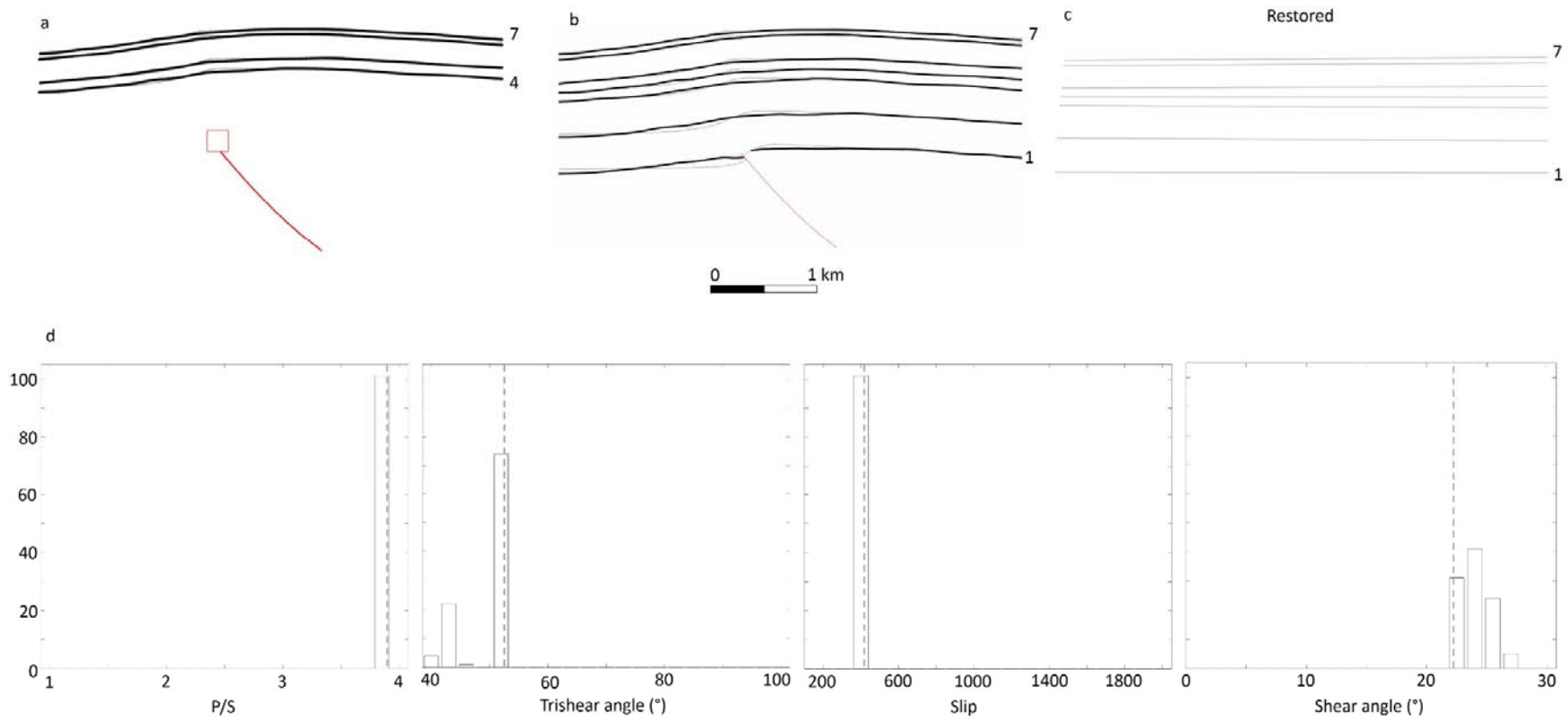

Figure 36 Trishear models for section B, Group 3. ***a.*** *100 best trishear models for beds 4 to 7,* ***b****. Best-fit model applied to the complete sequence of beds 1-7. Modelled beds (gray lines) compared to the interpreted beds (black lines) and thrust (red line).* ***c.*** *The restored geometry of the beds using the best-fit model.* ***d.*** *Histograms showing the distribution of the models in P/S, trishear angle, fault slip and shear angle. Vertical axis scale corresponds to the number of models. Gray dashed lines in histograms indicate the parameter values of the best-fit model.*

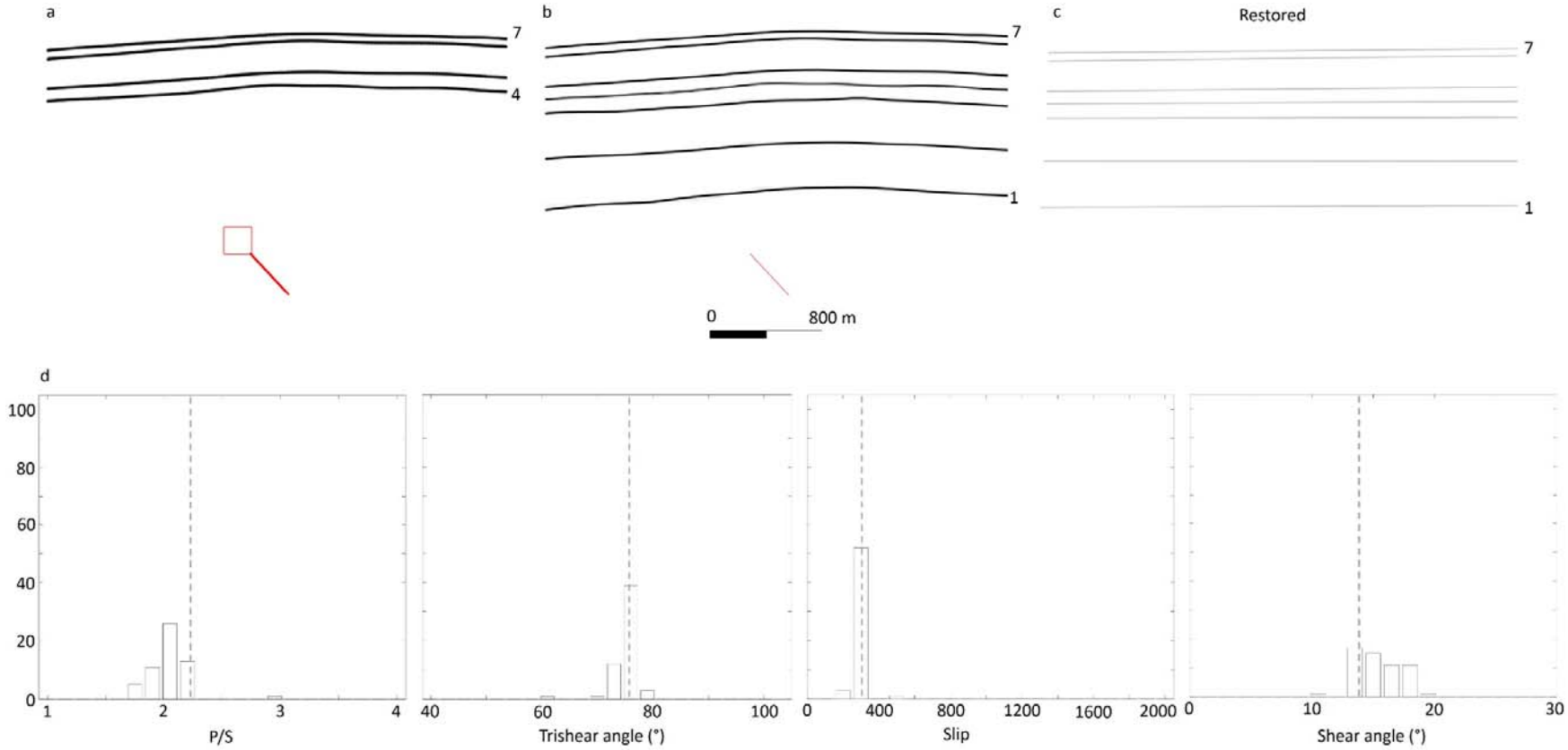

Figure 37 Trishear models for section B1, Group 3. ***a****. 100 best trishear models for beds 4 to 7,* ***b****. Best-fit model applied to the complete sequence of beds 1-7. Modelled beds (gray lines) compared to the interpreted beds (black lines) and thrust (red line).* ***c****. The restored geometry of the beds using the best-fit model.* ***d****. Histograms showing the distribution of the models in P/S, trishear angle, fault slip and shear angle. Vertical axis scale corresponds to the number of models. Gray dashed lines in histograms indicate the parameter values of the best-fit model.*

5.1.2 3D Model Reconstruction

Eight best-fit models were obtained from the 2D trishear modelling of the selected profiles. The beds and thrust traces on these cross sections were used to reconstruct the beds and thrust surfaces using the Kriging method in Move. This resulted in eight triangulated surfaces, seven horizons and the thrust plane.

The reconstructed horizons surfaces fit well the corresponding reflectors on both the 2D seismic lines and 3D seismic cube. However, the reconstructed thrust surface has a complex geometry (Figure 38a). 2D kinematic modelling suggest that the thrust reaches a maximum depth of about 2 km in the central part of the thrust surface along section D2 (Figure 38a). However, in the northern and southern regions, the 2D kinematic modelling delivers circular arc thrust traces with a larger radius of curvature that continue down beyond 2 km depth (sections S1 and B1, Figure 38a). Therefore, there is a dramatic (and perhaps unrealistic) dip angle variation of the thrust surface at ca 1.5 km depth in sections S, D2 and S1 (Figure 38a). When Kriging was performed, the thrust areas of low dip angle in the central region where extrapolated towards the northern and southern areas with higher dips. The surface that emerged was a complex thrust plane with a listric geometry in the central region and a more planar geometry towards the northern and southern fold terminations (Figure 38a). This 3D thrust geometry is rather unreasonable.

To test the geological validity of the modelled thrust surface in (Figure 38a), a preliminary exercise was performed by applying the elastic dislocation (ED) technique using this thrust surface. The geomechanic approach showed that a feasible mechanical model of the anticline cannot be obtained with such thrust geometry (refer to the next section for more details). These initial observations in the geomechanical model helped highlighting inconsistencies in the interpretation and modelling of the thrust geometry, particularly since the thrust is not clearly imaged.

To obtain better results in the geomechanical model, the thrust was extended 2 km down dip in a more planar fashion. This more planar, and more reasonable thrust surface is displayed in Figure 38b. The thrust surface has a steep upward termination (ca 50-55° dip) as the 2D trishear models suggest, and goes down with shallower dip angles of ca 35-40° (Figure 39).

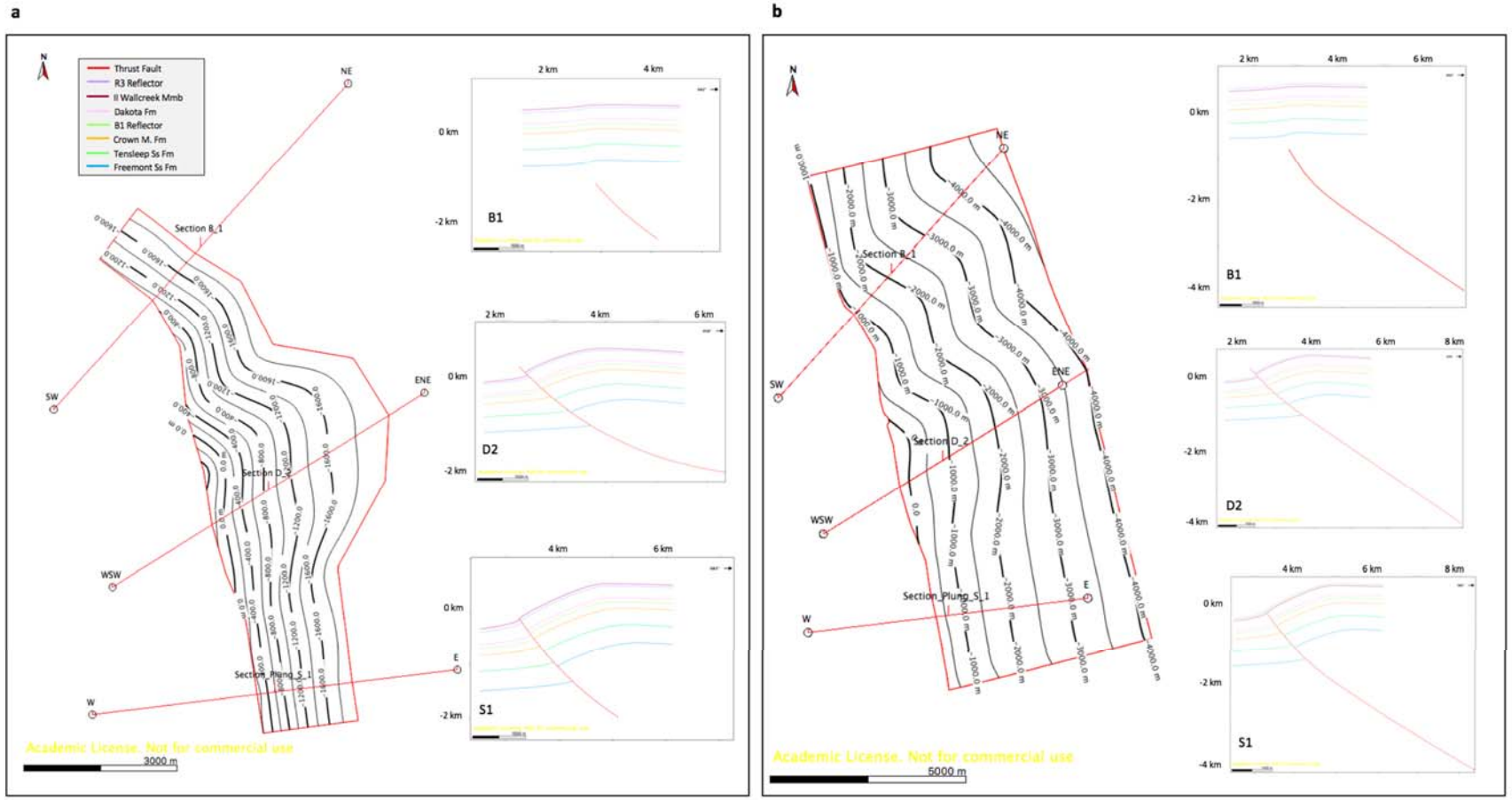

Figure 38 ***a.*** *Left: Initially reconstructed geometry of the thrust in the 3D structural model. Contours are depth in meters. Right: Cross-sections through the southern, central and northern part of the thrust surface. Bed colors correspond to those of the legend (left upper corner)* ***b.*** *Left: Improved, more planar geometry of the thrust in the 3D structural model. Contours are depth in meters. Right: Cross-sections through the southern, central and northern part of the thrust. Bed colors correspond to those of the legend in a. Notice that in the improved thrust interpretation, the thrust does not detach at a shallow level.*

Basically, I disregard the shallow detachment predictions of the kinematic models in the central part (profiles D2, E and D), yet use the geometries predicted by the kinematic algorithm both in the backlimb and forelimb. I believe this is a reasonable approach, because the forelimb which is partially or not imaged on seismic is modelled with trishear, and the backlimb which is well imaged on seismic is modelled by inclined shear on a shallow listric thrust surface that yet can be unrealistic. The kinematically predicted shallow thrust surface is highly uncertain, but the backlimb geometry is not. This means that, strictly speaking, in the central part, the kinematic model is used to reconstruct the forelimb, not the backlimb. Kinematic predictions on the backlimb in this central region might not be valid, considering the kinematic models deliver a very shallow thrust in this area. Extending the thrust down dip also conforms with the observed geometry of thrust faults below basement uplifts in the Laramide province, where the thrusts extend to mid-crustal depths (10-15 km, Allmendinger et al. 1983). On elastic dislocation models, movement on this deep, planar thrust causes a long-wavelength effect on the surface uplift and backlimb rotation (King & Brewer, 1983), which cannot be explained by the kinematic model.

(Figure 40) shows the 3D geological model of the Teapot anticline, with the reconstructed horizons and the thrust surface. Figures 41 to 48 show cross-sections of the 3D structural model superimposed on the seismic profiles. A structural map of the reservoir level, the top of the Tensleep Formation, is displayed on the right side of the figures. Note than on all seismic profiles, the modelled horizons fit well their corresponding seismic reflectors in areas with good seismic image, both in the backlimb and forelimb. Also, the modelled horizons predict reasonable forelimb geometries in forelimb areas with poor seismic image (seismic wipeout zones). The upper part of the modelled thrust surface also conforms to the approximate location of the thrust in forelimb areas (Figure 42). These are all proof of the validity of the 3D model, although of course there is uncertainty in both the forelimb and the underlying thrust geometries.

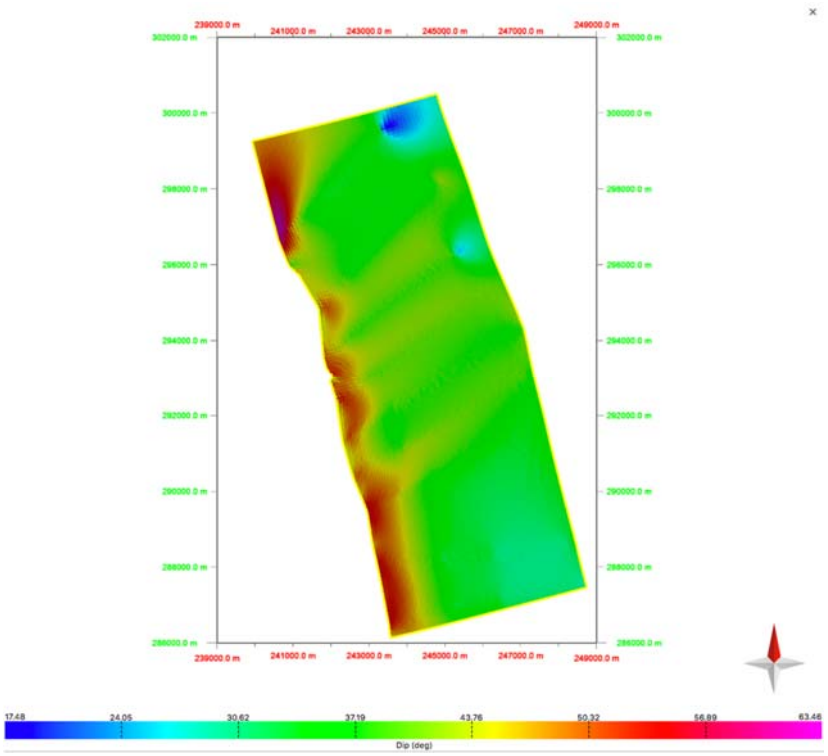

Figure 39 Map view of the improved thrust geometry colored by dip angle.

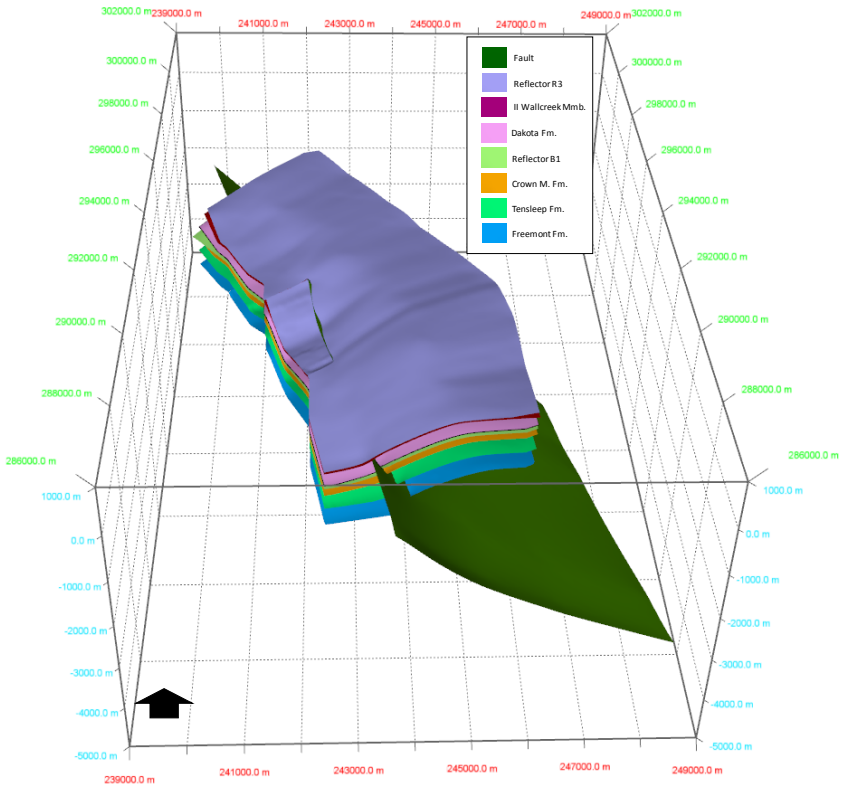

Figure 40 Perspective view towards the north of the 3D structural model consisting of seven horizons and the thrust surface.

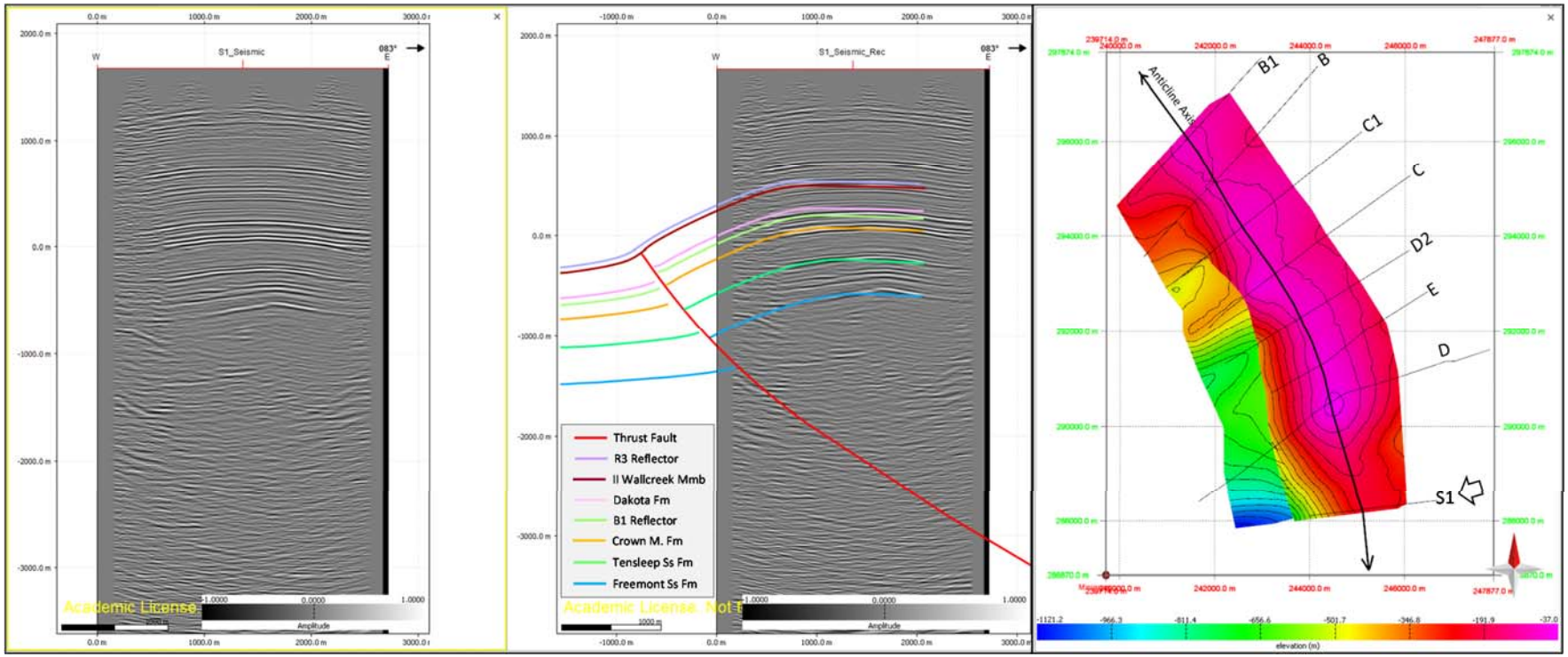

Figure 41 Left: Seismic profile at section S1. Middle: modelled beds and thrust (intersection of 3D model with the profile) is superimposed on the seismic profile. Right: location of section lines over structural map of the reservoir level, top of the Tensleep Formation.

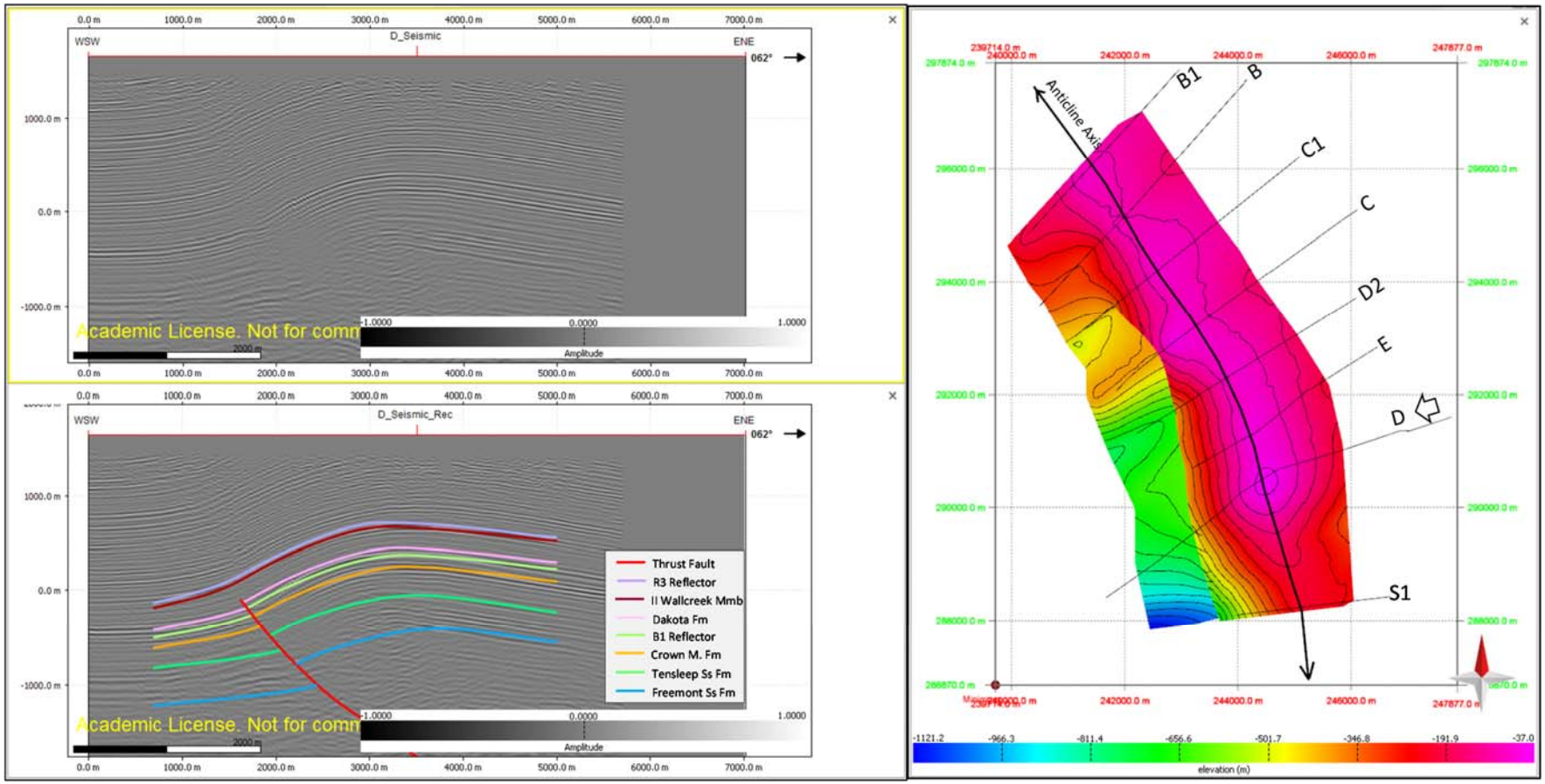

Figure 42 Top left: Seismic profile at section D. Bottom left: modelled beds and thrust (intersection of 3D model with the profile) is superimposed on the seismic profile. Right: location of section lines over structural map of the reservoir level, top of the Tensleep Formation.

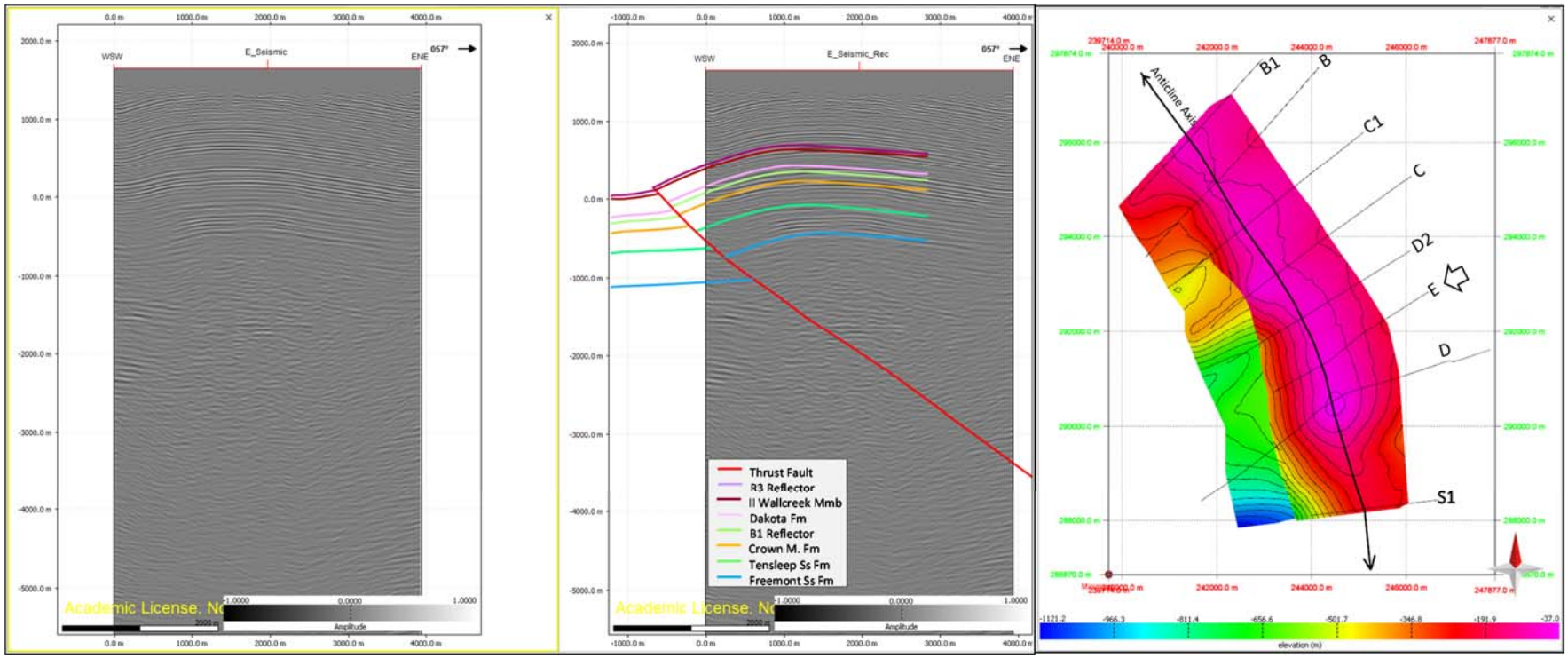

Figure 43. Left: Seismic profile at section E. Middle: modelled beds and thrust (intersection of 3D model with the profile) is superimposed on the seismic profile. Right: location of section lines over structural map of the reservoir level, top of the Tensleep Formation.

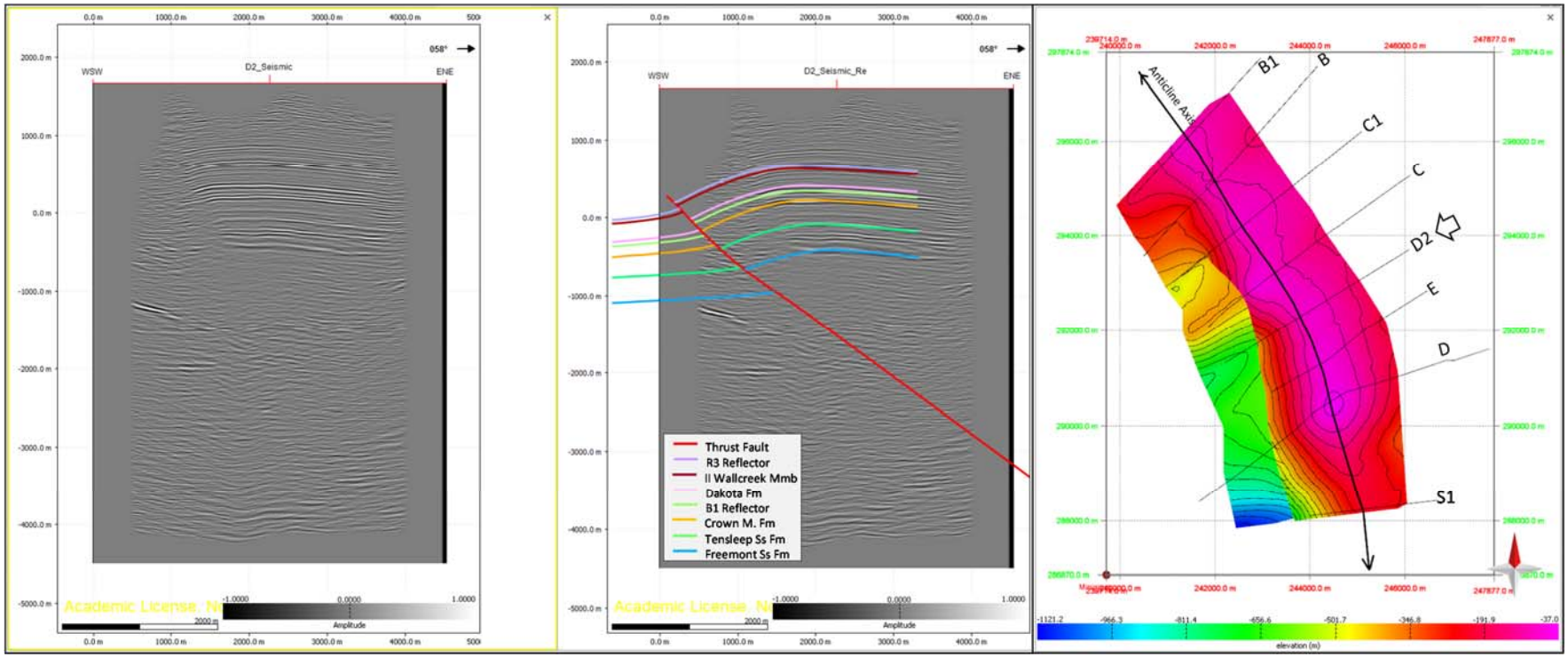

Figure 44. Left: Seismic profile at section D2. Middle: modelled beds and thrust (intersection of 3D model with the profile) is superimposed on the seismic profile. Right: location of section lines over structural map of the reservoir level, top of the Tensleep Formation.

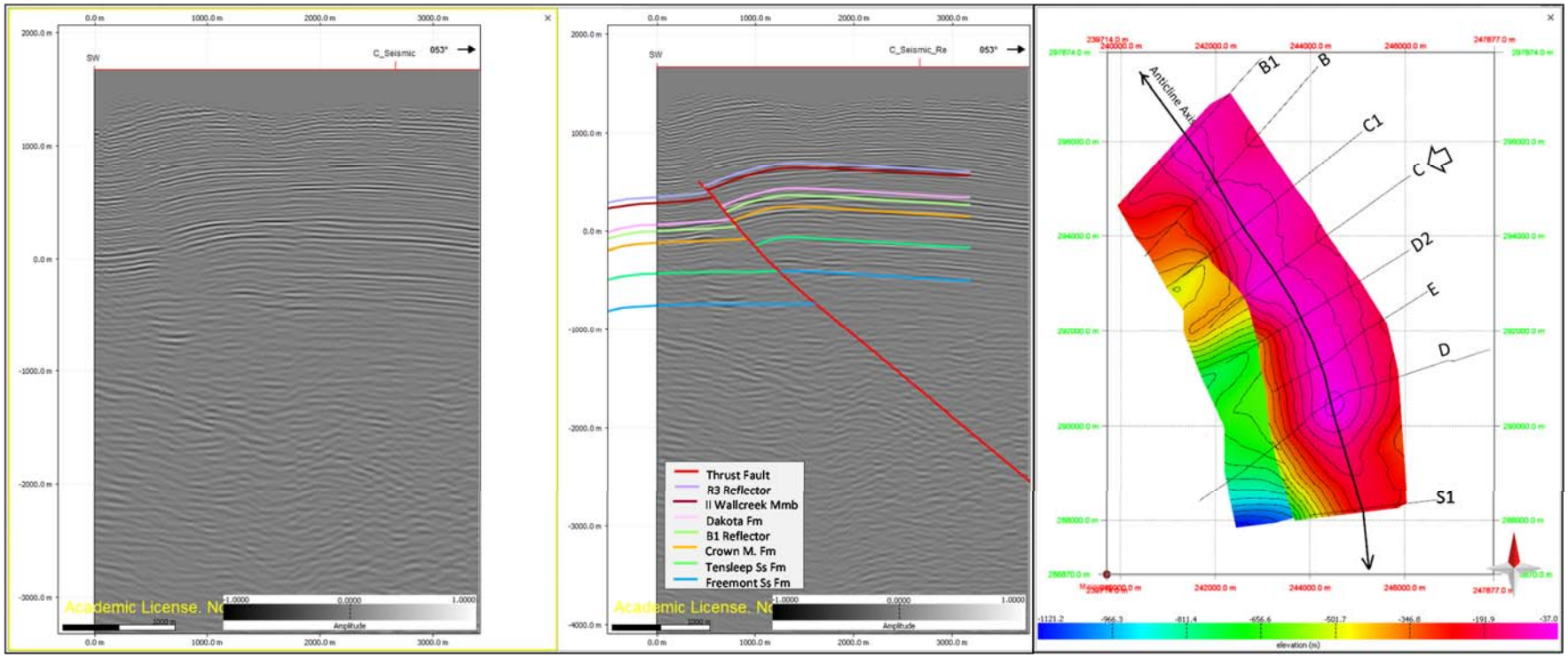

Figure 45 Left: Seismic profile at section C. Middle: modelled beds and thrust (intersection of 3D model with the profile) is superimposed on the seismic profile. Right: location of section lines over structural map of the reservoir level, top of the Tensleep Formation.

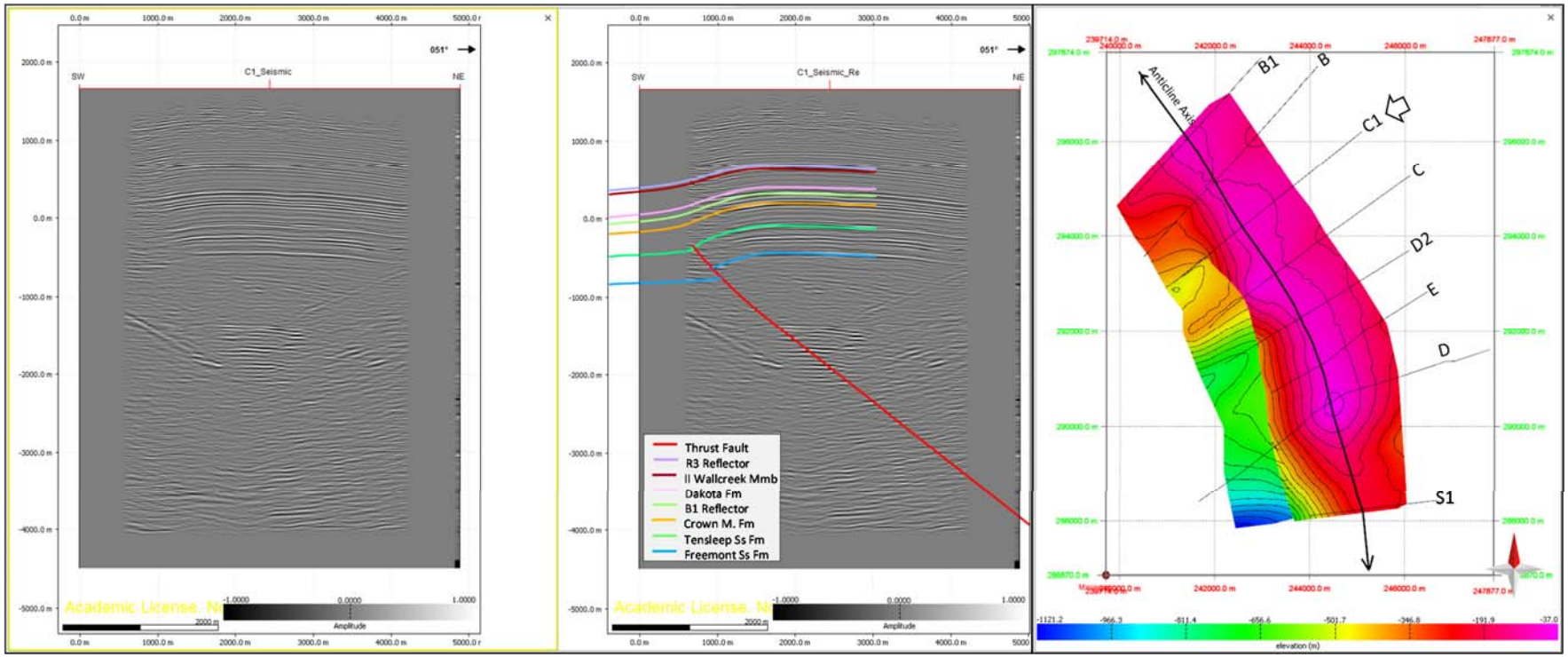

Figure 46 Left: Seismic profile at section C1. Middle: modelled beds and thrust (intersection of 3D model with the profile) is superimposed on the seismic profile. Right: location of section lines over structural map of the reservoir level, top of the Tensleep Formation.

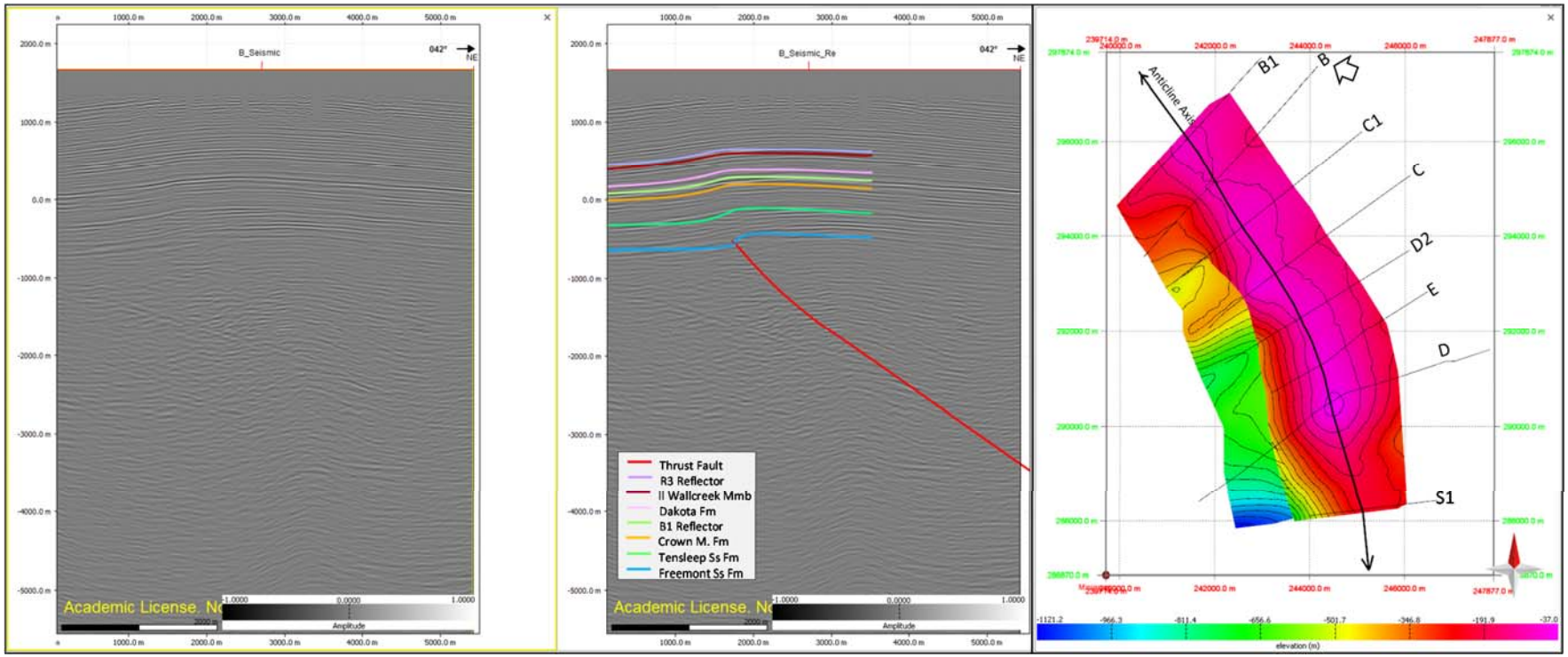

Figure 47 Left: Seismic profile at section B. Middle: modelled beds and thrust (intersection of 3D model with the profile) is superimposed on the seismic profile. Right: location of section lines over structural map of the reservoir level, top of the Tensleep Formation.

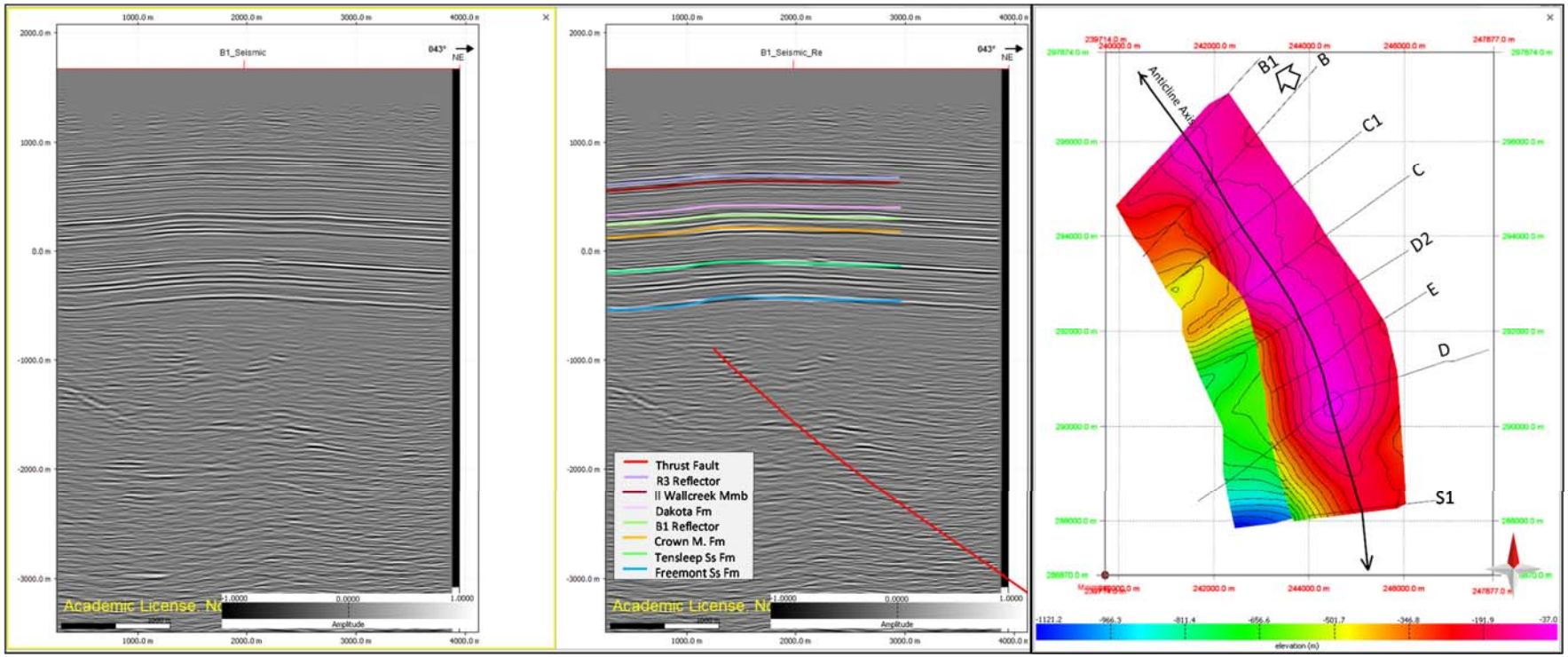

Figure 48 Left: Seismic profile at section B1. Middle: modelled beds and thrust (intersection of 3D model with the profile) is superimposed on the seismic profile. Right: location of section lines over structural map of the reservoir level, top of the Tensleep Formation.

5.2 Elastic Dislocation Model

The 3D structural model from the previous sections was loaded into TrapTester to perform elastic dislocation modelling (ED). This technique helped validating the predictions of the geometries provided by the kinematic modelling and provided proxies for fracture generation. Again, there is some circularity in this process because reconstructions from kinematic modelling are imported to the geomechanical model. Ideally, for comparison between the kinematic and geomechanical models one would need a complete dataset of the anticline and thrust that is used independently in the kinematic and geomechanical model.

The results described in the following section were obtained by applying manual (trial and error) ED modelling. Automated inverse ED methods (e.g. Healy et al., 2004) were not available. In ED modelling, the horizons and the thrust are inside an isotropic elastic medium. Displacement vectors and strain tensors are produced by the perturbation caused by the dislocation (major thrust) in the isotropic elastic medium (Dee et al., 2007). It is important to notice that in ED both the horizons and the thrust undergo deformation. This is opposite to kinematic models, where the thrust trajectory is fixed.

The horizons and the thrust were restored to their pre-deformation position by applying backward ED, and the restored beds were forward modelled (forward ED) to compare the modelled and the input horizons. Pre-model restoration step consisting of move the surfaces to the present day post-deformation state did not work properly. This is the reason why there is an offset of about 300 m between the modelled and interpreted fault. It is important to notice that the presented model is rather preliminary; with more time, I would have been able to obtain a better model.

The distribution of subsurface strain was calculated at the Tensleep reservoir level. Displacement, strain and stress were observed in one vertical and three sub-horizontal grids: one for the Tensleep reservoir and two for the underlying and overlying Freemont and Crown Mountain Formations, respectively (Figure 49). The results are divided in two: i. Comparison of the ED deformed surfaces with the input surfaces, and ii. Use of the geomechanical model for fracture prediction.

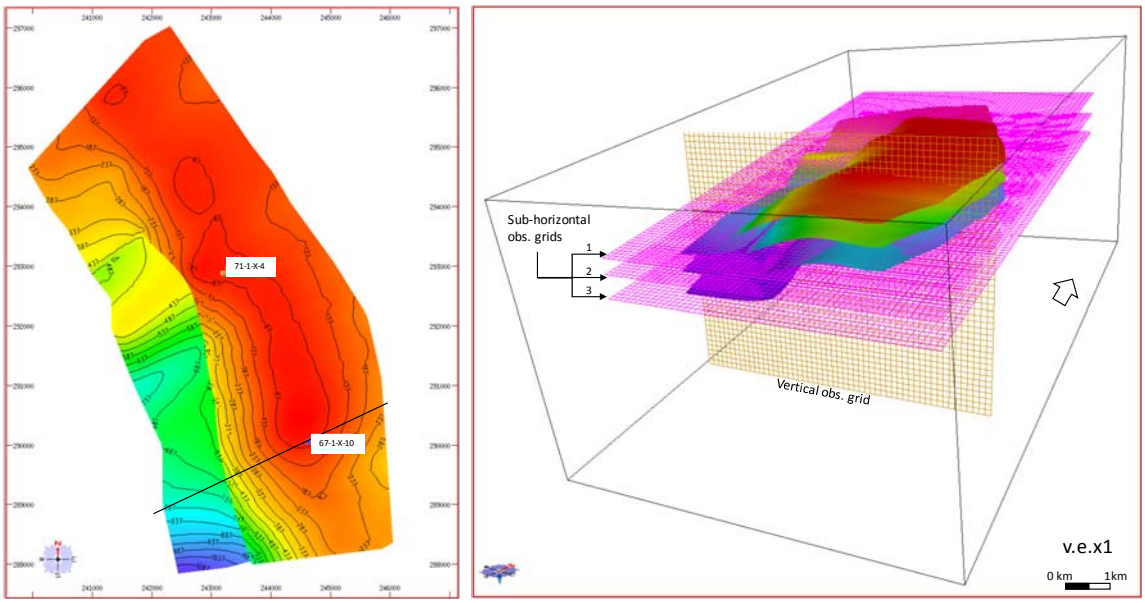

Figure 49 Left: Structural map of the Tensleep Formation top loaded into TrapTester. Note the location of the wells with fracture data and the location of the vertical grid. Right: Perspective view showing the observations grids used for visualizing the ED model. Vertical grid perpendicular to fault strike (orange), sub-horizontal grids following the regional dip of the beds (magenta).

5.2.1 Deformed Surfaces

As was mentioned in the trishear modelling section, unrealistic results were obtained from the kinematic models in the central region of the thrust, since the algorithm delivered a shallow thrust geometry which is inconsistent with the structural style prevailing in Laramide structures (e.g. Allmendinger *et al*., 1983). A preliminary exercise using ED helped to highlight the inconsistencies of this earlier 3D structural model and provided new insights regarding the thrust geometry.

Figure 50 shows the results of the ED model using the initial shallow thrust geometry. Figure 50a shows the thrust surface colored by throw distribution together with the cutoff lines (fault polygons). Notice that the throw distribution depicts a displacement pattern typical of a fault-propagation fold, with the displacement decreasing upwards. Along strike, the displacement decreases towards the north as well. The black vertical line in Figure 50a represents the vertical observation grid shown in Figure 50b. On the vertical observation grid, a significant misfit is observed between the input and the modelled beds. For example, the top of the

input Freemont Formation (blue) and its corresponding ED modelled surface (magenta) show a misfit in the amplitude of the fold of about 500 m. This means that there is not enough displacement below the Freemont Formation top to thrust up the anticline such that it fits with the observed fold. Figure 47a shows that there are no deeper horizons (i.e. fault polygons) that can provide the slip required to correctly model the amplitude of the anticline.

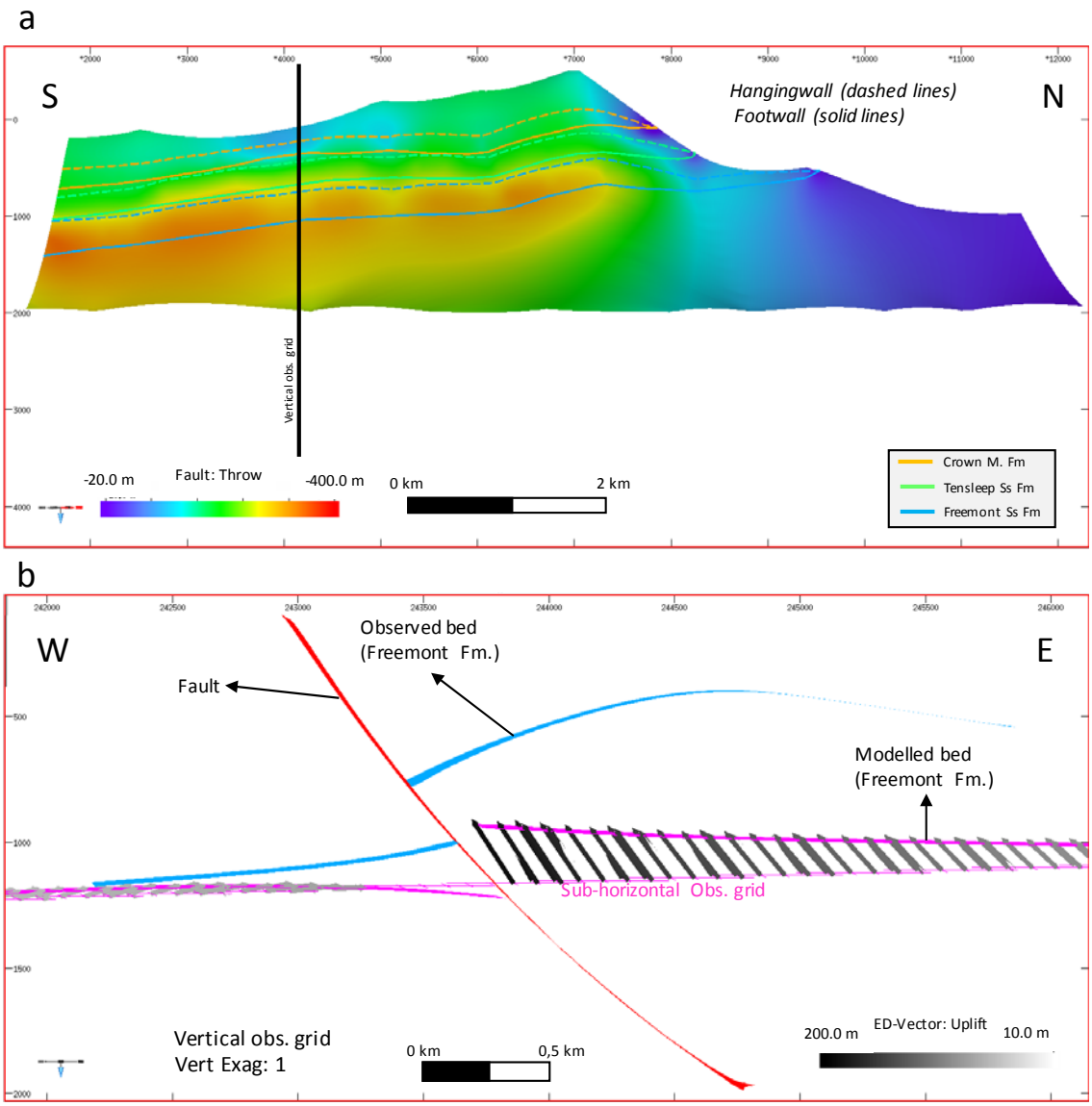

Figure 50 ***a.*** *The input thrust surface colored by throw. Warmer colors mean higher throw. Fault polygons (cutoff lines) for Freemont (low), Tensleep (mid) and Crown Mountain (up) tops are shown. Dashed lines represent the hanging wall and solid lines the footwall cutoffs. Vertical black line indicates the position of the vertical grid in b.* ***b.*** *Vertical observation grid (location in a and Figure 46). Blue is the input, and magenta is the modelled Freemont top. ED uplift vectors on the modelled surface are colored by their magnitude.*

In the absence of deeper horizons, I created pseudo-horizons below the Freemont Formation. At this point the restriction to create deeper horizons was related to the detachment depth. To deal with this, the thrust was extended 2 and 1 km along strike towards the north and south, respectively, and 2 km down dip in a more planar fashion as described in the previous section (Figure 51). Figure 51b shows the resulting thrust geometry after extending the thrust plane down dip and along strike. The final thrust geometry preserves similar characteristics from the original, mainly above 2000 m depth up to its upward termination, the dip angles average ca. 52°. Below 2000 m the thrust is planar with dip angles between 35 and 40° (Figure 51b). The manually created deeper fault polygon is shown in Figure 51b in magenta, and it gives about 2 km of additional vertical throw (ca. 3 km of net slip) to the ED model. This amount of slip is considerably higher compared to the slip predicted by the trishear model at the reservoir level (1.4 km), which imply higher strain in the ED model as consequence of higher decreasing displacement gradient (Figure 51b).

With this deeper, higher thrust displacement, the desired fold amplitude could be reached. The ED modelled top of the Tensleep reservoir shows a good fit in the forelimb (Figs. 52 and 53b). However, the modelled Freemont and Crown Mountain Formations tops, below and above, were gentler close to the fault, and the anticlinal hinge in these beds was shifted towards the fault compared to the input beds. Sensitivity tests showed that this issue could be fixed by decreasing the displacement of these beds 40%, implying a higher displacement gradient and consequently a higher strain. This modification is shown in Figure 51b, where the fault polygons for the Freemont and Crown Mountain tops are much narrower than in the input model. These modified fault polygons resulted in a reasonable fit of these beds (Figure 53a and c). However, the throw distribution of this modified model is rather inconsistent. The throw in the Tensleep top is higher than in the Freemont and Crown Mountain tops, below and above (Figure 51b). One would expect instead the throw to decrease up-section from the Freemont top to the Crown Mountain top. As I said, the model is preliminary, and requires more work to reach a more geologically consistent throw distribution on the thrust.

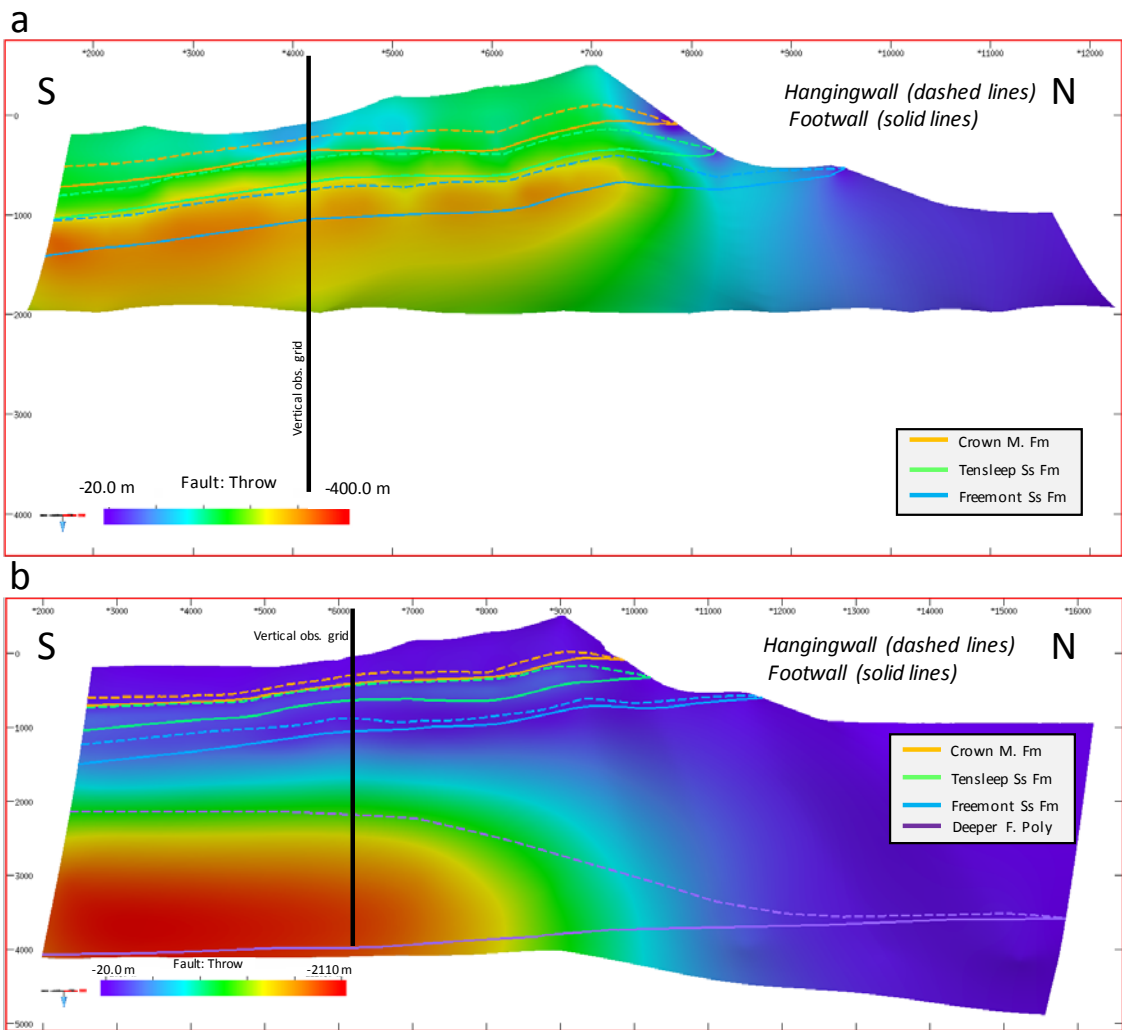

Figure 51 ***a.*** *Input thrust surface and unmodified fault polygons.* ***(b)****. Modified thrust geometry and fault polygons to obtain a good fit using ED. In a and b the thrust is colored by throw. Warmer colors mean higher throw values. Fault polygons (cutoff lines) for Freemont (low), Tensleep (mid) and Crown Mountain (up) tops are included. In (b) an additional deepest fault polygon (purple) was added. Dashed lines represent the hanging wall and solid lines the footwall cutoffs. Vertical black line indicates the position of the vertical observation grid.*

Figure 52 displays a 3D view of the input Tensleep reservoir top (left) and its corresponding ED deformed top (right). In general, the ED model is able to capture the geometry of the Tensleep top reasonably well in terms of fold width, length and curvature. Although the model needs a little bit more uplift, the results honor fairly well the input surface.

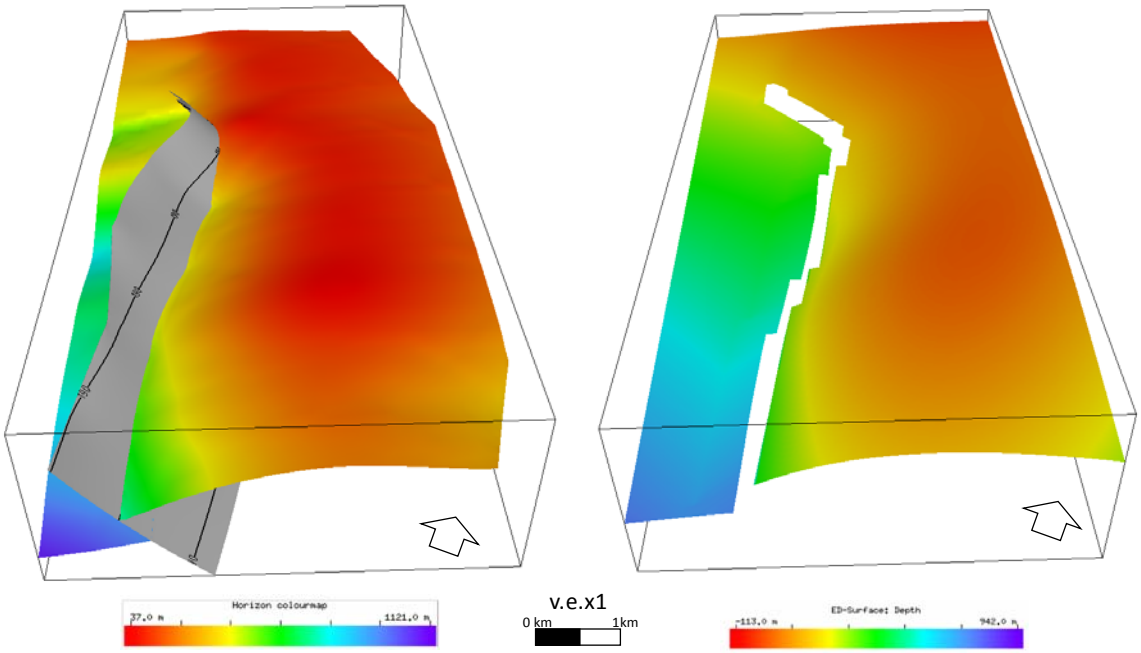

Figure 52. Perspective view of the input Tensleep reservoir top (left) and its corresponding ED deformed surface (right). Colors are elevation.

The vertical observation grid provides more details about the geometry and fit of the ED deformed surfaces. Figure 53a shows the comparison between the ED deformed surface of the Freemont top and the input one. The modelled bed fits well the input geometry, although the predicted uplift is higher. The ED modelled Tensleep top shows good fit in curvature, amplitude, and forelimb geometry, but the backlimb is shallower than in the input model as shown by the uplift vectors (predicted ED uplift is higher than input one, Figure 53b). The ED modelled Crown Mountain top depicts better fit in terms of curvature, amplitude, and forelimb geometry. However, there is an excess of uplift in the backlimb (Figure 53c). In the three modelled beds, the misfit in the footwall is rather high, with the modelled bed being higher than the input one (predicted ED uplift in footwall is higher than input one, Figure 53).

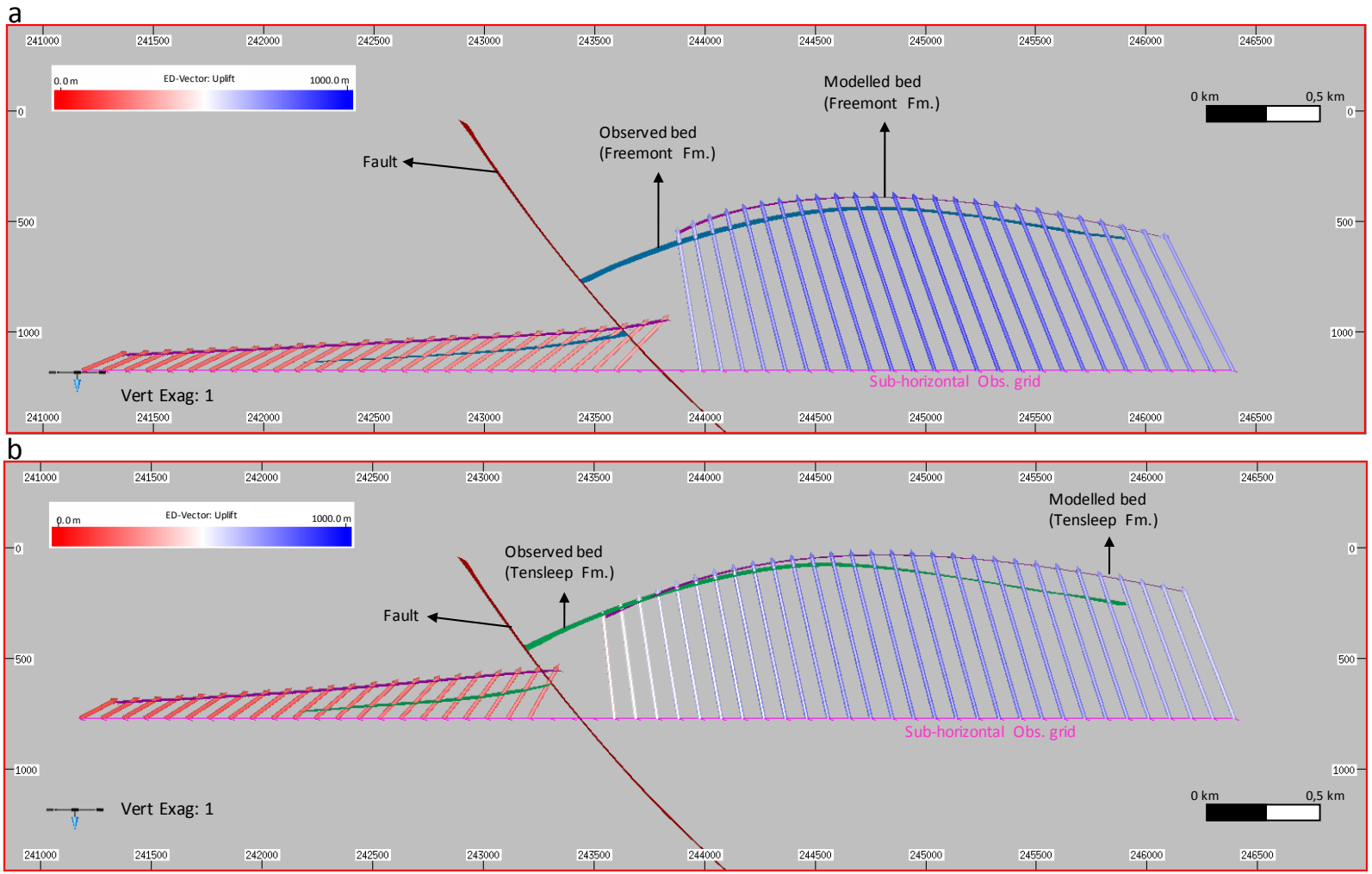

Figure 53 Vertical observation grid including input and ED modelled horizons (location of grid in Figure 46). Uplift vectors are colored by their magnitude. ***a.*** *Freemont top,* ***b.*** *Tensleep top.*

C

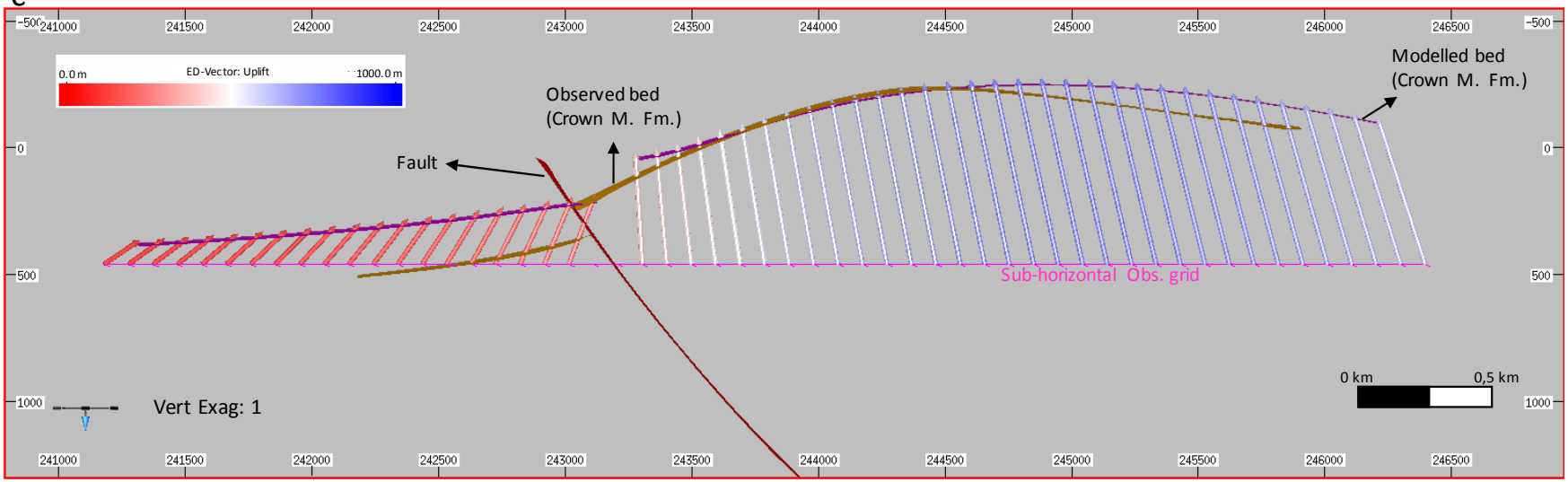

Figure 54 ***(cont.). c.*** *Crown Mountain Formation.*

5.2.2 ED Fracture Prediction

The intensity and orientation of fractures can be predicted from ED modelling since this technique delivers strain and stress tensors. Vector attributes such as the axis of maximum stretching (E1) and the axis of maximum shortening (E3) provide insight of the strain ellipse. Principal stress orientations such as S1 and S3 (maximum and minimum principal stresses) can also be visualized. Combination of these vectors with attribute-colored surfaces (e.g. maximum Coulomb shear stress) can be used as proxies for the intensity and orientation of fractures.

Figure 55 provides both proxies for fracture orientation and intensity. Figure 55a displays the the Maximum Coulomb Shear Stress (MCSS), which is a proxy for estimating the intensity of shear fractures (Dee et al., 2007). MCSS is the maximum shear stress generated when S1 is the bisector of the acute angle of the conjugated shear fractures planes (Maerten et al., 2006). The warmer colors suggest higher fracture intensity closer to the fault rupture zone, and more fracturing in the footwall (Figure 55a). Figure 55b shows the conjugate shear fractures planes, which intersect at S2 and are bisected by S1 (Maerten et al., 2006). Figure 56 combines MCSS attribute displayed in a colored sub-horizontal slice of the model with S2 at the observation grid of Tensleep reservoir. As the vertical grid in the Figure 55, MCSS color ramp suggests higher fracture intensity closer to the fault rupture zone, and more fracturing in the footwall. S2 represents the strike of the shear fracture planes. Inset cartoon in Figure 56 illustrate this situation. All the shown examples correspond to proxies for both the orientation and intensity of shear fractures. I will use the vertical observation grids of Figures 55 for comparison with the kinematic model in the next section.

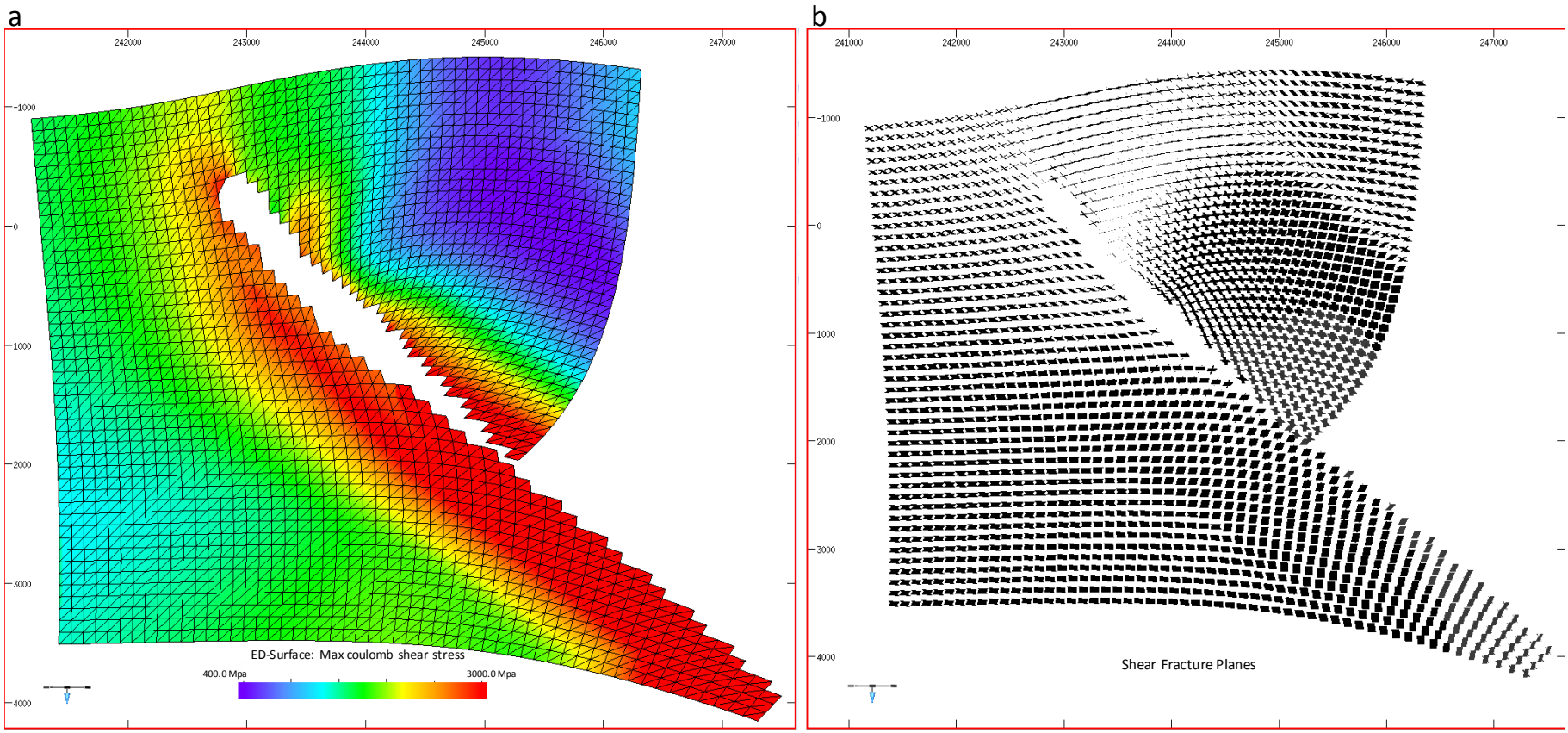

*Figure 55 Vertical observation grid displaying **a.** Max Coulomb Shear Stress. **b.** Shear fractures planes.*

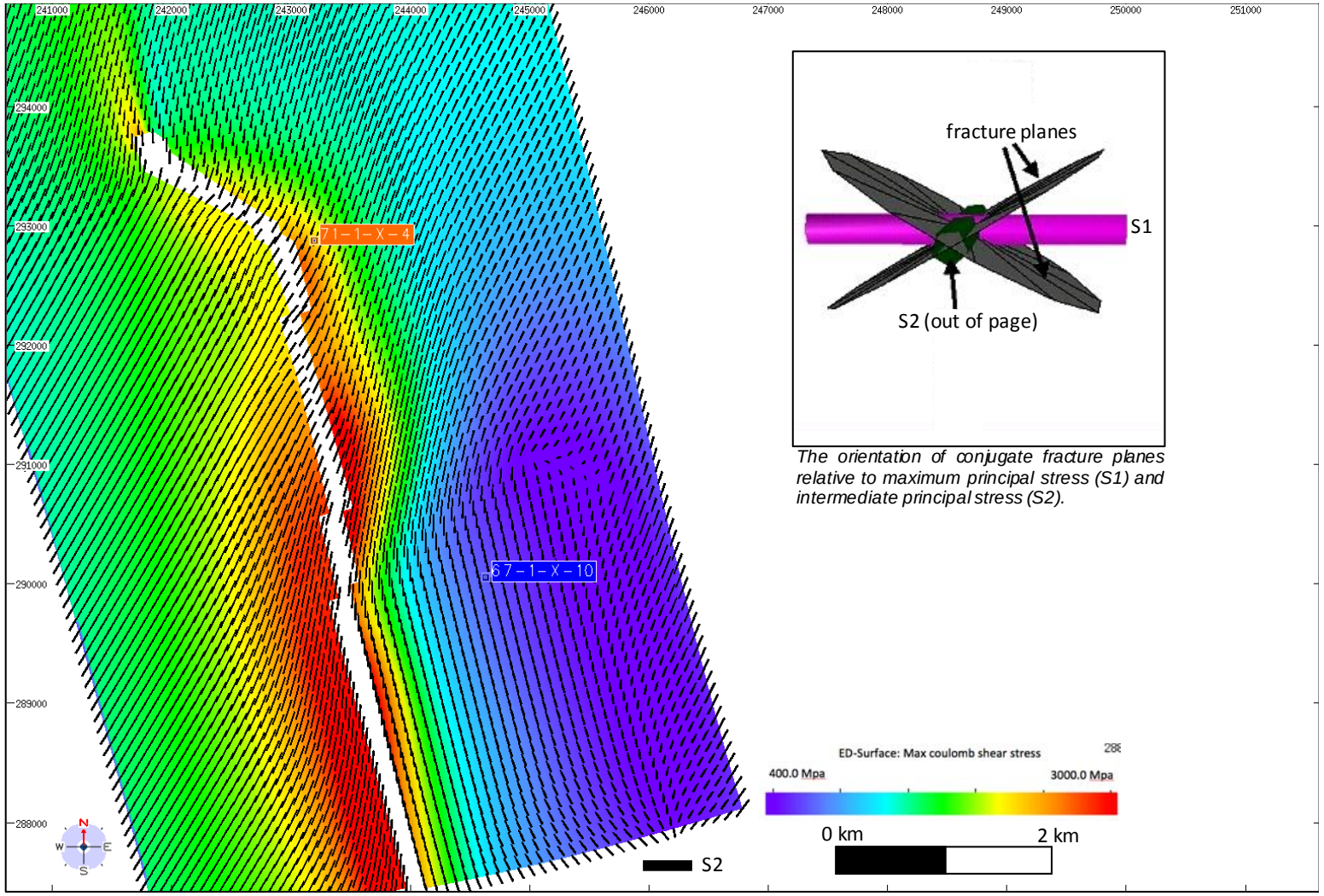

Figure 56 Horizontal observation grid at Tensleep reservoir level displaying Maximum Coulomb Shear Stress (MCSS) and intermediate principal stress (S2, black arrows). Inset cartoon modified after Badley, (2004).

Open fracture data from wells 71-1-X-4 and 67-1-X-10 were used to test the ED fracture prediction (Figure 57). Open fractures are the only family displayed in the wells since at Tensleep reservoir level this set is the dominant (Wilson et al., 2015). The fractures from these two wells (Figure 57b) seem to correspond to the oblique-hinge tensile fractures described by Olsen et al. (1993), Doll et al. (1995), Cooper et al. (2006) and Wilson et al. (2015). Therefore, one should expect them to be parallel to S1. Figure 57a shows a sub-horizontal observation grid at the Tensleep reservoir level populated with vectors indicating the orientation of S1 (black arrows). Close ups of the areas near the wells (insets, Figure 57a) show that the fractures in the wells (grey planes in insets) are similar in orientation to the predicted orientation of S1. The predicted S1 orientation fits better the fractures orientation in the well close to the thrust (71-1-X-4) than in the well in the backlimb area (67-1-X-10). This is reasonable, since the ED model fit is better in the forelimb area. Based on well measurements, Lorenz and Cooper (2013) and Wilson et al. (2015) determined a W-NW orientation of the present-day maximum horizontal stress (S1), which is similar to the S1 orientation predicted by the ED model. Figure 58 shows the same observation grid as Figure 57 but this time with MCSS attribute displayed in a colored sub-horizontal slice of the model. MCSS suggests that a lower intensity of shear fractures is expected in the well 67-1-X-10, while moderate to high shear fracture intensity is expected in the well closer to the thrust, 71-1-X-4.

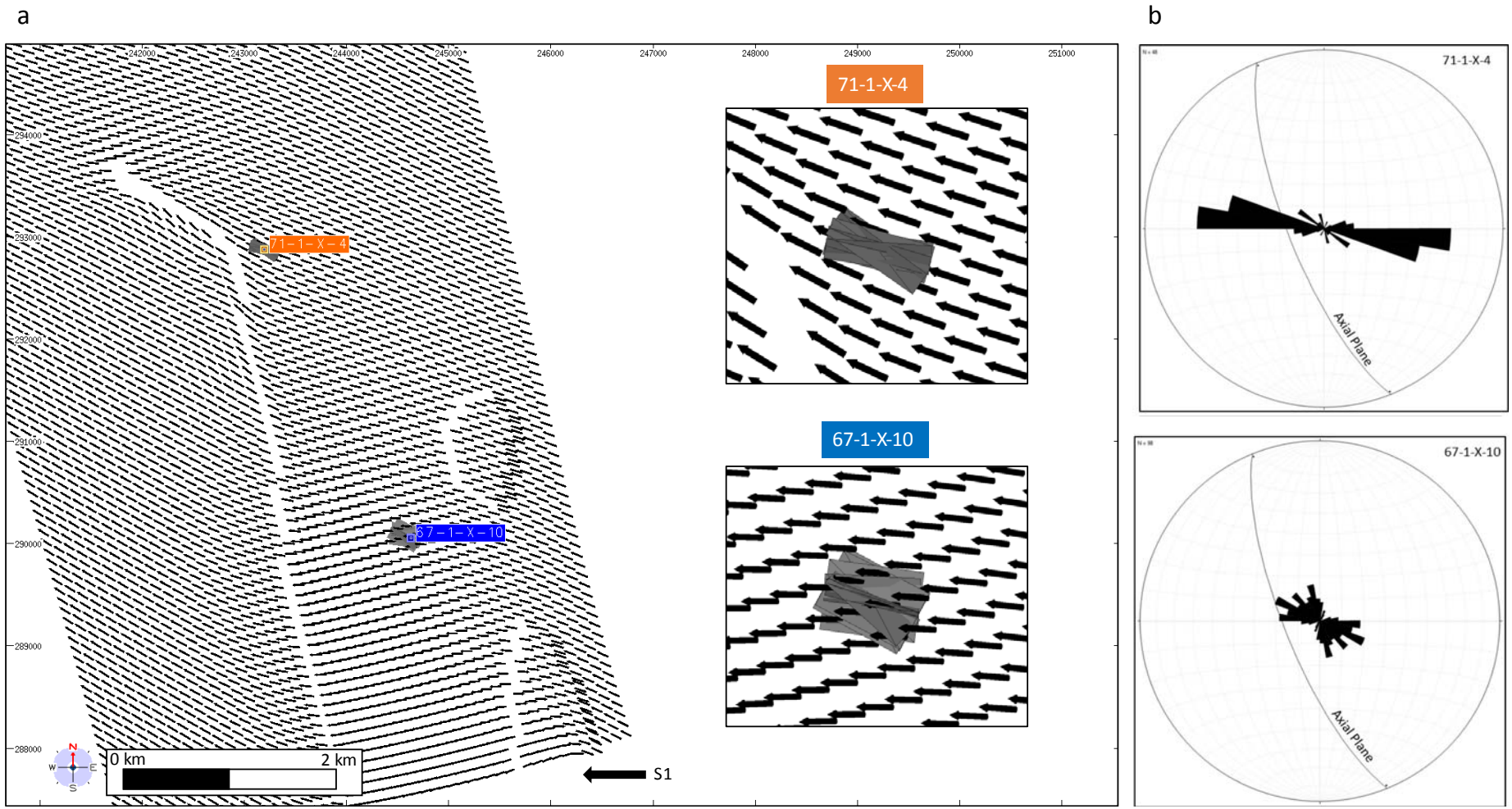

Figure 57. Horizontal observation grid at Tensleep reservoir level displaying maximum principal stress (S1, black arrows). Zoom areas correspond to locations nearby the two wells with only fracture data. Grey planes in the zoom are open fractures observed in the wells. ***b.*** *Rose diagrams displaying strike of open fractures at reservoir level in the wells. These fractures are similar to the oblique hinge tensile fractures described by previous authors in the area.*

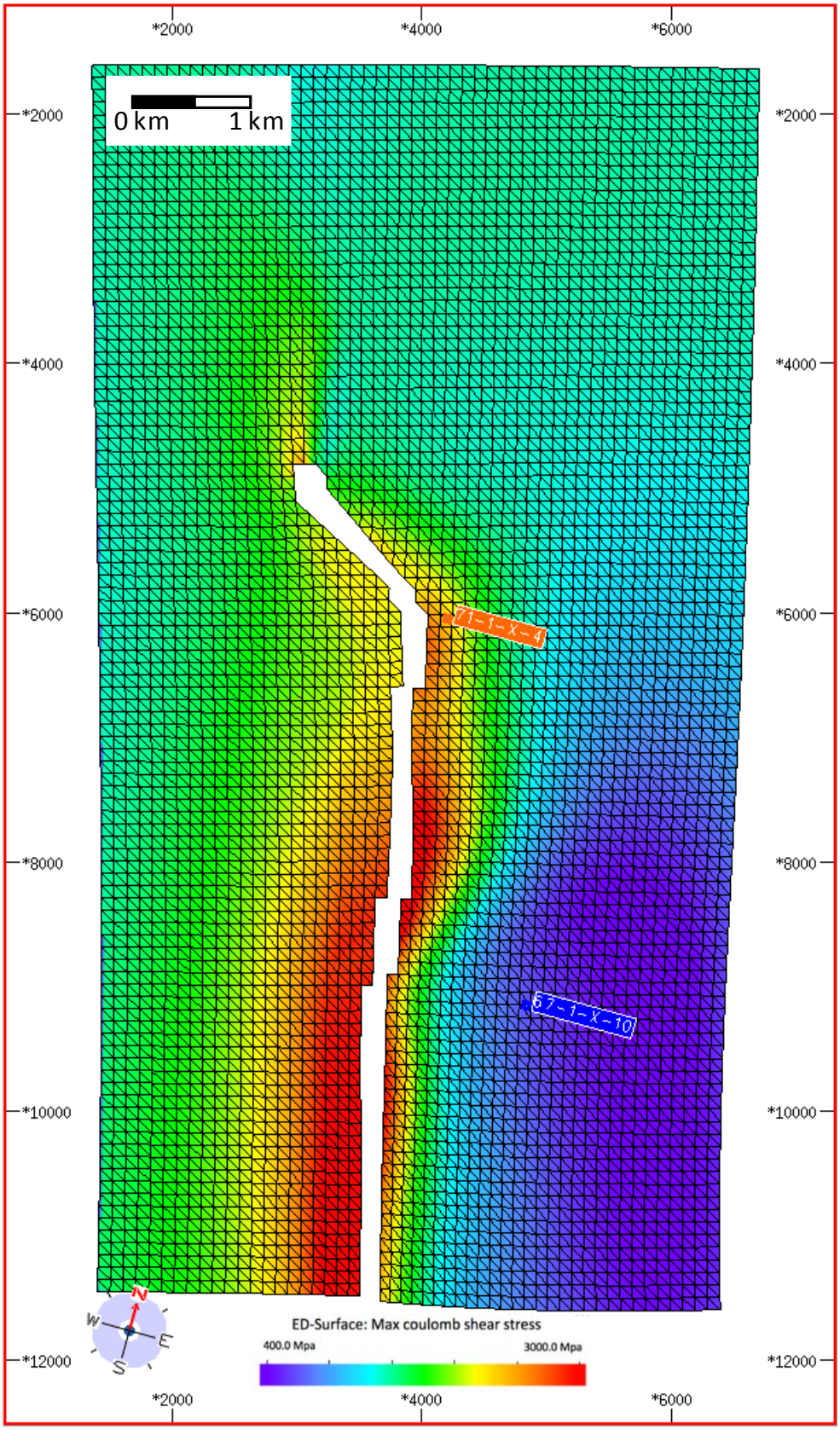

Figure 58. Horizontal observation grid at Tensleep reservoir level displaying Maximum Coulomb Shear Stress (MCSS). Lower intensity of shear fractures well 67-1-X-10, while moderate to high shear fracture intensity well closer to the thrust, 71-1-X-4.

5.3 Comparison of trishear and ED proxies

Before comparing the models, let's look at what each model delivers separately. Figure 59 shows a vertical slice of the deformed ED model on the vertical observation grid (location in the figures 49 and 50a). The ticks indicate the principal strain axes. Black ticks represent the orientation of the maximum shortening (-) axis (E3), and green ticks the maximum stretching (+) axis (E1). The length of the ticks was plotted using the computed magnitude of stretching and shortening along the axes (times 300). Five inset close-up windows are included to observe the vectors in detail in five areas: 1. Closer to the rupture zone in the hanging wall; 2. Far from the rupture zone in the hanging wall; 3. Above and closer to the fault tip; 4. In the footwall far from the fault tip; 5. Closer to the rupture zone in the footwall.

Based on the length of the axes, it is possible to suggest that, in general, the deformation in the hangingwall is dominated by shortening since E3 tends to be greater than E1. This is more evident in area 1 close to the thrust where the E1 ticks have the highest lengths. Also, this is observed in area 2 but to a less degree. Ticks in areas 3 and 4 show almost the same length for both E1 and E3, suggesting small or null strain in this region. This corresponds to a low strain region where the fault related deformation decreases substantially upward. In the footwall region (5) close to the rupture zone, the ticks' length suggest the second larger strains. The strain is dominated by stretching since E1 is much higher than E3.

Another way to observe the magnitude of the strain is by colouring the vertical grid as function of volume changes in the deformed model (Figure 60a). Negative values (blue) suggest loss of volume (-ve), and positive values gain of volume (+ve). Loss of volume in the hanging wall might be explained by the shortening. That disagrees with the observed tensile fracture in the wells as described in the previous section. On other hand, volume gain is observed in the footwall area, which has undergone stretching according to the observation in figures 59, and 60b. The colours in the area surrounding the fault tip point are faded suggesting very small volume changes due the low strain observed in this area.

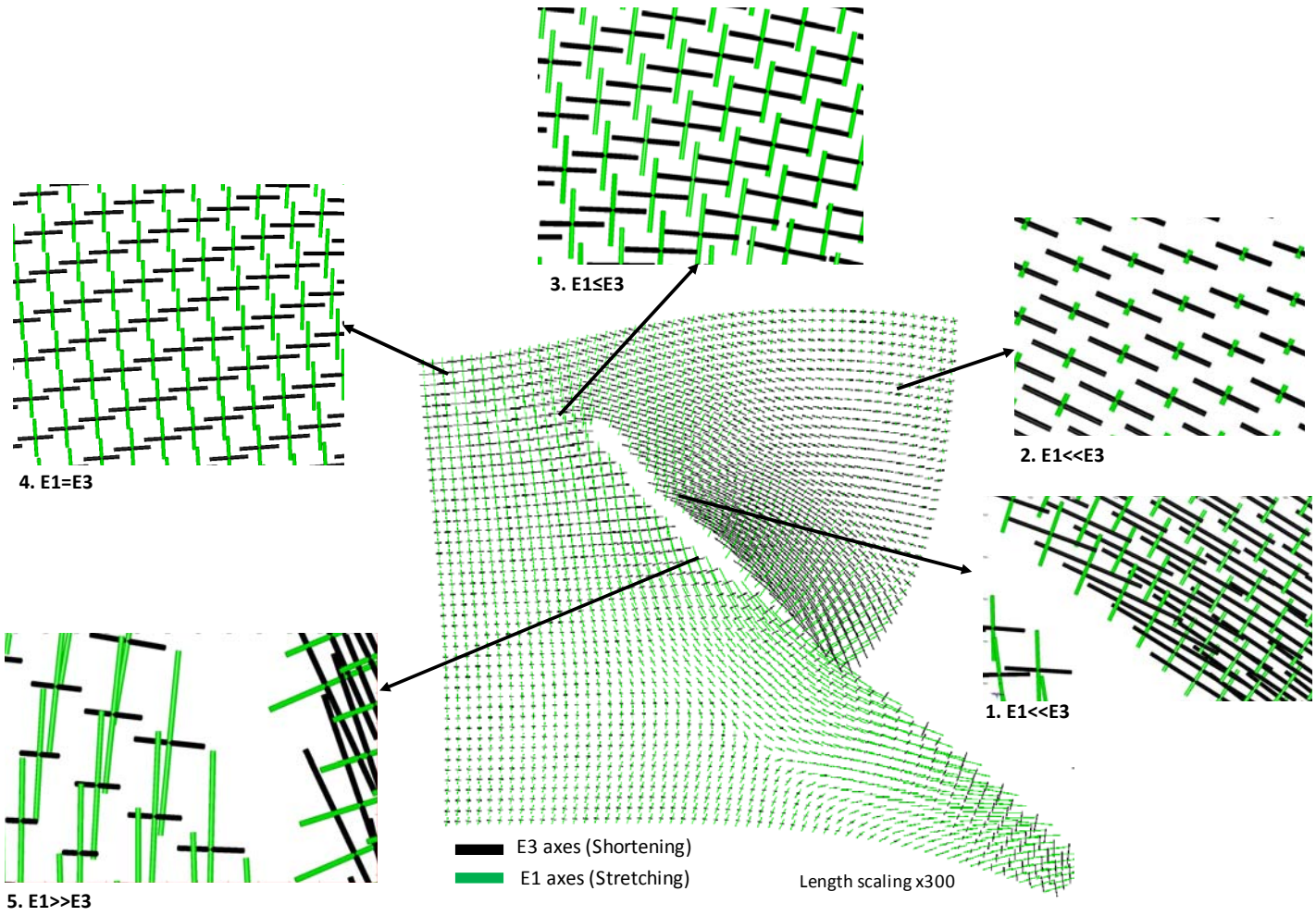

Figure 59 Vertical observation grid (location in Figure 46) displaying principal axes of strain (E1 and E3). Zoom areas (inset close-ups) show in detail the orientation of the strain axes close to fault rupture zone, fault tip point, footwall and hangingwall. Tick lengths are proportional to the stretch magnitude and are exaggerated 300 times.

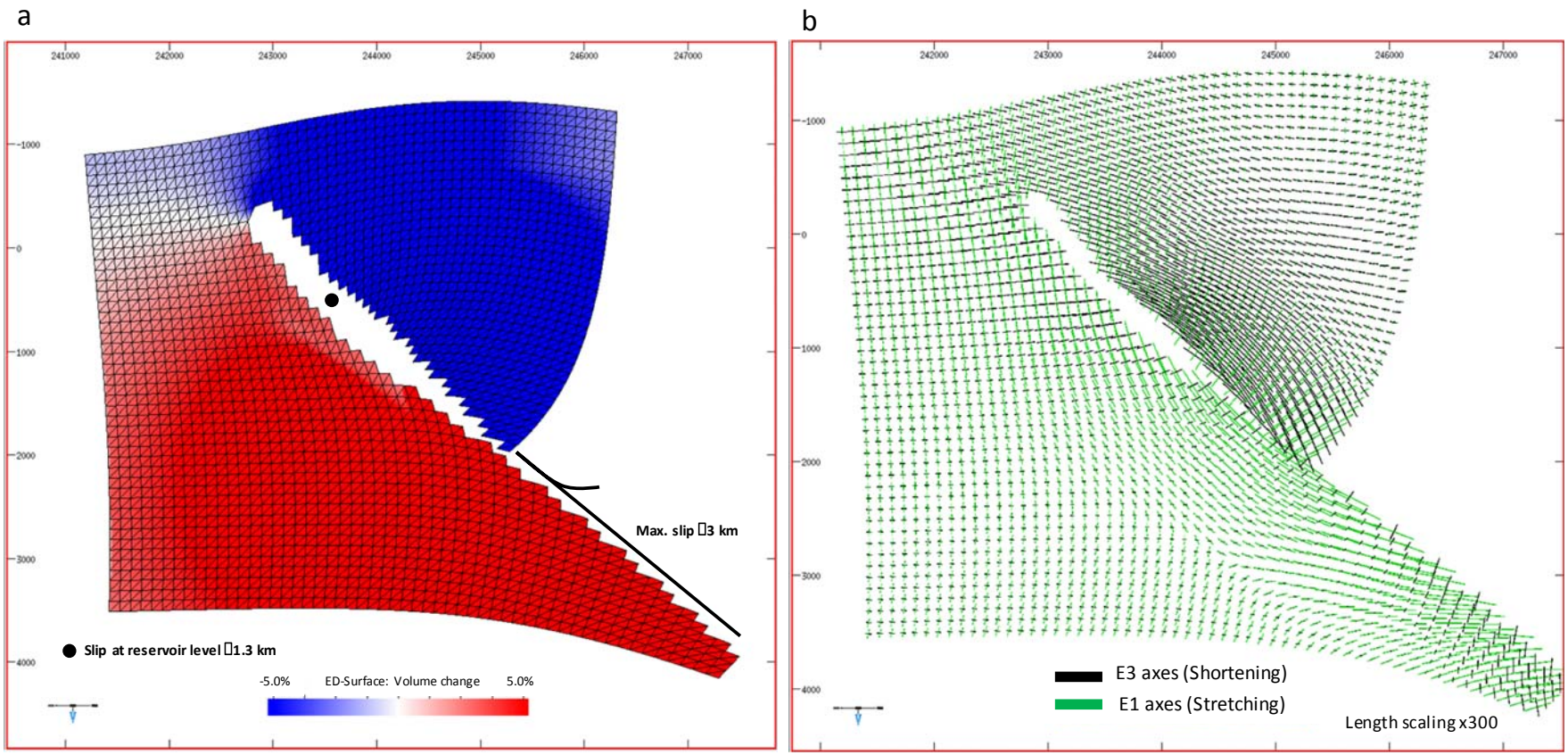

*Figure 60 Vertical observation grid (location in Figure 46) displaying **a.** Volume change, **b.** Principal axes of strain ellipse.*

Strain ellipses representing the strain field predicted by the trishear model are shown along section D (Figure 61b). The modelled beds and thrust are also plotted. The strain ellipses where plotted along the Tensleep reservoir and the Crown Mountain Formation above. Rectangles are close-ups from: (1) the backlimb, (2) crest of the anticline, (3) forelimb, and (4) footwall. The ellipticity (ratio between short and long ellipse axes) indicates the amount of strain. In the plots, the lines of no finite elongation (LNFE) are also shown. These LNFE are often used as proxies for shear fracture planes (Allmendinger, 1998; Hardy and Allmendinger, 2011). In general, the ellipticity in the hangingwall is low (Figure 61b, 1-3). Small strains are observed at the backlimb (1) and crest (2) of the anticline. The ellipticity is higher in the forelimb (3) and the footwall (4). Additionally, counterclockwise rotation of the ellipses is observed in the footwall (4).

Comparison between the ED and trishear proxies is interesting (Figures 61a and 61b). The black dot (both figures 61a and 61b) in the thrust is used as a reference. Both trishear and ED coincide in higher deformation in the forelimb and footwall (Figures 59 and 61) close to the thrust. They also predict that the deformation decrease towards the backlimb (Figure 61a and 61b 1) and the anticline crest (Figure 61a and 61b, 2). Rotation of E1 with respect to a horizontal axis is another interesting feature. While ED predicts large clockwise rotation of E1 in the hangingwall, trishear just shows a subtle clockwise rotation in the forelimb (Figure 61a and 61b, 3). Slight counter-clockwise rotation of E1 is predicted by trishear in the anticline crest (Figure 61b, 2) and towards the backlimb (Figure 61b, 1). This disagrees with the ED model predictions. Both ED and trishear models predict similar counter-clockwise rotations for E1 in the footwall (Figure 61a and 61b, 4). In general, both models produced similar strain results in the footwall region close to the thrust. The conjugate fracture planes of ED can be compared to the LNFE of trishear. These two proxies are different in nature, but they are both used to predict shear fractures. The orientation of the conjugate shear planes produced by the ED model (Figure 62a, 3-4) are somewhat similar to the LNFE of trishear (Figure 62b, 3-4), both in the forelimb and footwall, although there are some differences. In the forelimb, one of the conjugate shear planes is more parallel to bedding that its corresponding LNFE in trishear, and in both the forelimb and footwall, the acute angle between the conjugate shear planes in ED is larger than the corresponding angle between the LNFE in trishear.

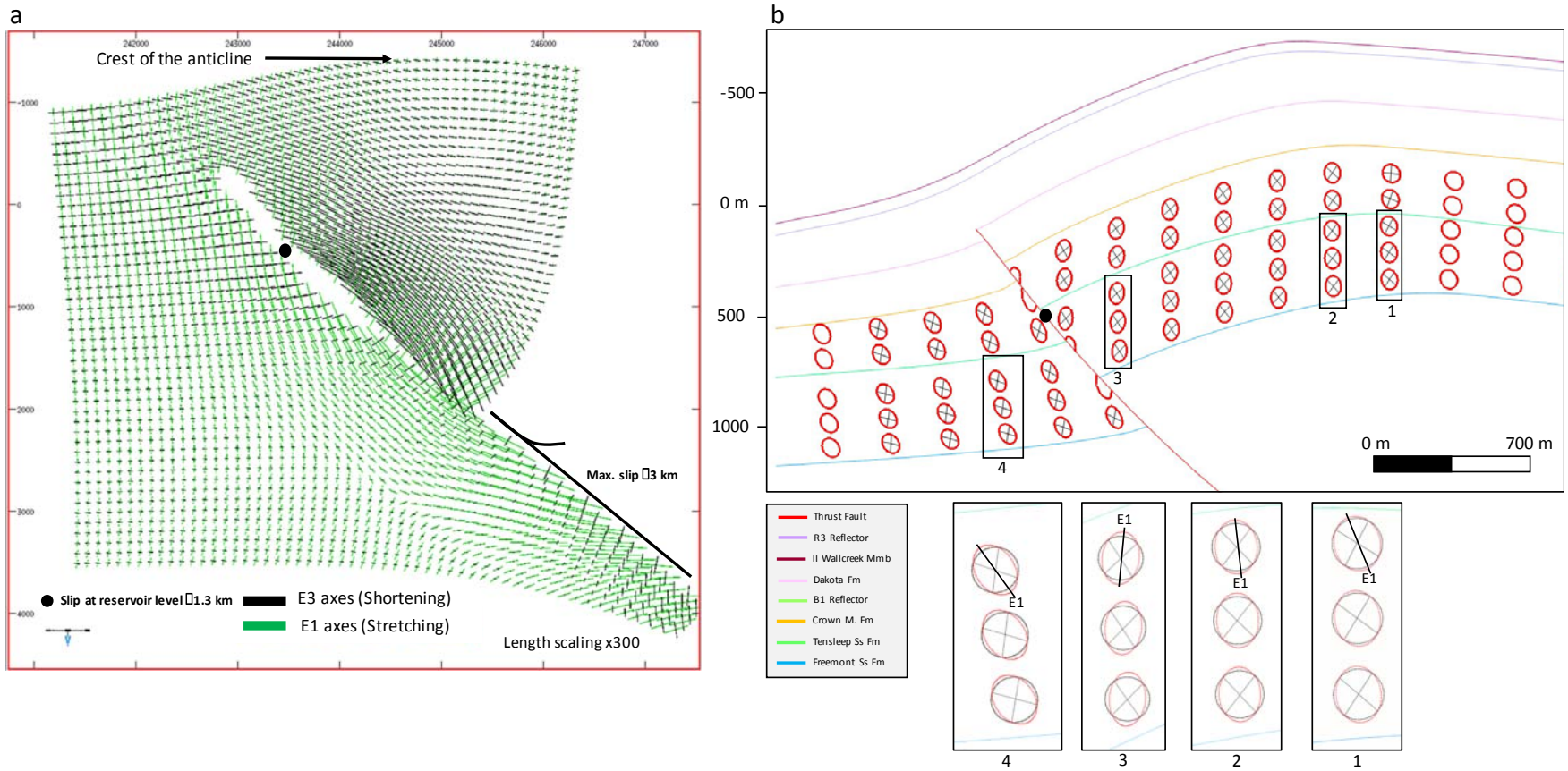

*Figure 61**a.** Vertical observation grid displaying the principal strain axes (location in Figure 46), **b**. Section D displaying the trishear modelled beds and thrust, strain ellipses (red), and LNFE (black lines). Rectangles (3-4) are close-ups of the strain ellipses in the hanging wall and footwall regions. The black dot in a and b is used as reference.*

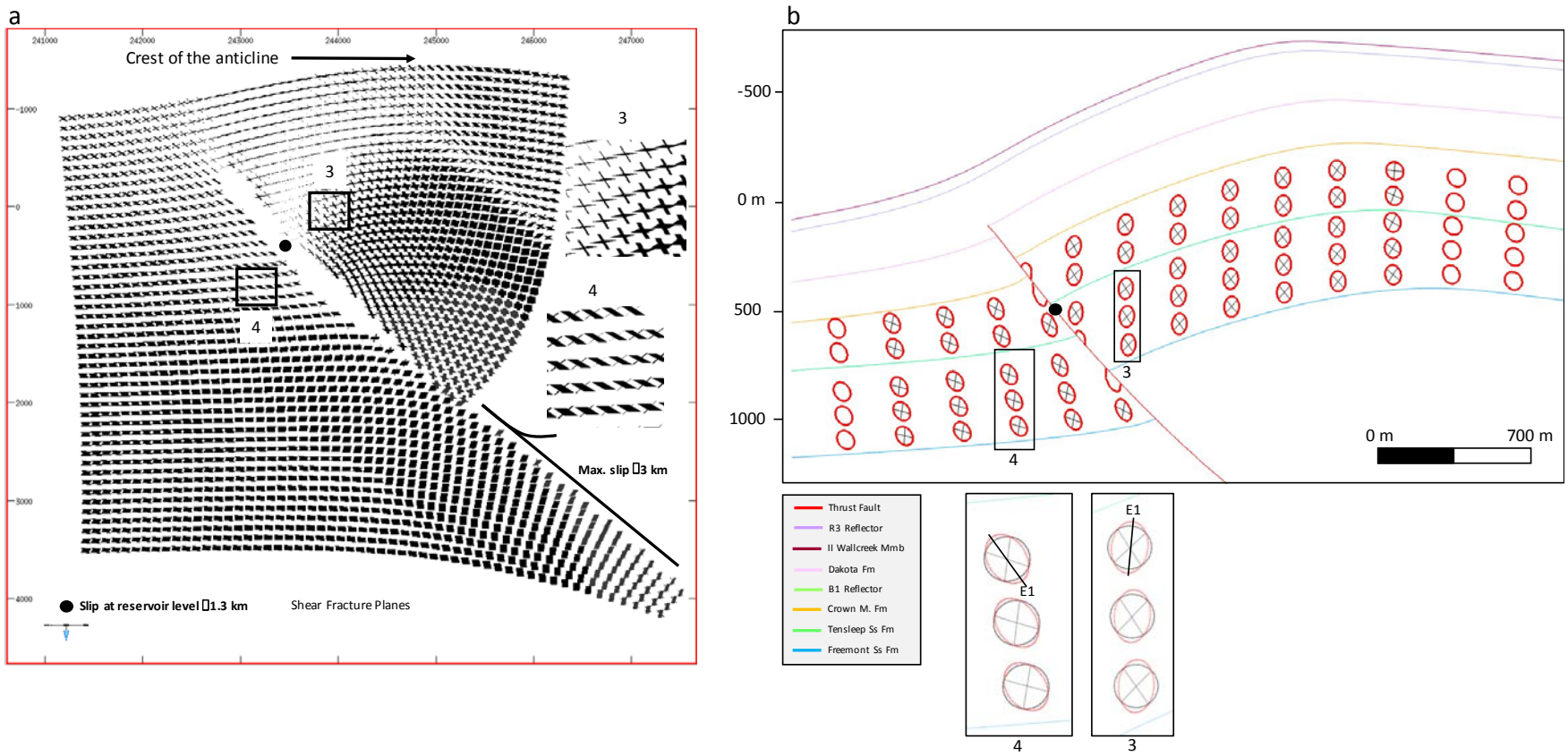

Figure 62 ***a.*** *Vertical observation grid displaying shear fracture planes (location in Figure 46). Inset pictures (3-4) are close-ups of shear fracture planes in hanging wall and footwall regions.* ***b****. Section D displaying the trishear modelled beds and thrust, strain ellipses (red), and LNFE (black lines). Rectangles (3-4) are in the same location than in a. Black dot in a and b is used as reference*

5.4 Discussion

This study has tested the application of inverse trishear and forward elastic dislocation modelling techniques to a relatively simple structure, the Teapot Dome. During the study, a workflow has been developed that starts with the interpretation of top horizons in the seismic data. Then, the 2D trishear inversion algorithm is applied to a set of cross-sections containing the depth converted horizons to reconstruct the fold forelimb, thrust, and footwall geometry. Beds and thrust traces contained in the best-fit models are interpolated and extrapolated between and beyond the cross-sections in Move to produce the 3D structural model. Thrust and horizons surfaces reconstructed in trishear were imported to TrapTester to perform Elastic dislocation modelling (ED). The ED technique delivers strain tensors. Stress tensors were computed from the ED strain tensors using appropriate rock properties. The outputs provided for ED model are used as proxies for the orientation and distribution of fractures in the anticline. The application of the implemented workflow helped to better understand the geometry, kinematics and mechanics of the Teapot Dome, especially since the dataset does not provide a complete picture of the structure.

Application of both trishear and elastic dislocation modelling techniques to the Teapot anticline, allowed highlighting the benefits and limitations of these structural modelling methods. This was possible because both methods have to tackle a common issue, the high uncertainty caused by no-seismic image zones in both the 2D and 3D seismic data. The data used in this study is a typical example of a dataset with poor seismic imaging of the steeply dipping forelimb and lack of coverage in the footwall region. Additionally, the underlying thrust is not clearly imaged and its geometry is difficult to determine. This scenario may lead to different interpretations for the structure. In this study, I assumed a simple configuration consisting of an anticline over a single major thrust. However, other interpretations can be suggested, for example two or more thrusts or an overturned forelimb. Although the results show that there is still much to improve in the modelling process (e.g. better fit in the ED model), the experience acquired demonstrates that the workflow was appropriate and applied in the right sense given the limitations of the dataset.

In general, 2D trishear modelling does a good job in the reconstruction of the thrust and the beds in the forelimb and footwall areas with no data or poor seismic imaging. Very few tools can provide such a reconstruction with such poor data constraints. Several studies at Teapot Dome, most of them aimed to describe fractures (e.g. Friedmann, 2004; Schwartz, 2006; Friedmann & Stamp, 2006; Cooper *et al*., 2006; Lorenz & Cooper, 2013; Wilson et al., 2015;

Schneider *et al*., 2016), show limited horizons due to the lack of 3D seismic coverage and poor seismic imaging of the thrust and forelimb. Figure 63 shows the geological surface representing the top of Dakota Formation presented by Cooper *et al*. (2003, Fig. 63a), and Friedmann (2004), Schwartz (2006), Lorenz and Cooper (2013, Fig. 63b), compared with the same top generated in this study (Fig. 63c). Note that the surface is limited to the 3D seismic cube, since only a small part of the forelimb is controlled by the seismic, a very steep and incomplete surface was obtained in previous studies (Fig. 63a-b). These surfaces do not include the footwall region despite that the data set provides a 2D seismic line (D) with full coverage of the backlimb and footwall, and partial coverage of the forelimb (Fig. 28a). However, this information is local and it is difficult to integrate with the 3D seismic cube. In this scenario, trishear appears as an alternative to address these issues. Figure 63c displays the Dakota Formation top obtained after applying trishear modelling. Note the reconstruction of the forelimb and footwall, and the thrust trace.

Without good seismic imaging of the forelimb and footwall, the thrust geometry is another critical issue. Figure 64 compares the thrust position suggested by Wilson et al. (2013, Fig. 64a) and the one interpreted in section S1 (Fig. 64b). Both interpretations are based on the 3D seismic data. In Figure 64a the thrust was placed in the zone where the seismic image is blurry. Note, the absence of the footwall beds. Figure 64b displays the kinematic reconstruction of the forelimb and the footwall after the application of trishear. This allows to place the thrust in a more reasonable position. This interpretation looks similar to the interpretation of section D (Fig. 64c), which has more seismic coverage and geologic control. Figure 64d shows a comparison between the deformed beds modelled with trishear against those included in the provided data set (RMOTC, 2005a, b) on section S1. The fit is very good, and the reconstructed beds in this thesis follow better the seismic reflectors (Figures 41-48).

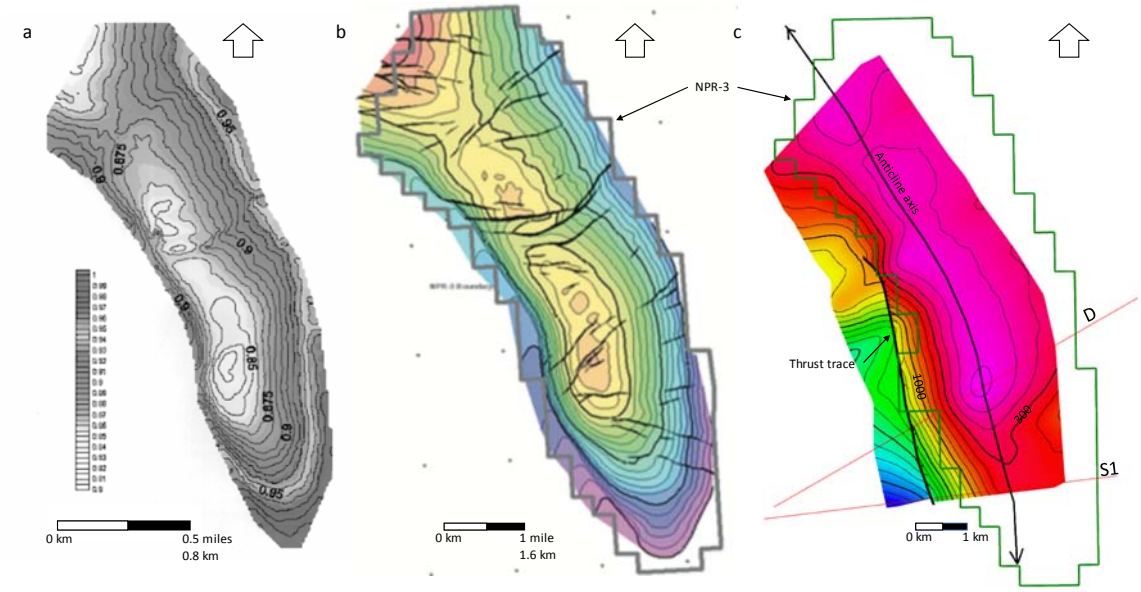

Figure 63 ***a.*** *Time-structure map of top of Dakota Formation after Cooper et al, (2003),* ***b.*** *Time-structure map of top of Dakota Formation after Friedmann (2004), Schwartz (2006), and Lorenz and Cooper (2013). Black lines are fault traces.* ***c****. Structural map in depth (m) of top of Dakota Formation from this study. In b and c, the polygon is the boundary of NPR-3. In c, the location of sections D and S1 in Figure 60 is shown.*

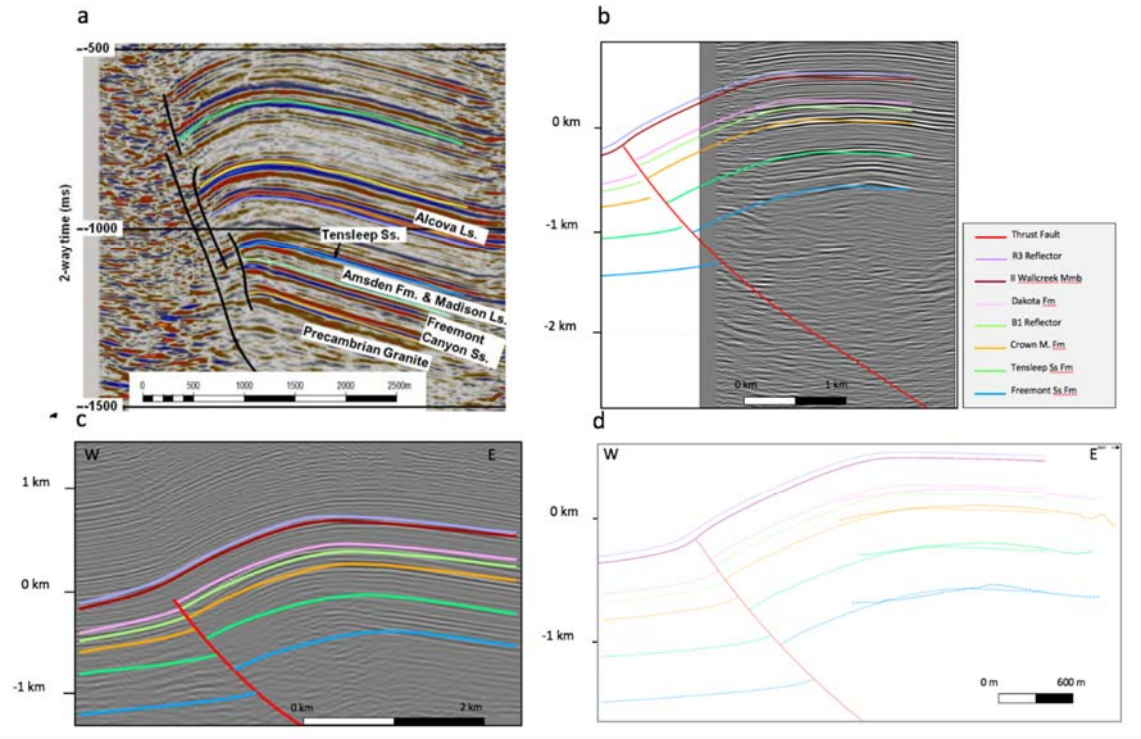

*Figure 64****.*** *Horizons (colored lines) and thrust interpretation (black lines) of 3D seismic in time domain. The seismic profile has unknown vertical exaggeration. After Wilson et al (2013).* ***b-c*** *Modelled beds and thrust superimposed to the seismic profile S1 (****b****) and D (****c****).* ***d****. Cross-section along S1 of the 3D structural model after trishear modelling, compared with the surfaces provided in the original dataset (RMOTC, 2005a, b)*

Different geometries along the anticline represent a challenge in the application of the trishear algorithm. Backlimb dip angles are shallower in the northern and southern regions towards the fold terminations. In the central part, the fold shows stepper backlimb dips. Therefore, the kinematic algorithm predicts a listric thrust with shallower detachment in the central region, and a more planar thrust continuing down section in the northern and southern regions, which is an awkward thrust geometry. Elastic dislocation modelling demonstrate that this geometry is unrealistic from the mechanical point view. Thus, kinematic predictions (including fractures) on the backlimb in this central region might not be valid.

Validation of the kinematic reconstruction was one of the most important benefits provided by elastic dislocation (ED) modelling. Earlier results suggested that the thrust had to be extended down dip, at least two kilometers. Also ED suggested a modification of the slip gradient to make it higher. However, the half-space in ED modelling behaves as a uniform rheology, which might not be true since layered anisotropy may be present. Nonetheless, the modelled rheology is fairly homogeneous, consisting of mainly sandstones interbedded with carbonates. Additionally, this is a reasonable approach for calculating strain.

The elastic dislocation modelling uses the thrust and beds in their post-deformation position (present-day) to compute the displacement vectors and strain tensors. These surfaces are immersed into the same isotropic elastic medium and both thrust and beds undergo deformation. This is opposite to kinematic models, where the thrust trajectory is fixed. TrapTester allows correcting for the deformation of the thrust surface such that it fits its present position. However, this is a time-consuming task, the software needs to perform several iterations to reach a reasonable solution. A pre-model restoration step consisting of moving the surfaces to their present day post-deformation state did not work properly. This is the reason why there is an offset of about 300 m between the modelled and interpreted thrust. Although this distance is small, it affects the comparison of fractures in wells with the ED model attributes.

Trishear only generates 2D strain on the modelled cross sections. The 3D structural model derived from 2D trishear modelling does not contain strain information between sections. Therefore, it is only possible to predict fractures in the cross-sections using 2D trishear. Ellipticity of the strain ellipses gives an idea of the strain intensity, and the lines of no finite elongation (LNFE) can be used as proxies for shear fractures (Allmendinger, 1998). However, most of the fractures in the studied wells are tensile fractures. Most of the wells are in the backlimb, where trishear does not do a good job. Therefore, the potential of trishear for

predicting fractures in the wells in this case is very low.

ED offers more alternatives in the generation of fractures, since the model can generate strain and stress tensors in 3D. This information was used to plot maximum Coulomb shear stress (MCSS) and conjugate shear planes in both cross-section and map view, which are proxies for the intensity (i.e. density) and orientation of shear fractures, respectively (Dee et al., 2007). The fractures in the selected wells, however, are predominantly tensile fractures according to Olsen *et al*. (1993), Doll *et al*. (1995), Cooper *et al*, (2006), and Wilson *et al*, (2015). Thus, they should be parallel to the maximum compressive stress (S1). A plot of S1 in the ED model at the reservoir level (Figure 57a) shows that S1 is sub-parallel to the fractures observed in the selected wells, one close to the thrust and another in the backlimb area. This shows that the ED model has predictive capabilities for the orientation of tensile fractures in the anticline (and perhaps also for the orientation of shear fractures). The MCSS suggests higher fracture intensity closer to the thrust along strike and down dip. The fracture intensity is higher in the footwall damage zone (Figures 55a and 56). Comparison of trishear and ED proxies suggests that, in general, both models produced similar prediction in the orientation of the principal strain axes, mostly in the footwall region close to the thrust. However, there are differences in comparable proxies such as the ED conjugate shear planes and the trishear LNFE.

Both techniques have been complementary in this project. Trishear helped reconstructing the geometry of the structure and ED helped validating and modifying the reconstructed trishear geometry, including the thrust and its cutoffs. However, for a better comparison between the trishear and ED models, one would need a complete dataset of the anticline and thrust that is used independently in both models. There is certainly some circularity in the described workflow.

These results contribute to emphasize the importance of using structural modelling techniques in DFN (discrete fracture network) generation, and not just statistical or seismic-attributes based techniques. Since fold geometries can change along strike, a unique 2D trishear model cannot be applied to the entire structure. Instead, the algorithm needs to be adjusted to the geometric variations of the structure (*e.g.* for listric thrusts, parameters such radius and centre of curvature can be modified to obtain reasonable thrust geometries). Improvement in ED modelling can be obtained by a better application of the pre-restoration model functionality in TrapTester. Also, user controlled trial and error modelling is not the best way to fit a structure. An inverse ED

method as the one described by Healy et al. (2004), would be a much more sensible way to model the anticline. These issues are the subject of future work.

6 References

Allmendinger, R. W. (1998). Inverse and forward numerical modelling of trishear fault-propagation folds. *Tectonics, 17*(4), 640-656.

Cardozo, N., & Brandenburg, J. (2014). Kinematic modelling of folding above listric propagating thrusts. *Journal of Structural Geology, 60*, 1-12.

Cardozo, N., Jackson, C. A. L., & Whipp, P. S. (2011). Determining the uniqueness of best-fit trishear models. *Journal of Structural Geology, 33*(6), 1063-1078. doi:10.1016/j.jsg.2011.04.001

Cather, S., Chapin, C., Dickinson, W., Klute, M., Hayes, M., Janecke, S., . . . Olivares, M. (1990). Paleogeographic and paleotectonic setting of Laramide sedimentary basins in the central Rocky Mountain region: Alternative interpretation and reply. *Geological Society of America Bulletin, 102*(2), 256-260.

Chiaramonte, L., Zoback, M., Friedmann, J., Stamp, V., & Zahm, C. (2011). Fracture characterization and fluid flow simulation with geomechanical constraints for a CO2–EOR and sequestration project Teapot Dome oil field, Wyoming, USA. *Energy Procedia, 4*, 3973-3980.

Coney, P. J. (1972). Cordilleran tectonics and North America plate motion. *American Journal of Science, 272*(7), 603-628.

Cooper, S. (2000). Deformation within a basement-cored anticline Teapot Dome. *Wyoming [MS thesis]: New Mexico Institute of Mining and Technology, 274*.

Cooper, S. P., Goodwin, L. B., & Lorenz, J. C. (2006). Fracture and fault patterns associated with basement-cored anticlines: The example of Teapot Dome, Wyoming. *AAPG bulletin, 90*(12), 1903-1920.

Crouch, S. L., Starfield, A. M., & Rizzo, F. (1983). Boundary element methods in solid mechanics. *Journal of Applied Mechanics, 50*, 704.

Dee, S., Yielding, G., Freeman, B., Healy, D., Kusznir, N., Grant, N., & Ellis, P. (2007). Elastic dislocation modelling for prediction of small-scale fault and fracture network characteristics. *Geological Society, London, Special Publications, 270*(1), 139-155.

Dickinson, W. R., & Snyder, W. S. (1978). Plate tectonics of the Laramide orogeny. *Geological Society of America Memoirs, 151*, 355-366.

Doll, T., Luers, D., Strong, G., Schulte, R., Sarathi, P., Olsen, D., & Hendricks, M. (1995). *An update of steam injection operations at Naval Petroleum Reserve No. 3, Teapot Dome Field, Wyoming: A shallow heterogeneous light oil reservoir.* Paper presented at the SPE International Heavy Oil Symposium.

Fox, J., Dolton, G. and Clayton, J.,. (1991). Powder River Basin. Economic Geology, US: Geological Society of America, The Geology of North America. *P-2*, 373-390.

Friedmann, S. J., & Stamp, V. W. (2006). Teapot Dome: Characterization of a CO2-enhanced oil recovery and storage site in Eastern Wyoming. *Environmental Geosciences, 13*(3), 181-199.

Gao, D., Wilson, T., Zhu, L., & Marfurt, K. J. (2011). 3D seismic curvature and flexure for unconventional fractured reservoir characterization at Teapot Dome (Wyoming) *SEG Technical Program Expanded Abstracts 2011* (pp. 1145-1149): Society of Exploration Geophysicists.

Giangiacomo, L., and A. Vivas. (2000). Course manual: prepared for
U. S. Department of Energy Naval Petroleum and Oil
Shale Reserves, Casper, Wyoming: Rocky Mountain

Region, Petroleum Technology Transfer Centre. 26
Groshong Jr, R. H. (2006). *3-D structural geology*: Springer.
Hardy, S., & Allmendinger, R. W. (2011). Trishear: A review of kinematics, mechanics, and applications.
King, G., & Brewer, J. (1983). Fault related folding near the Wind River thrust, Wyoming, USA. *Nature, 306*(5939), 147-150.
Kostenko, O. V., Naruk, S. J., Hack, W., Poupon, M., Meyer, H.-J., Mora-Glukstad, M., . . . Mordi, M. (2008). Structural evaluation of column-height controls at a toe-thrust discovery, deep-water Niger Delta. *AAPG bulletin, 92*(12), 1615-1638.
Kundacina, D. (2016). *Evaluation of strategies for fracture modelling: A case study at Teapot Dome, Wyoming.* University of Stavanger, Norway.
Lorenz, J. C., & Cooper, S. P. (2013). Natural fractures in folded sandstones of the Tensleep Formation, Wyoming.
McCutcheon, T. (2003). Time structure maps: 3D seismic data interpretation: Teapot Dome oil field. *Naval Petroleum Reserve*(3).
Okada, Y. (1985). Surface deformation due to shear and tensile faults in a half-space. *Bulletin of the seismological society of America, 75*(4), 1135-1154.
Okada, Y. (1992). Internal deformation due to shear and tensile faults in a half-space. *Bulletin of the seismological society of America, 82*(2), 1018-1040.
Olsen, D., Sarathi, P., Hendricks, M., Schulte, R., & Giangiacomo, L. (1993). *Case History of Steam Injection Operations at Naval Petroleum Reserve No. 3, Teapot Dome Field, Wyoming: A Shallow Heterogeneous Light-Oil Reservoir.* Paper presented at the SPE International Thermal Operations Symposium.
RMOTC. (2005a). Teapot Dome, Natrona County, Wyoming, NPR-3, well data set, CD-ROM. RMOTC (Rocky Mountain Oilfield Testing Centre).
RMOTC. (2005b). Teapot Dome, Natrona County, Wyoming, 2D and 3D seismic data data set, CD-ROM. RMOTC (Rocky Mountain Oilfield Testing Centre).
Schneider, S., Eichkitz, C. G., Schreilechner, M. G., & Davis, J. C. (2016). Interpretation of fractured zones using seismic attributes—Case study from Teapot Dome, Wyoming, USA. *Interpretation, 4*(2), T249-T260.
Schwartz, B. (2006). Fracture pattern characterization of the Tensleep Formation. *Teapot Dome, Wyoming: MS thesis, West Virginia University*.
Snyder, L., Dickinson, D., Brown, L., & Buhl, D. (1978). Detection of a weak maser emission pedestal associated with the SiO maser. *The Astrophysical Journal, 224*, 512-519.
Spieker, E. M. (1946). *Late Mesozoic and early Cenozoic history of central Utah* (2330-7102). Retrieved from
Thom, W. T. (1931). *The Significance of Geologic Conditions in Naval Petroleum Reserve N° 3, Wyoming, by WT Thom, Jr., and Edmund M. Spieker; with a Section on the Waters of the Salt Creek-Teapot Dome Uplift, by Herman Stabler*: US Government Printing Office.
Thomas, A. L. (1993). *Poly3D: A three-dimensional, polygonal element, displacement discontinuity boundary element computer program with applications to fractures, faults, and cavities in the Earth's crust.* Stanford University.
Wilson, T. H., Smith, V., & Brown, A. (2015). Developing a model discrete fracture network, drilling, and enhanced oil recovery strategy in an unconventional naturally fractured reservoir using integrated field, image log, and three-dimensional seismic data. *AAPG bulletin, 99*(4), 735-762.

Wilson, T. H., Smith, V., & Brown, A. L. (2013). PS Characterization of Tensleep Reservoir Fracture Systems Using Outcrop Analog, Fracture Image Logs and 3D Seismic.